

Three Decades of Tropospheric Ozone Lidar Development at Garmisch-Partenkirchen, Germany

Thomas Trickl, Helmuth Giehl, Frank Neidl, Matthias Perfahl and Hannes Vogelmann

Karlsruher Institut für Technologie, Institut für Meteorologien und Klimaforschung (IMK-IFU), Kreuzeckbahnstr. 19, D-82467 Garmisch-Partenkirchen, Germany

Correspondence to: Dr. Thomas Trickl, thomas@trickl.de, Thomas-Knorr-Str. 47, D-82467 Garmisch-Partenkirchen, Germany; Tel. +49-8821-50283

Abstract. Since 1988 two ozone lidar systems have been developed at IMK-IFU (Garmisch-Partenkirchen, Germany). A stationary system, operated at the institute, has yielded about 5000 vertical profiles of ozone from next to the ground to typically 3 km above the tropopause and has contributed data for a large number of scientific investigations. A mobile system was successfully operated in a number of field campaigns after its completion in 1996, before it was destroyed in major flooding in May 1999. Both systems combine a high data quality with high vertical resolution dynamically varied between 50 m in the lower troposphere and 250-500 m below the tropopause (stationary system). The stationary system has been gradually upgraded over the years. The noise level of the raw data has reached a level of about $\pm 1 \times 10^{-6}$ of the input range of the transient digitizers after minor smoothing. As a consequence, uncertainties of the ozone mixing ratios of 1.5 to 4 ppb have been achieved up to about 5 km. The performance in the upper troposphere, based on the wavelength pair 292 – 313-nm varies between 5 and 15 ppb, depending on the absorption of the 292-nm radiation by ozone and the solar background. In summer it is, therefore, planned to extend the measurement time from 41 s to a few minutes in order to improve the performance to a level that will allow us to trust automatic data evaluation. As a result of the time needed for manual refinement the number of measurements per year has been confined to less than 600. For longer time series automatic data acquisition has been used.

Key words: Tropospheric ozone, lidar, differential absorption, DIAL

1. Introduction

Lidar measurements of tropospheric ozone have resulted in important contributions to atmospheric research. Large variations of the concentrations on time scales of less than one hour may be observed, which have led insight into a number of tropospheric transport processes (see Table A1 for a large number of examples). In addition, measurements with ozone lidar systems have contributed to numerous air-quality studies (Table A2). Due to a considerable technical progress nowadays rather small changes of the volume mixing ratio of just a few parts per billion (ppb) can be resolved, which is necessary for distinguishing also the influence of minor contributions and for reliable trend studies.

Still, important tasks in tropospheric ozone research exist such as a clarification of the positive ozone trend observed until 2003 at high-lying observational sites in Europe (Scheel, 2003; Ordoñez et al., 2007) despite the pronounced reduction of ozone precursors over Europe (Jonson et al., 2006; Vautard et al., 2006), a detailed analysis of the rather complex contributions of different sources to long-range transport, or the influence of vertical mixing on free-tropospheric layers, in particular on stratospheric air intrusions (Trickl et al., 2014; 2015; 2016). Although vertical sounding, including lidar measurements of complementary quantities such as aerosols and water vapour (e.g., Trickl et al., 2014; 2015, 2020; Strawbridge et al., 2018; Fix et al., 2019), can yield key

1 information for the understanding of the role of the underlying atmospheric processes, for a long time there was
2 no significant growth in the number of tropospheric ozone lidar stations towards something like an international
3 network. By contrast, more and more ozone lidar systems have even been shut down. Opposite to this
4 development, recently a Tropospheric Ozone Lidar Network (TOLNet, [https://www-air.larc.nasa.gov/missions/
5 TOLNet/](https://www-air.larc.nasa.gov/missions/TOLNet/)) with seven lidar stations was established in North America (e.g., Newchurch et al, 2016; Wang et al.,
6 2017; Leblanc et al., 2018). It is important to note that even vertical profiles from the impressive MOZAIC
7 (Measurements of Ozone and Water Vapor by Airbus In-Service Aircraft) (Marenco et al., 1998) data base are
8 not able to resolve the fine-scale temporal variability of the vertical distribution of trace constituents because of
9 the rather confined time slots for the aircraft departures and arrivals at the individual airports. Satellite
10 measurements cannot yield the necessary information because of presently insufficient spatial resolution and
11 global coverage within a day.

12 With a few exceptions mostly ultraviolet (UV) differential-absorption lidar (DIAL) systems for tropospheric
13 applications have been proposed and developed since the 1975 (Papayannis et al., 1990; Table A3). Here, the
14 advantages of high Rayleigh backscattering and strong absorption cross sections are combined. In Europe, the
15 TESLAS (Tropospheric Environmental Studies by Laser Sounding) subproject of EUROTRAC (EUREKA
16 Project on Transport and Chemical Transformation of Environmentally Relevant Trace Constituents in the
17 Troposphere over Europe; EUROTRAC, 1997) has resulted in the co-ordinated development of several state-of-
18 the art ozone lidar systems (TESLAS, 1997). Lidar sounding of tropospheric ozone is a demanding technical task
19 (Weitkamp et al., 2000) because of the considerable dynamical range of the backscatter signal covering up to
20 about eight decades, the presence of aerosols and clouds, interfering trace gases such as SO₂ and NO₂, the solar
21 background (stratospheric ozone measurements are normally made during night-time), all necessitating an
22 elaborate optical and electronic design. The data evaluation is based on derivative formation that is particularly
23 sensitive to signal perturbations that set limitations to resolving the frequently rather small changes in free-
24 tropospheric ozone.

25 At IFU (Fraunhofer-Institut für Atmosphärische Umweltforschung; now: Karlsruher Institut für Technologie,
26 IMK-IFU), a differential-absorption lidar (DIAL) with a particularly wide operating range from next to the
27 ground to the upper troposphere was completed in 1990 in the framework of TESLAS and subsequently applied
28 for a full year (1991) within the TOR (Tropospheric Ozone Research) subproject of EUROTRAC (Carnuth et al.,
29 2002). The operating range of this system was extended to roughly 15 km by introducing three-wavelength
30 operation (Eisele and Trickl, 1997). Due to thoroughly upgrading of the data-acquisition system an uncertainty
31 level of 1.5 to 4 ppb has been achieved up to the mid-troposphere (slightly higher in the upper free troposphere,
32 depending on the ozone concentration and solar background).

33 In the mid-1990s a mobile ozone DIAL was additionally built in co-operation with OHB System (Bremen,
34 Germany; Brenner et al., 1997). This system, that was completed in spring 1996 and exhibited at the 1996
35 International Laser Radar Conference, could be operated in a vertical range between 0.2 and more than 4 km
36 with a similar accuracy as our stationary system at low altitudes and was used in a number of field campaigns
37 before it was destroyed by 2 m of water during major flooding in southern Bavaria in May 1999 when waiting
38 for the VOTALP "Munich field campaign" (VOTALP II, 2000).

39 In this paper we review the experience gained with these two lidar systems. The development of these two
40 systems has significantly contributed to the state of the art in this field. Meanwhile, even the dream of a
41 meaningful automatic data-evaluation looks feasible due to the technical progress made. Most approaches and
42 instruments used are the same in both lidar systems, which simplifies the description.

1 Most of the paper is devoted to the stationary DIAL. We describe only deviating design properties of the much
2 compacter mobile system such as the laser approach or the wavelength-separation technique chosen. This system
3 has been extensively used over three decades, but no full-size technical description has been given. We do not
4 want to give a full description of all the technical improvements made over the years. Just the decisive steps are
5 reported.

6 Most of the approaches of the ozone DIAL systems have been successfully transferred also to the other lidar
7 systems of IMK-IFU.

8 **2. General design considerations**

9 In both IFU DIAL systems fixed-frequency lasers and stimulated Raman shifting in H₂ and D₂ have been used
10 for generating suitable “on” and “off” wavelengths (see (de Schoulepnikov et al., 1997; Milton et al., 1998) for
11 general overviews). In this way just a single high-power laser source is needed. Both systems are three-
12 wavelength lidars with two “on” wavelengths and one “off” wavelength. This offers the opportunity of a wide-
13 range operation starting below 0.3 km above the ground, with stronger absorption and accuracy as well as good
14 vertical resolution for the shorter of the two “on” wavelengths and a range extension with lower vertical
15 resolution for the longer “on” wavelength. In addition, the comparison of ozone profiles obtained from two
16 separate wavelength pairs allows for internal quality control. In fact, as described in Sect. 6, for an optimum
17 alignment and sufficient backscatter signal the agreement between the different ozone profiles is almost perfect.
18 Apart from the wavelength separation methods the basic optical layout principles and detection electronics are
19 mostly the same. Both systems feature automatic data acquisition.

20 The stationary system (Fig. 1) is operated in two separate, rather large laboratories at IFU (47.477° N, 11.064° E,
21 740 m a.s.l.). This offers several advantages such as a simple optical layout, good alignment control due to long
22 beam paths, reduced thermal drifts because of no direct exposition of the laser system to outside air, or the long
23 distance between detection electronics and the interfering laser system. Two separate power systems are used for
24 laser and electronics. The laser PC is connected to the cleaner power system for the electronics and controls the
25 laser system via optical fibres. Remote control of the laser is achieved via RS232.

26 Due to the clean-air conditions prevailing at this rural site the wavelength choice is less critical. The ambient
27 concentrations of SO₂ and NO₂, species with absorption bands in the spectral range of ozone DIAL systems, at
28 are low which is known from the local long-term monitoring stations. Thus, the choice of the laser source was
29 determined by high power in order to achieve a short measurement time. Krypton fluoride lasers have been used
30 (Kempfer et al., 1994; Eisele and Trickl, 1997), since 1994 a model with a maximum available average power of
31 54 W at 248.5 nm (all wavelengths in this paper are given for vacuum).

32 The laser choice was different for the mobile system (Fig. 2). A frequency-quadrupled Nd:YAG laser with up to
33 4.2 W of average power at 266.1 nm served as the basic source of ultraviolet (UV) light. This approach was
34 preferred for several reasons: Due to the expected operation also in heavily polluted areas at least one
35 wavelength combination (266 nm – 299 nm) reduces the cross sensitivity with respect to SO₂ and NO₂ to about
36 0.01 ppb ozone per ppb of these species. Under such conditions, also the perspective of low interference by
37 aerosols is important, which is fulfilled for short “on” wavelengths (Völger et al., 1996; Eisele et al., 2005).
38 Thus, wavelength combinations involving 266 nm are favourable. Finally, due to the choice of a solid-state laser
39 source the dangerous gas handling in an excimer laser could be avoided, an issue for the mobile operation.

40 A clear design goal for the mobile system had been a vertical range significantly exceeding the boundary layer
41 by a few kilometres. This requirement had been seen as crucial for meaningful investigations during air-pollution

1 field campaigns. The mobile ozone DIAL was mounted inside an air-conditioned truck (Fig. 2) and was designed
2 for autonomous operation with an on-board power generator, batteries, automatic positioning (GPS) and a
3 detailed safety control management including rain and wind sensors, shutter control of the laser, and many
4 interlocks. Critical safety conditions immediately overrode any other action. The operator could be automatically
5 informed about incidents in his hotel during night-time via telephone. After rain, the system could be restarted
6 automatically, unless the laser was shut down (see Sect. 3.2).

7 The detection system of this DIAL was much simpler, with a less demanding optical set-up (single telescope for
8 both near- and far-field detection, simple filter polychromator) and with less electronic components due to a
9 sequential emission of two of the three operating wavelengths. All this resulted in a considerable reduction of
10 costs, at that time an attractive perspective also in view of the goal of our industrial partner of an affordable
11 commercial system.

12 Overall specifications of the two systems are listed in Tables 1 and 2. All optical components and dielectric
13 coatings have been provided by Laseroptik G.m.b.H. (Garbsen, Germany) unless otherwise specified.

14 3. Transmitter Design

15 3.1. Stationary Lidar

16 The transmitter of the system (Fig. 1, Table 1) is based on a KrF excimer laser (Lambda Physik, LPX 250,
17 maximum repetition rate 100 Hz) consisting of a tunable narrowband oscillator and a three-pass power amplifier.
18 CaF₂ is used for transmitted optics. CaF₂ is not birefringent and, thus, polarization effects (Kempfer et al., 1994)
19 and ageing are avoided. The energy was considerably enhanced by anti-reflection (AR) coating the outer side
20 windows of the amplifier gas cell and the beam splitter in front of the energy monitor. A pulse energy of up to
21 540 mJ was measured several metres away from the laser where divergent components also emerging from the
22 amplifier can be separated and blocked by an aperture. For the lidar measurements the laser energy is usually set
23 to 400 mJ. The unstable cavity of the amplifier yields a highly collimated rectangular beam with a divergence of
24 0.2 mrad. The wavelength was set for maximum output and the prism-grating combination never touched again.
25 In 2010 measurements with a HighFinesse WS6 ($\Delta\lambda = 0.6$ pm) wavelength meter carried out over several days
26 yielded $248.5078 \text{ nm} \pm 0.0060 \text{ nm}$, in agreement with the results of Kempfer et al. (1994). The spectral
27 bandwidth is specified as 0.2 cm^{-1} (6 GHz). Locking the amplifier to the oscillator can be nicely verified by an
28 enhancement of the pulse energy by up to 70 mJ under our standard operating conditions.

29 The output of the KrF laser is split by a 50-% beam splitter and focused into two Raman cells with $f = 1.0$ -m
30 AR-coated plano-convex CaF₂ lenses. One cell is filled with hydrogen and the other one with deuterium, and the
31 same pulse energy per cell as previously used for a single cell (Kempfer et al., 1994) is ensured (almost 0.2 J). A
32 total of six Stokes components are generated in hydrogen, just 277.124 nm (S1) and 313.188 nm (S2) are taken
33 (Table 1). For deuterium the second Stokes (S2) component (291.838 nm) is used. The outer surfaces of the CaF₂
34 windows of the Raman cells are AR coated. The inner ones are not coated because of the possibility of ageing in
35 the presence of photolysed hydrogen. The pump radiation leaving the evacuated Raman cells is of the order of
36 160 mJ. The output of the Raman cells is combined with a pair of dichroic beam combiners and collimated with
37 an $f = 5$ -m, 150-mm-diameter concave spherical mirror. The beam combiners reflect 99 % of the 292-nm
38 radiation at 45° and transmit 88 to 90 % of all the other relevant spectral components. Overlap and pointing of
39 the 292-nm beam are optimized by placing a wire cross in front of the D₂ cell or behind the second beam
40 combiner, by watching the images of the cross in front of mirror M4.

1 The Raman conversion efficiency obtained with the LPX 250 laser system is lower than that previously
2 published (Kempfer et al., 1994). We ascribe this to the smoother energy distribution in the beam profile of the
3 new laser. As an example, Fig. 3 shows the conversion efficiencies obtained for hydrogen for a laser pulse
4 energy of almost 200 mJ per Raman cell, attenuated by the optics, in particular by the single-side AR coated cell
5 entrance windows). The sum of all conversion efficiencies is less than 1.0 starting at low pressures already. This
6 loss of overall energy is tentatively ascribed to optical breakdown. Above 3 bar the loss starts to level off. The
7 non-negligible fourth Stokes emission (Kempfer et al., 1994) was not determined. The maximum second-Stokes
8 conversion efficiency for deuterium is approximately 17 % (at 11 bar). The operating pressures have been
9 chosen around 3.3 bar and 11 bar for H₂ and D₂, respectively.

10 The conversion efficiency was determined for a laser repetition rate of 10 Hz in order to avoid damage to the
11 power meter used. During the lidar measurements it turned out that the second-Stokes output may increase when
12 selecting a repetition rate of 100 Hz, sometimes even leading to range signal overflow in the transient digitizer.
13 This effect was unexpected and must be taken into account when setting the detector supply voltages. We did not
14 analyse this behaviour in detail.

15 Linear polarization is important for single-line output of the Raman shifters (Kempfer et al., 1994). We placed a
16 Glan prism and a Fresnel rhomb (both from Halle) in the beam between oscillator and amplifier. All mirrors and
17 beam splitters of the transmitter section were manufactured with minimum polarization sensitivity. The Fresnel
18 rhomb is rotated for optimum backscatter signal (Fig. 4). The strong modulation of the lidar signal in Fig. 4 is
19 mainly caused by the holographic gratings used in the receivers (Sect. 3).

20 Due to the high average power of the laser system the time for a single ozone measurement, carried out with a
21 repetition rate of 99 Hz, is as short as 41 s.

22 **3.2 Mobile Lidar**

23 The pump laser of the mobile DIAL was a frequency-quadrupled Nd:YAG laser with 30 Hz repetition rate and
24 pulse energies of up to 140 mJ at 266 nm (Continuum, Powerlite 9030). The laser was selected because of a
25 remote control option. The manufacturer had promised external control of warm up and rotation of the frequency
26 doubling and quadrupling crystals. The 1064-nm and 266-nm powers were measured by two Moletron power
27 meters for a PC-based power optimization. However, the computer control never worked properly: Automatic
28 warm up of the laser was never achieved. The reason was a conflict with “keep-alive” pulses that had to be sent
29 by the external control.

30 The quadrupling was achieved by using BBO (beta barium borate). This approach yielded high conversion
31 efficiency and moderate thermal loading. However, after more than one year of infrequent operation of the lidar
32 the surface of the crystal started to degenerate. This turbid layer did not strongly reduce the UV emission and
33 polishing was, therefore, postponed.

34 At maximum pump energy (1.6 J at 1064 nm) ring-the 266-nm radiation exhibited a ring-shaped mode, at a
35 pulse-energy level of 140 mJ. We reduced the pulse energy to 1.1 J. Still, 120 mJ could be produced, now with a
36 filled beam profile. However, a hot spot formed that focussed in the Raman-shifting compartment and we
37 reduced the UV output to about 70 mJ for safety reasons. This hot-spot problem was solved by the manufacturer
38 in a later (“Precision”) version of the laser.

39 A ceramics shutter was added to the exit holes of the Powerlite laser that was controlled by both the safety
40 system and the lidar PC. Closing the shutter was preferred to switching off the laser oscillator in order to
41 maintain stable thermal conditions in the laser during an interruption.

1 A side view of the lidar including the entire transmitter is given in Fig. 2, the lower level of the frame in Fig. 5.
2 Figure 5 shows the Raman shifting compartment that also contained a 6:1 beam expander used for reducing the
3 beam divergence. Rotating beam splitters were used for directing the laser pulses into the H₂ and D₂ cells. These
4 beam splitters were based on a circular quartz plates differently coated on the two halves of the surface, high
5 reflecting for the lidar wavelengths on one half and high transmitting on the other one. The rotation was
6 synchronized to the laser pulses. The control unit issued pulses for identifying the Raman cell actually passed for
7 the data-acquisition system. Two precision motors with measured out-of-axis rotation of just about $\pm 2 \mu\text{rad}$ and
8 $\pm 40 \mu\text{rad}$, respectively, were chosen (KaVo, model EWL 4025; with custom-made electronic control).
9 Due to a high thermal sensitivity the emission wavelengths of Nd:YAG lasers may vary considerably from
10 model to model. We derive a guess of the unknown pump wavelength of our Powerlite laser model from (Trickl
11 et al., 1989; 2007) and wavelength measurements for three other injection-seeded Nd:YAG lasers in our
12 laboratory. The average pump wavelength of $266.120 \text{ nm} \pm 0.011 \text{ nm}$. This yields first-Stokes-shifted
13 wavelengths of 289.103 nm (in D₂) and 299.209 nm (in H₂).
14 We reached maximum first-Stokes (S1) conversion efficiencies of almost 50 % both in hydrogen and deuterium
15 at pressures of as low as 0.9 bar and 1.6 bar, respectively. This is remarkable in two respects: the theoretical
16 Raman conversion efficiency reaches 50 % at higher pressures and the Raman gain of deuterium is substantially
17 smaller than that of hydrogen (de Schoulepnikov et al., 1997). A total of five Stokes orders and one anti-Stokes
18 order were visually observed for hydrogen, less orders in deuterium. There was some contribution of the second
19 Stokes order (particularly low at 1 bar due to gain competition with S1), but those for the higher orders were
20 below the 1 mW detection threshold of the power meter used. Starting at pressures below the threshold for
21 Raman conversion absorption was realized and, in H₂, the conversion efficiency rapidly dropped to zero above
22 about 1 bar. The same effect was observed also in pure helium and argon. Thus, we ascribe these observations to
23 laser-induced breakdown. The role of the hot spot in igniting this breakdown could not be examined. Quite
24 obviously, the Stokes emission was emitted prior to the breakdown maximum (see also Trickl, 2010). In any
25 case, the high conversion efficiency achieved was more than enough for the lidar operation.
26 Motivated by the hot-spot problem the focussing lens was replaced by a pair of crossed $f = 1.0 \text{ m}$ cylindrical
27 lenses during the final phase of operation of this lidar system. As suggested in by Perrone and Piccinno (1997)
28 this may result in a softer focus, a larger focal volume and higher Raman conversion. The maximum possible
29 distance between the two lenses was about 12 cm and was chosen for the lidar operation. In Fig. 6 the conversion
30 efficiencies as a function of cell pressure for this distance and also for the minimum possible distance of about 5
31 cm is given. A clear change in behaviour was seen. The transmitted pump energy no longer dropped to zero
32 above 1 bar. As one would expect the depletion for pressures up to 2 bar is smaller for the larger distance
33 between the two lenses. Quite interestingly, the pump depletion in D₂ was much less pronounced than that in H₂.
34 Despite these obvious improvements, the maximum conversion efficiency just rose for H₂ (to 61 %, comparable
35 to the results by de Schoulepnikoff et al., 1997).
36 The rectangular beam-steering mirror was mounted on two mutually orthogonal rotation stages (OWIS). The
37 beam pointing angle was set on the lidar PC.

38 4. Receiver Design

39 4.1 Design Principles

40 The optical layout of the IFU lidar systems built or modernized since 1990 is based on several design principles:

- 1 (1) The use of Newtonian telescopes for a less critical alignment than in the case of a Cassegrain telescope and
2 for an easier discrimination of the near-field signal.
- 3 (2) Separate detection in near-field and far-field channels in order to reduce the giant dynamical range of the
4 backscatter signal covering roughly eight-decades.
- 5 (3) No optical elements or detectors are placed close to the focal points in order to avoid a modulation of the
6 backscatter signal by the near-field scan of the focal point across inhomogeneously transmitting or detecting
7 surfaces. A severe example for a photomultiplier tube (PMT) is given by Simeonov et al. (1999). In
8 particular, this principle also strongly prohibits the use of optical fibres because of their unknown input
9 surface quality (apart from the coupling losses).
- 10 (4) Particularly inhomogeneous surfaces must be placed in or very close to image planes (exit pupils) where the
11 image spots and the light bundle as a whole stay stable in space. As a result even very long beam paths do
12 not matter as long as no aperture is hit due to an excessive pointing drift of the laser beam. In this way a
13 stable performance is achieved over long periods of time. Also the diameter of the light bundle reaches its
14 minimum in the exit pupil, and it is important to place components with limited diameter in (or very close
15 to) this plane, such as detectors, optical filters, gratings or beam splitters.
- 16 (5) All lenses with focal lengths below 0.2 m must be anti-reflection coated in order to avoid angle-dependent
17 transmittances. Anti-reflection coating was applied to all lenses in IFU lidar systems after 1995 also to
18 avoid transmission losses.

19 In most of our lidar systems we have chosen a modular design composed of a series of relay-imaging pairs of
20 equal lenses (distance $2f$) with beam splitters or filters close to the centre between the lenses (Vogelmann and
21 Trickl, 2008; Giehl and Trickl, 2010; Klanner et al., 2020). This approach is also implemented in the receiver of
22 the stationary ozone DIAL, however with a holographic grating instead of optical filters. However, in the mobile
23 system a convergent beam path was chosen behind the ocular of the telescope in order to save space.

24 **4.2 Telescopes**

25 *Stationary system*

26 The large dynamical range of the backscattered light of about eight decades is reduced by using two separate
27 Newtonian telescopes (Kempfer et al., 1994) as shown in Fig. 1 (manufacturers: Vehrenberg (entire small
28 telescope) and Lichtenknecker (mirrors only). The primary mirrors have diameters of 0.13 m and 0.5 m, and
29 focal lengths of 0.72 m and 2.0 m, respectively. The axes of the two telescopes are in plane with the outgoing
30 laser beam and located about 0.2 m and 1.8 m from that of the beam, respectively.

31 The solar background was reduced by both black surfaces and a black circular baffle around the input path of the
32 backscattered radiation. This turned out to be insufficient after introducing new detectors in 2012 that are more
33 susceptible to the background (Sect. 4.4).

34 The approximate vertical range is 0.2 to 2.5 km above the ground for the small near-field telescope and 1.5 to 3-
35 5 km above the tropopause for the large far-field telescope with a dynamically adjusted vertical resolution of 50
36 to 300-500 m. Both telescopes are combined with 1.1-m grating spectrographs. This led to a much better
37 daylight rejection in comparison with Kempfer et al. (1994).

38 The alignment of the small telescope is very difficult, given the very long beam paths through the polychromator
39 (Sect. 3.3). It was highly difficult to avoid nonlinearities of the results on the first few hundred metres. The
40 signal had to be attenuated by a factor of ten. The solution was found a few years ago. During the routine four-
41 quadrant (“telecover”) testing (Freudenthaler et al., 2008), introduced for quality assurance within EARLINET

1 (European Aerosol Research Lidar Network; e.g., Amodeo et al., 2010; <http://www.earlinet.org/>), it turned out
2 that almost the entire near-field return passed through the quadrant on the side of the outgoing laser beam
3 (named “north” sector). This explains the observed sensitivity to misalignment.

4 The north sector of the telescope was subsequently covered by a triangular piece of cardboard. After this, the
5 alignment sensitivity of the near-field receiver (including the spectrograph, see below) disappeared, a stable
6 linear performance was obtained and the signal was attenuated to an acceptable level due to the missing “north”
7 quadrant. Another important consequence was that no additional attenuators had to be used after this
8 change. Most importantly, after the design change a very reliable diurnal variation of ozone could be retrieved in
9 the boundary layer with a morning minimum and an afternoon maximum.

10 The alignment of the far-field receiver has remained stable during the past 24 years. The only parameters
11 routinely optimized have been the laser-beam pointing and the overlap of the two partial laser beams from the
12 two Raman shifters. Slight deviations in the overall beam pointing do (inside the slits in the focal planes) not
13 matter (despite the long distances in the receivers) due to the imaging principles applied: The final and the
14 intermediate images of the primary mirrors are not shifted.

15 *Mobile System*

16 A single Newtonian telescope with an $f = 1.56$ m, 317.5-mm-diameter principal mirror (Intercon Spacetec) was
17 used. The distance between the laser and the telescope axes was 0.5 m. The exit of the telescope towards the
18 detection polychromator was (horizontally) perpendicular to these two axes.

19 **4.3 Wavelength Separation**

20 *Stationary System*

21 After 1994, the wavelength separation for the stationary system was achieved with two identically built 1.1-m
22 grating spectrographs, one per telescope (Figs. 1 and 7). A grating spectrograph has the advantage of the
23 transverse near-field-far-field beam walk and the spectral separation taking place in separate, mutually
24 orthogonal planes. As explained in more detail by Kempfer et al. (1994), a near-Wadsworth configuration was
25 chosen in order to reduce the astigmatism to an acceptable level. The Wadsworth angle for a given wavelength is
26 defined by an exit of the first diffraction order along the grating normal. As shown by ray tracing the spectral
27 resolution is also close to optimum for this approach and was expected to be 0.2 nm. The design described by
28 Kempfer et al. (1994) was extended by placing $f = 80$ mm lenses in front of the detectors for imaging the
29 primary mirrors of the telescopes on to the photocathode of the PMT. The spherical grating (Carl Zeiss, $r = 1995$
30 mm) was also placed in an image plane of the primary mirror to minimize the diameter of the radiation bundle.
31 Detailed numbers are given by Eisele (1997).

32 The true spectral resolution was determined with a mercury lamp to be about 0.35 nm, achieved with low-
33 intensity emission lines not exhibiting line broadening due to absorption in the lamp prior to emission. Due to
34 the defocusing caused by the beam walk the effective spectral range for the components of the integrated lidar
35 return is 1.0 nm (full width at half maximum, f.w.h.m.), but with sharp edges. The grating efficiency was
36 specified as 70 % by the manufacturer (Carl Zeiss, Oberkochen) in auto-collimation, which may be different for
37 the Wadsworth configuration.

38 An aperture with four adjustable blades (custom-made by OWIS) was placed at the entrance of each
39 spectrograph in the focal plane of the primary mirror for reducing the level background light. In the large

1 receiver the vertical blades were adjusted to block the near-field return and to transmit the return from all longer
2 distances. These vertical blades were never touched again and laser beam steering mirror always set for a peak
3 signal at 8.0 μ s. The horizontal blades are set for a slit width of 2-3 mm, after alignment with a narrow slit. The
4 minimum slit width possible for the S1 radiation is 0.7 mm (0.35 mrad), more being needed for the S2
5 components. The consequence of the small spot size is a low susceptibility to typically observed laser pointing
6 drifts, and the 277-nm return always yields correct ozone values.

7 Further adjustable slits (widely open) were placed in the secondary focal planes in front of the PMTs. However,
8 this was just for occasionally controlling the alignment since no cross talk between the different wavelength
9 channels was observed. As mentioned no alignment drifts were found.

10 As already mentioned in Sect. 3.1 the lidar signal varies with the polarization angle of the laser (Fig. 4). An
11 approximate 5:1 sinusoidal modulation is seen. The polarization angle was set for optimum signal.

12 *Mobile System*

13 The polychromator design for the mobile system system is quite different and is based on dielectric mirrors,
14 beam splitters, an edge filter and adjustable-slit apertures (Fig. 8). The 289 nm and 289 nm returns were
15 separated by temporal discrimination, triggered by the rotating beam splitters described in Sect. 3.2. The data
16 were stored in different areas of the transient digitizers. The separation of the larger gap between 266 nm and the
17 two longer wavelengths could be conveniently achieved by pairs of dielectric beam splitters (BS3), each of them
18 transmitting just 3 % of the longer wavelengths and fully reflecting the 266 nm component at an incidence angle
19 of 45°. In this way, two 266-nm channels were available for both the near- and the far-field sections of the
20 polychromator. As seen in Fig. 8, the entire arrangement is highly symmetrical and almost identical for the near-
21 and far-field parts. A 1:100 beam splitter and an O.D. 1.0 neutral density filter (Andover) were used to separate
22 and to attenuate the near-field return. In the far-field section the signal was first adjusted to match perfectly the
23 near-field signal for low PMT gain. After this procedure, OWIS adjustable-blade apertures (see above), placed in
24 the focal planes in front of the PMTs, were used to cut off the strong near-field return that was shifted
25 horizontally (due to the perpendicular geometry of the outgoing laser beam, the telescope axis and the telescope
26 output axis). Finally, the PMT gain was increased to maximize the far-field signal. This approach is a rather
27 simple alternative to the use of two telescopes as done in our stationary system and is also applied in our water-
28 vapour DIAL (Vogelmann and Trickl, 2008). However, it requires very constant pointing of the outgoing laser
29 beam in order to avoid changes in signal level. This was not perfectly the case for the laser used here, but could
30 be verified for the more recent (“Precision”) version of the Powerlite laser of the H₂O DIAL.

31 An OWIS adjustable-slit aperture was also placed in the focal plane of the telescope (top of Fig. 8) for the
32 reduction of the solar background. To account for the changing position of the “focus” as a function of the
33 changing position of the outgoing laser pulse the orientation of the slit was horizontally tilted (i.e., perpendicular
34 to the orientation in the stationary system, due to the 90° rotation of the telescope exit). The vertical blades of the
35 aperture could be closed to 1.7 mm (corresponding to an acceptance angle of 1 mrad) without a loss of signal,
36 but were set slightly wider during normal operation.

37 Each of the four detection channels principally look the same, apart from the different surfaces of the
38 components (HR1 (high reflector for 266 nm) and BS3). As mentioned the set-up deviates from the conventional
39 modular set-up with relay-imaging lenses. The $f_1 = 100$ mm ocular (L1) does not collimate the lidar return, it
40 directly refocusses the radiation to an intermediate focal point. In this way, the overall distance to the detectors
41 could be shortened. Just one additional lens (L2, $f_2 = 50$ mm) was used for exactly imaging the principal mirror

1 of the telescope onto the photocathodes of the PMTs. Most optical components were placed in the vicinity of the
2 intermediate images of the the primary mirror (green dots in Fig. 8).

3 One deficiency that was never overcome before the destruction of the system was that just a single PMT was for
4 both “on” and “off” channels in the far-field section. Since the “on” signal peak is already rather small at the
5 beginning of the far-field signal, the “off” component should be attenuated, e.g., by rotating quartz plates with
6 two differently coated halves similar to those next to the Raman shifter should be used. This would allow the
7 “off” signal to be reduced to about the same level as the “on” signal, and a higher PMT gain could be used.

8 **4.4 Detectors**

9 The detectors are key components of our lidar development, which calls for an explicit description. After the
10 experience in early years (Kempfer et al., 1994) we used until April 1996 exclusively the fourteen-stage EMI
11 9893B photomultiplier tubes (PMTs). For linear performance the 9893B detectors were operated with maximum
12 analogue signal levels below 10 mV (50-Ω termination). This means that the very high gain of this fourteen-
13 dynode PMT (up to eight decades) is completely unnecessary. The big plus was range gating (Kempfer et al.,
14 1994) lifting the far-field signal level to values mostly well above the electronic imperfections of the signal
15 processing system. The range-gating circuit was further improved for repetition rates of more than 20 Hz.

16 However, after very positive testing in 1995, we introduced Hamamatsu H5783P-06 PMT modules to both
17 DIAL systems in spring 1996 (Brenner et al., 1997; Eisele and Trickl, 1997). The miniature PMT features a
18 built-in Cockroft-Walton power supply, an 8-mm-diameter photocathode and six mesh dynodes, leading to a
19 maximum current gain of 3×10^5 . This gain is sufficient for obtaining a very big lidar signal. This module is
20 extremely linear over at least five decades for analogue signals up to at least 100 mV (50 Ω termination) in the
21 operating voltage range around the most recommended 800 V. Fluorescence-free Corion SB-300-F short-pass
22 filters were placed on the PMTs and efficiently removed radiation for wavelengths beyond 320 nm.

23 The small size of the modules allowed us to achieve a very compact design of the polychromators of the two
24 lidar systems. In particular, side-by-side operation of all three PMTs in the spectrographs of the stationary DIAL
25 became possible. These modules were used in our stationary system for more than fifteen years without
26 discernible signs of ageing.

27 Finally, driven by the hope for further improvement, we replaced in 2012 the Hamamatsu H5783P-06 modules
28 by an actively stabilized version optimized for us in 1999 for our three-wavelength aerosol lidar (Kreipl, 2006)
29 by Romanski Sensors (RSV). This device had to be based on the follow-up PMT version Hamamatsu R7400U-
30 03, because the 5600 series was longer available. The socket was further modified to deliver optimized single-
31 photon spikes without the ringing of the original PMTs (Figs. 9a and 9b). The power connection cable is
32 shielded, but the shield is grounded just on one side.

33 Similar to the Hamamatsu module the RSV socket generates a clean reference voltage (5 V). This voltage is
34 produced from the 15 V supply voltage. The 5-V reference, corresponding to a PMT voltage of 1000 V, is then
35 returned to the power supply where it is divided to the adjustable final control voltage level (0 to 5 V) that is sent
36 back to the detector (Fig. 3.12 of Kreipl (2006)). This loop was necessary to clean the lidar signals to a level
37 below 10^{-5} of the peak signal. Sending in just an external control voltage had resulted in an unacceptable baseline
38 crossing of about 10^{-4} of the peak lidar signal.

39 The diameter of these detector modules, 50 mm, was too large for operating the PMTs for 277 nm and 292 nm
40 side by side in the spectrograph of the stationary system. In order to make this possible RSV delivered four of
41 the modules with the small PMT tubes mounted off axis.

1 Testing of the PMTs in our three-wavelength aerosol lidar had shown that above peak signals of 40 mV signal-
2 induced nonlinearities become observable that are attributed to photocathode overload (Fig. 3.10 of Kreipl
3 (2006); English version: <http://www.trickl.de/PMT.PDF>). However, this result was obtained for a PMT supply
4 voltage of the order of just 450 V, and, therefore, corresponded to an excessive photon flux (see Fig. 10 for a
5 gain curve). For voltages around 800 V (maximum: 1000 V), as recommended for photon counting, the incident
6 radiation levels for creating the same signal are roughly 100 times lower. As a consequence, much higher signal
7 levels can be afforded and, in recent years, we have routinely set the peak signals in the far-field receiver to 70
8 mV, this being a rather conservative choice. This setting was motivated by decision to stay within the 100 mV
9 input range of the transient digitizer (Sect. 4.5).

10 We ascribe this unprecedented performance due to the mesh layers of the dynode stages that likely to act as
11 electrostatic kinetic energy filters for the electrons. A pulse-height spectrum of one of the PMTs for the
12 recommended operating voltage of 800 V is shown in Fig. 11. This spectrum was derived from a time scan with
13 a 1-GHz digital oscilloscope (Tektronix, DPO 7104). No rise in photon counts towards 0 V pulse height is seen
14 that would indicate signal-induced cathode emission, this result being limited by the chosen trigger level of the
15 scope of -1.5 mV. It is important to mention that the pulse-height distribution does not end at -23 mV. As can
16 be concluded from Figs. 9a and b much higher pulses exist that can reach almost -200 mV. For one-hour
17 measurements with our Raman lidar (Klanner et al., 2020) we did not observe dark counts in 7.5-m bins for
18 discriminator thresholds of 4 mV and PMT supply voltages beyond 900 V.

19 In the far-field receiver we found that a high number of photons is more important than a high peak analogue
20 voltage because the photon noise dominates the signal at large distances. Thus, we no longer attenuate the
21 signals and irradiate the photocathode with all the light emerging from the spectrograph. For compensation we
22 reduce the PMT voltage to about 700 V. Now, the 70 mV signal level corresponds to about 2.5 times more
23 photons per time interval than before. This change has resulted in considerable lowering of the ozone noise for
24 the 292 – 313-nm wavelength combination in recent years. Photon counting at 700 V and the resulting much
25 lower single-photon amplitudes has not been tested so far (Sect. 4).

26 A really bad surprise was that the 7400 PMT is more than one order of magnitude more susceptible to daylight
27 than the old modules. The H5783P-06 modules had stayed linear up to about 12 mV of constant-background
28 analogue signal. Now, the constant signal background must be kept below 1 mV. This task has been demanding
29 at 313 nm during the brightest part of the day, aggravated by the degraded surface of the primary mirror and in
30 the presence of clouds. In spring and summer even signal undershoot to below the signal base line has been
31 observed during the hours around noon. We added a 5.7-nm (f.w.h.m.) filter from Laseroptik was used for
32 additional background blocking. Still, mathematical corrections had to be made, which were particularly
33 important for optimum aerosol retrievals. A filter with a 0.5-nm flat top and very steep edges is needed.
34 Additional solutions could be an additional light baffle above the telescope and replacing the aged primary
35 mirror of the telescope.

36 4.5 Transient Digitizers

37 For the digitization of the analogue signal a 12-bit transient digitizer was found to be sufficient for avoiding the
38 influence of single-bit steps since the shot-to-shot noise is larger than a least significant bit (LSB). This has
39 anticipated by numerical simulations with artificial noise before the 1994-1995 upgrading of the stationary
40 system that demonstrated the absence of steps for a noise amplitude of 4 LSBs. A saw tooth generator built for

1 randomizing the single-bit steps turned out to be unnecessary. By contrast, Langford (1995) reported a
2 significant improvement in his system achieved by modulating the signal.
3 In the upgraded stationary system, the a 12-bit, 20 Hz system from DSP Technology was used until 2003. Since
4 the mobile system was built one year later the first 12-bit, low-noise 20 Hz transient digitizers systems from
5 Licel became available and was used. The performance was excellent with lower noise than in the DSP system.
6 In 2013, the Licel transient digitizers were upgraded on our request by introducing custom-made ground-free
7 input amplifiers. This latest version has led to an unprecedented performance with a relative noise level of about
8 $\pm 1 \times 10^{-6}$ of the full 100 mV voltage range after minor smoothing (Sect. 7.1), yielding also highly sensitive
9 aerosol measurements at 313 nm despite the short wavelength. This unprecedented performance has made
10 possible to operate the system without photon counting with very little loss of quality.
11 Though being much noisier, the DSP Technology system was more linear than that of Licel as resolved down to
12 a level of 2×10^{-5} of the full scale (Kreipl, 2006; Fig. 3.10: <http://www.trickl.de/PMT.PDF>). When firing the laser
13 of our mobile aerosol lidar near-horizontally on to a rock at a distance of 9 km, where the peak equalled the
14 signal maximum, the return from beyond the rock instantaneously and exactly returned to zero. By contrast, the
15 Licel system yields small undershoot for distances beyond remote clouds, larger for larger signal areas. Of
16 course, the performance is perfect in the absence of clouds that generate very pronounced spikes. The
17 performance of the most recent version of the Licel system is discussed further in Sect. 7.1.

18 **4.6 Pre-amplifiers**

19 In order to lift the PMT output, typically around 10 mV for the old PMTs and 70 mV for those from Hamamatsu
20 (into 50 Ω), to the coarsest range of the transient digitizers adjustable-gain pre-amplifiers were used until 2011
21 (Analog Modules, model 351, bandwidth 4 MHz, gain adjustable between 1 and 10). In two of the far-field
22 channels (“on” wavelengths”) these pre-amplifiers produced some very small small ringing. Between 1997 and
23 2003 these problems were overcome by using photon-counting data. For many years of exclusively using
24 analogue data the ringing had to be removed by mathematical corrections. The ringing and the additional noise
25 finally completely disappeared after disconnecting the zero voltage. After introducing the latest (ground-free)
26 version of the Licel input stage the preamplifiers were removed.

27 **4.7 Photon counting**

28 In the stationary ozone DIAL single-photon counting was applied between spring 1997 and 2003 with a FDC700
29 1-GHz photon-counting system from Optec. The signals were fully linear starting in the middle troposphere, but
30 produced extra counts at lower altitudes, presumably due to pile-up effects of the PMT ringing (Fig. 9a). The
31 signal for photon-counting was separated from the analogue output by an impedance-matched junction
32 containing an adjustable discriminator custom made by RSV. In the first version the discriminator level could
33 not be reduced to below 11 mV. This level had to be chosen to ensure linear performance and maximum signal
34 (Fig. 11). The unit was upgraded several year ago for picosecond time resolution and discriminator levels down
35 to 2 mV.

36 The new PMT units delivered by RSV are free of the ringing of the original Hamamatsu tubes (Sect. 4.4) and
37 feature pulse widths of about 1.5 ns (Fig. 10). In order to benefit from this considerable time resolution we
38 recently purchased MCS6 and MCS6A five-channel high-speed photon counting systems from Fast Comtec for
39 several of our lidar systems. The signals are scanned for selectable pulse edges at intervals of 100 ps which
40 means a maximum count rate of about 5 GHz for equidistant picosecond pulses. For both reasons a highly linear

1 photon-counting performance was achieved that is presented in detail in the parallel publication on our Raman
2 lidar for water vapour and temperature (Klanner et al., 2020).
3 The simultaneous analogue and photon-counting measurements from a single PMT lead to a deterioration of the
4 analogue signal with an artificial perturbation of the signal of the order of 10^{-4} of the peak voltage. This could be
5 reduced by one order of magnitude by adding an optocoupler to the trigger input of the counting system.
6 However, the shape of the perturbation was somewhat complex and, thus, difficult to correct mathematically. In
7 addition, we do not have experience with photon counting at the currently preferred PMT voltages around 700 V
8 or less (see above). At this time the simultaneous application of photon counting is postponed until a better
9 solution becomes available.

10 **4.8 System Control**

11 All connections between electronic components of the two DIAL systems are ground-free. The trigger pulse is
12 derived from a photodiode and subsequently distributed into numerous output channels via optocouplers
13 (Ingenieurbüro W. Funk). The supply voltages for the PMTS, preamplifiers and discriminators (Ingenieurbüro
14 W. Funk) are generated implying high-quality DC-DC converters (TRACO POWER, models TYL 05-05S30
15 and TYL 05-15W05). They are transferred to the different devices in shielded cables. The shields of the cable
16 leading to the PMTs are open on the side of the detectors. The supply voltage can be set by the lidar PC via an
17 I²C bus, but this option has never been used in the stationary system because of the rather stable clean-air
18 conditions at Garmisch-Partenkirchen. Also the opening and closing of flap in the roof was initiated via I²C bus.
19 Electromagnetic interference from outside (e.g., the laser) has been kept at a negligible level by using doubly
20 shielded signal cables (Suhner, G03332; the outer shield is left open on one side) and ground-free circuits. The
21 trigger pulses were obtained from photodiodes and then distributed via optocouplers.
22 The firing of the XeCl laser was initiated via RS232 remote control of the computer of the excimer laser. The
23 power for the high-voltage circuits of the laser is supplied by a separate source. The laser PC was connected to
24 to the clean power in the lidar laboratory. The laser itself is controlled by its computer via optical fibres. Finally,
25 both cables connecting the lidar laboratory and the laser PC are shielded which successfully removed any
26 interference from the high-voltage pulses (Eisele and Trickl, 1997).

27 **4.9 Automatic Operation**

28 Both DIAL systems have been extensively operated under automatic control by the lidar PC. In the mobile
29 system an external start and warm-up of the laser was not possible due to issues in the programs delivered by
30 Continuum. The laser output was continuously controlled: The measurements were interrupted if the 1064-nm
31 and 266-nm power levels were below maximum.

32 Among the various error conditions the most important ones are rain or high wind speed. This results in
33 immediate closing the flap in the roof. As to the KrF laser the high-voltage is shut down, and as to the Nd:YAG
34 laser the output shutter is closed the laser continuing to fire in order to maintain thermal equilibrium of the
35 frequency doubling crystals.

36 Time series under automatic control have been extended for the stationary system to up to four days. In this was,
37 numerous atmospheric transport studies could be made, the first four-day series leading to the first detection of
38 North American ozone over Europe (Eisele et al., 1999; Trickl et al., 2003).

39 **5. Data Processing**

1 The number density of ozone, n_{O_3} , is obtained by computing the DIAL equation

$$2 \quad n_{O_3}(r) = -\frac{1}{2\Delta\sigma} \frac{d}{dr} \ln \frac{P(\lambda_1, r)}{P(\lambda_2, r)} + \frac{1}{2\Delta\sigma} \frac{d}{dr} \ln \frac{\beta(\lambda_1, r)}{\beta(\lambda_2, r)} - \frac{1}{\Delta\sigma} (\alpha_r(\lambda_1, r) - \alpha_r(\lambda_2, r)) \quad (1)$$

3 with the difference

$$4 \quad \Delta\sigma = \sigma_{O_3}(\lambda_1) - \sigma_{O_3}(\lambda_2)$$

5 of the absorption cross sections of ozone. P is the power returning from the atmosphere ("lidar signal"), β the
6 total backscatter coefficient and α_r the residual extinction coefficient that includes Rayleigh and particle
7 scattering as well as absorption by molecules other than ozone. In the absence of aerosols and interfering gas Eq.
8 1 reduces to:

$$9 \quad n_{O_3}(r) = -\frac{1}{\Delta\sigma} \left(\frac{1}{2} \frac{d}{dr} \ln \left(\frac{P(\lambda_1, r)}{P(\lambda_2, r)} \right) + (\alpha_R(\lambda_1, r) - \alpha_R(\lambda_2, r)) \right), \quad (2)$$

10 the subscript R denoting "Rayleigh". The Rayleigh extinction coefficients can be calculated in the ultraviolet
11 spectral region with relative uncertainties less than 1 % if radiosonde data are used for deriving the atmospheric
12 density. For short "on" wavelengths (266 nm, 277 nm) the absorption of the radiation by ozone dominates the
13 extinction coefficients and, thus, the uncertainty due to the Rayleigh term is, therefore, negligible.

14 Under the clean-air conditions prevailing at Garmisch-Partenkirchen Eq. 2 is mostly a reasonable approximation.
15 However, occasionally aerosol corrections must be made. Due to the large wavelength separation in UV ozone
16 DIALs the inference by aerosols may contribute more seriously than in DIAL systems measuring species with a
17 well-resolved line structure allowing the use of neighbouring wavelengths. Operational procedures based on
18 iterative parameter search were developed that are in detail described in our preceding publication (Eisele and
19 Trickl, 2005). For calculating ozone in the presence of structured aerosol distributions the lowest errors have
20 been obtained for the wavelength pair 277 nm – 292 nm, followed by 277 nm – 313 nm and 292 nm – 313 nm.
21 The most important factor is a strong absorption cross section of ozone, and then a minimum (but finite)
22 wavelength difference (Völger et al., 1996; Eisele and Trickl, 2005), in contrast to a frequently heard, but
23 obviously wrong opinion.

24 Our numerical approach was significantly modified with respect to that published earlier (Kempfer et al., 1994).
25 Previously, the derivatives in the DIAL equation were calculated by fitting third-order polynomials to the
26 backscatter profiles within a given evaluation interval. This method worked rather well, but was slow. A faster
27 modified approach resulted in small steps in the generated ozone profiles requiring to apply some moderate data
28 smoothing in addition (Kempfer et al., 1994).

29 From the point of view of numerical filter theory polynomials are not ideal because their transfer functions
30 expose ringing. We decided to calculate the derivative with a simple linear least-squares fit of just a short
31 interval keeping the vertical resolution (see further below) at about 50 m, followed by optimized numerical
32 filtering. A five-step algorithm is applied, consisting of

- 33 (1) data pre-smoothing at a level roughly corresponding to the chosen minimum vertical resolution of 50 m
34 (important for smooth aerosol retrievals for the near-field telescope),
- 35 (2) calculation of the derivative with a constant number of data points in a sliding interval,
- 36 (3) range-dependent data smoothing with a vertical resolution of about 50 m at low altitudes and 250 m to 500
37 m in the tropopause region, depending on the noise level of the respective measurement,

1 (4) truncation of the uppermost ozone profiles is truncated at an altitude below the onset of diverging noise, in
 2 summer sometimes even below the tropopause,

3 (5) final minor smoothing of the composite ozone profile put together from the best segments of the partial
 4 ozone profiles from different wavelength combinations and the two telescopes.

5 The smoothing intervals in step 3 have been mostly minimized in order not to suppress existing ozone structures.

6 For a linear fit and equidistant data points the result of the fits may be expressed in a rather simple formula,
 7 resulting in the following solution of the DIAL equation for the i^{th} data point (Vogelmann and Trickl, 2008).

8 Selecting a fit interval between data point $i - k$ and $i + k$ one obtains

$$9 \quad \frac{d}{dr} \ln q_i \approx \frac{3}{\langle q_i \rangle \Delta r} \frac{\sum_{j=i-k}^{i+k} (j-i) q_j}{k(k+1)(2k+1)}, \quad (3)$$

11 with the signal ratio

$$12 \quad q_i = \frac{P(\lambda_{on}, r_i)}{P(\lambda_{off}, r_i)} \quad \text{and} \quad \langle q_i \rangle = \frac{\sum_{j=i-k}^{i+k} q_j}{2k+1},$$

13 Δr being the size of the range bin of the transient digitizer or photon-counting system. Application of Eq. 3
 14 allows a fast computation of the derivative, in particular for constant k , when only the sum in the numerator must
 15 be calculated for each step. In Eq. 3 $\langle q_i \rangle$ is written instead of q_i as by Vogelmann and Trickl (2008). This is
 16 explained further below.

17 Another important advantage of Eq. 3 is that the least-squares fit is not applied to the logarithm, but to the signal
 18 ratio itself, due to the transformation

$$19 \quad \frac{d}{dr} \ln q_i = q_i^{-1} \frac{d}{dr} q_i.$$

20 In contrast to the noise of the logarithm of q_i the noise of the signal ratio is symmetrical and fulfils a key
 21 prerequisite of least-squares fitting. A negative density ozone bias is, therefore, avoided.

22 However, the application of Eq. 3 has limitations. Its application to simulated lidar profiles revealed that there
 23 are numerical biases with growing interval sizes $2k$. This is further discussed below.

24 The linear approach in Eq. 3 is reasonable for interval sizes $L = 2k \Delta r$ not exceeding a scale representing the
 25 ozone distribution. Eq. 3 is reasonable choice for data smoothing, but it is not a perfect frequency filter and
 26 transmits residual high-frequency noise. Therefore, we have used a combination of Eq. 3 in a limited interval and
 27 numerical low-pass filtering.

28 Numerical low-pass filtering of data points y_i is based on the general equation (Eisele, 1997; and references
 29 therein)

$$30 \quad y'_i = \sum_{j=i-k}^{i+k} a_j y_{i \rightarrow j} \quad (4)$$

31 with the smoothed value y'_i and the coefficients

$$a_j = a_{-j} = N \frac{\sin(2\pi j f_c f_s^{-1})}{j\pi}$$

1 ;

2 f_c and f_s being the cut-off and sampling frequencies, respectively, and N a normalization factor. The interval
3 width is $L = 2 k \Delta r = 2 k c f_s^{-1}$. One general problem with numerical low-pass filtering is the occurrence of
4 ringing. This can be minimized by introducing window functions w_j

$$5 \quad y'_i = \sum_{j=-k}^k a_j w_j y_{i-j} . \quad (5)$$

6 After comparing several listed window functions a Blackman-type window (Blackman and Tukey, 1959) was
7 chosen:

$$8 \quad w_j = 0.42 + 0.50 \cos(\pi \frac{j}{k}) + 0.08 \cos(2\pi \frac{j}{k}). \quad (6)$$

9 The best performance was achieved by selecting

$$10 \quad f_c = \frac{f_s}{2 k} = \frac{c}{2 k \Delta r} , \quad (7)$$

11 c being the speed of light. The response function obtained for applying Eqs. 5 – 7 with $k = 25$ is depicted in Fig.
12 12 together with that for a sliding arithmetic mean over $2 k + 1 = 51$ symmetrically arranged data points. A
13 linear least-squares fit is equivalent to the arithmetic mean. These linear operations, though suitable for
14 smoothing, are not perfect frequency filters and, therefore, transmit residual high-frequency noise. More details
15 on the frequency transfer functions for some filters are given by Eisele (1997), and, more recently, by Iarlori et
16 al. (2015) and Leblanc et al. (2016).

17 The vertical resolution can be defined in a number of ways (Iarlori, 2015; Leblanc, 2016). For practical reasons
18 the German Engineering Society (Verein Deutscher Ingenieure, VDI, 1999) introduced a definition of the range
19 resolution as the the interval between 25 % and 75 % of the rise of the response to a Heaviside step (Fig. 12).
20 Here, the response reaches a signal level of 100 % at large distances from the step. Since the VDI guideline was
21 published we have preferred to apply this definition. In spectroscopy, mostly a response to a delta peak and its
22 full width at half maximum is used to define spectral resolution. As we can see in Fig. 12 without normalization
23 the delta response is much smaller than the original one, which looks strange in practise.

24 From Fig. 12 we derive for the Blackman filter a VDI vertical resolution of 19.2 % of the full filtering interval L .
25 The response of the Blackman filter to a single-channel (“delta”) peak ($5 \times 10^{17} \text{ m}^{-3}$ to $1 \times 10^{18} \text{ m}^{-3}$) was found to
26 exhibit a full width at half maximum of 34.3 % of L (Fig. 12). This fraction looks surprisingly large in
27 comparison with the step response. The fractions for the pure Blackman filter (Eqs. 5, 6) are also valid for much
28 smaller smoothing intervals than in this example.

29 We also give in Fig. 3 an example for numerical differentiation of a simulated lidar measurement based on Eq. 3.
30 The DIAL equation was synthesised for the wavelength pair 277 – 313 nm, based on the artificial ozone density
31 step between bins 999 and 1000 and on an air density profile calculated from the U.S. Standard Atmosphere
32 (1976). The absence of particles and absorbing molecules other than ozone was assumed. The application of Eq.
33 3 yields a similar step (Fig. 3) that matches that for the Blackman filter within most of the rise if one selects $k =$
34 27. In contrast to an ideal filter the derivative filter transmits some residual noise. The VDI vertical resolution is
35 about 45 % of the filtering interval ($k = 10$ to 30 , presumably in a wider k range).

1 It is important to note that due to the curvature of the backscatter profiles Eq. 3 yields a bias that is absent in the
2 case of missing Rayleigh scattering. This bias grows with k , and is negative for Eq. 3 (for $k = 27$: -0.0050×10^{17}
3 m^{-3} (-0.10%) ahead the step and $-0.0033 \times 10^{18} \text{m}^{-3}$ (-0.33%) behind it). This bias is small, and it becomes
4 even negligible for, e.g., $k = 10$ (and less). However, it grows with k . Thus, it is reasonable to use moderate
5 values of k for the derivative and subsequent numerical filtering with Eqs. 5 and 6 to remove the residual noise.
6 Finally, the use of q_i instead on $\langle q_i \rangle$ in the denominator of Eq. 3 yields a positive bias larger than the negative
7 one for using Eq. 3. This justifies the choice of $\langle q_i \rangle$. One could think about an empirical mathematical
8 correction interpolating between q_i and $\langle q_i \rangle$.

9 The filter interval for the smoothing is dynamically enhanced with height applying a linear relation for simplicity
10 (a quadratic dependence might be better). The coefficients c_1, c_2 are pre-selected for each wavelength pair,
11 $k = c_1 + c_2 * i$ for bin i .

12 For example, for the large telescope of the stationary lidar $c_1 = 0, c_2 = 0.125$ for the pair 277 – 313 nm, $c_1 = 0, c_2$
13 $= 0.156$ for 292 – 313 nm. This results in filtering intervals $2k$ of the order of 250 and 500 near the upper end of
14 the respective useful range (VDI vertical resolutions of 360 m and 720 m, respectively). These preset
15 coefficients are used for the initially automatically produced set of quick-look profiles, but are afterwards
16 reduced in size in some subranges if allowed by the noise level. In ranges with clearly distinguishable ozone
17 gradients (e.g., stratospheric intrusion peaks or tropopause) or strong narrow features the vertical resolution is
18 also reduced as far as reasonable. In particularly noisy subranges in the upper troposphere sometimes
19 homogeneously distributed ozone is fitted to the corresponding density segments. The different segments are
20 pasted into the actual overall ozone profile.

21 As a consequence of this complexity, a solution for automatically deriving uncertainties for all partial data
22 segments has been postponed. In the early 1990s uncertainties for the much less sophisticated evaluation
23 procedure had been calculated from the least-squared fitting approach applied (Kempfer, 1992).

24 The calculation of mixing ratios and the retrieval of aerosol backscatter coefficients require the knowledge of the
25 atmospheric density. Within the troposphere this is not extremely important and simple annual average density
26 profiles do not contribute more than a few per cent to uncertainty (Carnuth et al., 2002). However, with growing
27 data quality and a range reaching the stratosphere the incorporation of a better density profile became mandatory.
28 This is achieved by importing the radiosonde data for the nearest-by station of the German Weather Service,
29 Munich or Stuttgart, from the University of Wyoming data base ([http://weather.uwyo.edu/upperair/
30 sounding.html](http://weather.uwyo.edu/upperair/sounding.html)).

31 313-nm aerosols backscatter coefficients have been routinely calculated for each measurement since 2007 based
32 on the methods mentioned above (Eisele and Trickl, 2005). They are publically available for all years starting in
33 2007 from the EARLINET data base (<https://data.earlinet.org/>).

34 The quality of the aerosol backscatter coefficients for the latest period of lidar operation has been extremely high
35 during most of the day, as can be seen in (Trickl et al., 2015) and in Sect. 7.1. This has served as an additional
36 quality criterion for the ozone retrieval, together with the comparison of the DIAL profiles for different
37 wavelength combinations and the single-wavelength ozone retrieval for 292 nm. In absence of aerosol this single
38 channel is extremely reliable and, in summer, less noisy than the DIAL solution for 292 – 313 nm. However, the
39 Rayleigh backscatter coefficients must be calculated from radiosonde data in order to achieve good quality.

40 After the introduction of the 7400 PMTs, a slight correction of the far-field 313-nm profiles became necessary
41 during the hours around noon (Sect. 4.4). The overshoot of the normally negative signal is particularly
42 pronounced in summer due to the PMT overload effects in the presence of a daylight background exceeding 1

1 mV. Aerosol retrievals mostly perfect during night-time; just a constant displacement of the order of 10^{-7} m^{-1}
2 sr^{-1} must be corrected. As the 313-nm PMT starts to exhibit overshoot for large distances a mathematical
3 correction becomes necessary, in summer even before 10 CET. In the absence of aerosol in the upper
4 troposphere and the lower stratosphere the corrections can be nicely verified by comparing the DIAL ozone with
5 the 292-nm single-signal ozone retrieval.

6 **6. System Validation and Measurements**

7 **6.1 Calibration**

8 Since the first measurement series in 1991 the ozone data have been calibrated by using the absorption cross
9 sections from the University of Reims (Daumont et al., 1992; Malicet et al., 1995). The motivation for this is
10 described Kempfer et al. (1994). Most importantly, the measurements account for the decomposition of ozone
11 during the absorption measurements by precise pressure measurements. The cross sections have measured again
12 and again (e.g., Gorshelev et al., 2014; Serdyuchenko et al., 2014; and references therein), but no improvement
13 has been achieved, except for, perhaps, the temperature dependence. Very recently, four new cross sections
14 measured between 244 nm and 254 nm at an uncertainty level of 0.1 % have been provided by Viallon et al.
15 (2015). In view of the choice for our ozone DIALs it is extremely satisfactory that the agreement with the
16 corresponding values in the Reims data is within ± 0.06 %.

17 The temperature dependence as a function of altitude is obtained by interpolation of the cross sections from
18 Reims measured for different temperatures.

19 **6.2 Validation**

20 For the convenience of data users, the system performance is summarized in Table 4 for the different periods of
21 operation. The uncertainties have been derived from validation exercises, sensitivity studies in low-signal ranges
22 and noise estimates and reproducibility of the ozone densities during diurnal series of measurements.

23 The lidar system has been systematically validated (since 2007 on each sounding day) by using the in-situ data
24 from the nearby mountain stations Wank (1780 m a.s.l.) and Zugspitze (2962 m a.s.l.) until the measurements at
25 these sites were discontinued (evaluated data are available until 2010). Afterwards, the ozone values of the
26 Schneefernerhaus (UFS) Global Atmosphere Watch station have been used for occasional comparisons (Trickl et
27 al., 2014; 2020). UFS is located in the southern face of Zugspitze, at a distance of 9 km from the ozone DIAL at
28 IFU. The gas inlet is at 2670 m. The average ozone mixing ratios are about 1 % lower than those at the summit
29 (Ludwig Ries, personal communication). The lidar data agree similarly well with those from UFS as previously
30 with the Zugspitze ozone.

31 In addition, a large number of successful comparisons have been made with the Hohenpeißenberg ozone sondes
32 (distance: 38 km), a few examples were given by Eisele et al. (1999). A more extensive comparison is planned
33 for the 2018 data, accompanied by a highly successful comparison with a sonde launched by colleagues from
34 Jülich directly at IMK-IFU in February 2019. The latter side-by-side comparison for mixing ratios of about 50
35 ppb yielded a rather constant, bias of the sonde of 2 to 3 ppb up to 7 km and, above this, a slightly higher
36 variability of the differences.

37 These comparisons have certain limitations. In the case of the Hohenpeißenberg sondes the air-mass difference
38 matters in certain altitude ranges due to a 48 km distance between both stations. Under comparable conditions
39 the differences between the profiles have been between 5 and 10 %.

1 The lidar has shown a slightly positive bias with respect to the Wank site, mostly not exceeding 5 ppb. This bias
2 is not present during night-time, but mostly forms in the morning under warm conditions. It has, therefore, been
3 ascribed mostly to slope winds (Carnuth and Trickl, 2000, Fig. 5) venting morning-type low-ozone air from the
4 valley up this rather isolated summit that acts like a chimney. Frequently the summer-time morning values agree
5 better with the 5:00 CET measurement than with the Wank mixing ratio for the true data-acquisition time. Until
6 2011 some alignment issues could occasionally exist that enhanced the uncertainty for distances below 0.5 km.
7 The Wank site has been invaluable for verifying good alignment of the near-field telescope, until 2011 resulting
8 in problems.

9 The comparisons with the Zugspitze in-situ data have been mostly very convenient. The differences of the
10 mixing ratio have rarely exceeded 2 ppb, exceptions typically occurring if there is a pronounced ozone gradient
11 around 3000 m. In absence of an extended comparison since 2012 an example from a four-day series in May
12 1999 (Trickl et al., 2003; 2011) is shown in Fig. 13 that exhibits more noise than recent comparison. The data are
13 compared for two lidar altitudes, 2970 m and 2786 m. The lower altitude accounts for the air-mass rise during
14 the final approach towards the high mountain. The results for 2970 m show a few positive departures that results
15 in a positive average difference between lidar and station of 0.82 ppb (standard deviation: 2.15 ppb). For the
16 lower altitude the “bias” is just 0.34 ppb (standard deviation: 1.61 ppb). These values are all small in comparison
17 with the average Zugspitze mixing ratio, but its sign agrees with the expectation for the 1.8-% bias of the in-situ
18 measurements obtained in the recent cross-section study by Viallon et al. (2015).

19 The performance of the mobile system is discussed in Sect. 5.5.

20 **6.3 Interference by Other Gases**

21 Important species absorbing in the typical wavelength range of ozone DIAL systems are SO₂, NO₂ and some
22 hydrocarbons. Under the clean-air conditions prevailing at the Alpine site Garmisch-Partenkirchen and in the
23 free troposphere spectral interference from these constituents should be very rare. As mentioned, for the mobile
24 DIAL retrievals for the wavelength pair 266 – 299 nm are almost insensitive with respect to SO₂ and NO₂.

25 Oxygen must be also considered in the wavelength region below 285.66 nm (Krupenie, 1972; Jeunouvrier et al,
26 1999). The absorption cross sections of O₂ in this region (Herzberg bands) are rather low, but absorption cannot
27 be completely neglected due to the high concentration of this molecule. We found some approximate
28 coincidences with not relevant high rotational levels, and an approximate coincidence of the 277.11 nm emission
29 with J = 5-7 components of the extremely weak A' → X (2,0) band. 266.12 nm is slightly outside a group of O₂
30 lines. In summary, absorption of the emissions used in the two DIAL systems in oxygen can be neglected, in
31 agreement with the good validation results.

32 **7. Measurements**

33 **7.1 Examples for the Stationary System**

34 After the first upgrading of the stationary DIAL in 1994 and 1995 the system yielded a greatly improved
35 sensitivity and a much larger vertical range up to about 15 km due to the tree-wavelength operation. The number
36 of measurements per year grew and time series under automatic control were extended up to four days, the first
37 four-day series being the well-documented one in May 1996 published by Eisele et al. (1999), Stohl et al. (2000),
38 Cristofanelli et al. (2003) and Trickl et al. (2003). However, until 2003 the operation was limited to funded
39 projects and focussed research topics. After the second major system upgrading routine measurements were
40 started in 2007. Almost 5000 ozone profiles were obtained from 1991 to February 2019, numerous examples can

1 be found in our publications (see Appendix, the most recent one, on the period 2007 to 2016, being (Trickl et al.,
2 2020)).

3 A summary of the work done is given in Table 3. Uncertainties estimated for the different periods and altitude
4 ranges are specified in Table 4 as a guide for potential data users.

5 Figure 14 shows the raw backscatter signals (a) uncorrected and (b) with automatic exponential correction. The
6 amplitudes of the corrections grow with the area of the backscatter signal that is larger for the far-field telescope
7 than for the near-field telescope and grows with the wavelength due to the decreasing absorption cross section.
8 In the range where such an exponential wing affects the lidar signal it does not exceed a few times 10^{-5} of the
9 input voltage range (100 mV). The slightly enhanced noise in channel 6 (313 nm, red curve) is caused by the
10 early-morning daylight roughly one hour after sun rise.

11 The introduction of three-wavelength operation made possible an internal quality assurance. Ozone profiles are
12 derived from different wavelength combinations. The observation of mutual deviations in the retrieved densities
13 results in immediate re-examination of the alignment. As mentioned just two misalignments matter: the overlap
14 of the partial beams emerging from the Raman shifters after recombination and the pointing of the beam emitted
15 into the atmosphere. Minor discrepancies for 292 – 313 nm due to alignment drifts during extended periods of
16 unattended operation can be conveniently recalibrated by using the 277 – 313-nm profiles as a reference, which
17 was routinely done in recent years. As mentioned the 277-nm channel of the large telescope was found to be
18 insensitive to slight misalignments presumable due to the particularly small focal point in the entrance slit of the
19 spectrograph. In addition, small drifts in laser pointing are do not result in a transverse displacement of the spot
20 on the detectors that are placed in the image planes of the principal mirror of the telescope.

21 One example for a measurement for a perfectly aligned lidar is shown in Fig. 15 (26 October 2015). The figure
22 contains three ozone profiles from both receivers. The three ozone profiles match well in their common overlap
23 regions. Nevertheless, due to low ozone the near-field signal (here 277 – 313 nm) yields reasonable ozone values
24 up to 2.5 km above the ground (740 m a.s.l.). The range for same wavelength pair in the large receiver extends
25 up to 6.5 km a.s.l., with moderately elevated ozone. The simultaneously measured ozone value at UFS is lower
26 by just 0.7 ppb. The 292 – 313-nm ozone profile exhibits less structure than that for 277 – 313 nm. The
27 absorption cross section for 292 nm is less than one quarter of that for 277 nm, which necessitates smoothing the
28 292 – 313-nm ozone over larger intervals (Sect. 5). In the uppermost part of the red curve a 292-nm single-
29 wavelength retrieval was applied that reduces the noise inferred by the 313-nm profile, but otherwise agrees with
30 the DIAL solution. Such a retrieval is not possible in the presence of aerosol or clouds.

31 The ozone hump between 3.0 and 4.7 km is caused by a very dry layer (1 % minimum relative humidity at 4.2
32 km for the Munich radiosonde (100 km roughly to the north; 1% is an artificial cut-off in the listings for the
33 RS92 radiosonde (Trickl et al., 2014)). 315-h backward trajectories calculated with the HYSPLIT model
34 (Draxler and Hess, 1998; http://ready.arl.noaa.gov/HYSPLIT_traj.php), selecting re-analysis meteorological
35 data, suggest a long-range descent from the stratosphere over western Canada. The Munich thermal tropopause
36 for both standard launch times is significantly higher than the onset of the ozone rise. It is well known, also from
37 our measurements, that the thermal tropopause does not perfectly coincide with the onset of the ozone rise
38 (Hoerling et al., 1991; Pan et al., 2004).

39 In general, as pointed out in Sect. 4.2, the near-field receiver yields reasonable ozone typically up to at least 2
40 km above the ground (2.74 km a.s.l.). The quality is limited due to the rapid drop of the backscatter signal. The
41 useful range for 277 nm of the far-field receiver is 6.5 to 8 km in winter (40 to 50 ppb). 292 nm is rarely used in
42 the lower troposphere because of the lower sensitivity for ozone and the stronger sensitivity to aerosol (Eisele

1 and Trickl, 2005). However, the 277 – 292-nm profiles are preferred the presence of pronounced aerosol
2 structures because of a less critical aerosol correction. The typical range for 292 nm is roughly 3 km above the
3 tropopause, which can vary with the slope of ozone rise. In summer, when ozone in the free troposphere can
4 exceed 100 ppb, sometimes the range is limited to 10 to 11 km and the seasonally higher tropopause is not
5 reached due to the strong loss of radiation.

6 Due to the short measurement time of just 41 s the reproducibility of the data can be easily verified. In Figure 16
7 we show the profiles for three measurements under complex conditions (Saharan dust up to 4 km and a
8 stratospheric air intrusion around 5.7 km) obtained within less than three minutes on 18 June 2013. The intrusion
9 originated at 10 km or more over the United States at least 13 days backward in time (Trickl et al, 2020). The
10 layer descended to southern Spain and then turned north-eastward towards the Alps, slightly rising. Due to the
11 long travel the minimum relative humidity was as high as 6 %, as measured by both our water-vapour DIAL and
12 the Munich radiosonde (Trickl et al., 2020).

13 Due to elevated ozone mixing ratios (50 to 80 ppb) the radiation loss results in an increase of the short-term
14 variability of the ozone profiles in the upper troposphere which indicates a level of uncertainty of about ± 10 ppb.
15 The noise of the 277-313-nm ozone values strongly increases above 5.5 km, where the data from the 292-313-
16 nm pair are used.

17 With the latest PMT version (2012) the far-field performance of the lidar during the warm season decreases
18 around noon due to the growing daylight background at 313 nm and the resulting nonlinearity. The 313-nm
19 constant background is largest in the presence of clouds. The signal must be corrected mathematically (Sect. 5)
20 to achieve both a quantitative ozone profile and a reasonable aerosol retrieval with zero aerosol in clean parts of
21 the atmosphere. The DIAL result based on the corrected 313-nm data is then also compared with the 292-nm
22 single-trace ozone retrieval and usually agrees well. These comparisons demonstrate the value of simultaneously
23 evaluating aerosol and O_3 . For the strongest ozone mixing ratios (exceeding 100 ppb in the middle and upper
24 troposphere) the range of the system may be limited to about 10 km and the stratospheric ozone rise is missed.

25 The best results are achieved in winter due to low ozone and low solar background. In Fig. 18 we give as an
26 example the measurements on 13 February 2014. The measurements were limited to the morning hours due to
27 the arrival of clouds ahead of a cold front, just before 11:00 CET. The profiles coincide extremely well outside
28 two dry layers (1 CET Munich radiosonde, 4 to 12 % and 6 % RH, respectively) in the lower free troposphere
29 and above 6 km that might be associated with the slightly elevated ozone at 8:00 CET around 3.8 km and 6.1
30 km, respectively. The tiny peak at 6.1 km at 8:35 CET does not significantly exceed the uncertainty level in that
31 altitude range. However, in addition to the low RH around 1 CET the corresponding HYSPLIT trajectories indi-
32 cate for both layers a descent over at least 13 d from high altitudes over the North Pacific, confirming the idea of
33 stratospheric intrusions. Intrusions with just a low rise in ozone are not rare during the cold season (Trickl et al.,
34 2020). They can be resolved at least in the range covered by the less noisy 277 – 313-nm wavelength pair.

35 In Fig. 19 examples of aerosol retrievals of ozone-corrected 313-nm backscatter profiles during the brightest
36 period of the year are shown. A constant backscatter-to-extinction ratio of 0.020 sr^{-1} was applied. Backscatter
37 coefficients of $(1-3) \times 10^{-6} \text{ m}^{-1} \text{ sr}^{-1}$ are typical of the warm season at this site unless there is a strong Saharan
38 dust or fire event. Here, the air masses originate in Italy and eastern Europe. The top altitude of 5 km resembles
39 that for Saharan dust (Jäger et al., 1988; Papayannis et al., 2008), but was caused by orographic lifting during a
40 transport across the Alps almost parallel to the mountains. The free troposphere was free of aerosol on that day
41 which allows one to visualize the low noise of the lidar, at least during the early hours. Aerosol data from
42 ultraviolet channels are usually strongly influenced by the noise of the strong Rayleigh background.

1 In the presence of strong aerosol in the PBL, such as in the case of smoke or pronounced Saharan dust, the
2 signal-to-noise ratio is strongly attenuated. High-aerosol events prevail in summer which adds to lowering the
3 upper-tropospheric performance of the system.
4 Starting in late 2012, the aerosol backscatter coefficients have been archived in the EARLINET data base mostly
5 with a delay of less than one day after the measurements.

6 **7.2 Examples for the Mobile System**

7 ***29 April 1999***

8 The final performance of the mobile system was achieved shortly before its destruction in late May 1999 (Fig.
9 19). It had turned out that a daylight signal background of more than 12 mV was present in the 299-nm channel
10 which lead to signal distortion (Sect. 4.4). Due to inserting a 300 nm cut-off filter, bridging the gap to the 320
11 nm edge of the Corion filter, the 299 nm channels became linear and the planned operating range of the DIAL of
12 4 km could be reached. As mentioned, further range extension would be possible if a rotating attenuator could be
13 used for 299 nm to get roughly equal maximum far-field returns for 289 nm and 299 nm. Below a distance r of
14 2.7 km 266 – 299-nm pairs were taken.

15 In the example of Fig. 19 the range could be extended to a distance $r = 8.3$ km (9.0 km a.s.l.) by evaluating
16 ozone from the much stronger (less noisy) 299-nm signal alone. A slight adjustment of that partial profile had to
17 be made, based on the DIAL results for lower altitudes, which resulted in elevated uncertainties. As can be seen
18 from the edges of the isolated structures smoothing over several hundred metres was applied here.

19 The validation is based just on comparisons with the in-situ measurements at the three local stations operated by
20 IFU. The small deviations from the 11:30 CET Wank and Zugspitze in-situ data also shown in the figure suggest
21 an uncertainty of 2 ppb in this altitude range. For the higher altitudes a comparison is missing because the
22 measurement was made on a Thursday, too early for the Friday morning Hohenpeißenberg ozone sonde ascent.

23 As can be concluded from the rich structure of the ozone profile and the pronounced ozone changes in the in-situ
24 data (we select for Fig. 19 the data for 5:00, 9:30, 11:30, 14:00, and 17:00 CET) the meteorological situation was
25 complex. The situation was characterized prefrontal advection of North American air via Algeria at most
26 altitudes, where the minimum altitude of about 1.5 km was reached. Up to $r = 3.5$ km the ozone profile is
27 difficult to interpret. The ozone peak between 2.5 and 3.0 km is not necessarily caused by a subsiding
28 stratospheric air intrusion: The relative humidity (RH) at the Zugspitze summit rose from 38 % to 66 % until
29 17:00 CET, when the Zugspitze ozone reached the mixing ratio of the 11:30 peak above the summit. Subsidence
30 is not very likely under prefrontal conditions anyway (Trickl et al., 2020). Also contributions from Northern
31 Italy could have been picked up.

32 Above 3.5 km we clearly see a pronounced stratospheric intrusion layer. This view is supported by the very high
33 peak ozone of 113 ppb, the minimum RH of 1 % in the 13:00-CET ascent of the Munich radiosonde and
34 HYSPLIT backward trajectories. The HYSPLIT trajectories revealed descent over more than ten days from the
35 north-western part of North America or beyond.

36 The low upper-tropospheric ozone values are in agreement with the calculated source region 2 km above the
37 Pacific south of Hawaii. Directly above the remote Pacific almost zero ozone has been found (Kley et al., 1996),
38 which justifies to assume 20-30 ppb 2 km above the surface.

39 ***Milano field campaign***

1 The second example is chosen from the VOTALP II (Vertical Ozone Transport in the Alps) “Milano” field
2 campaign in 1998, in a joint effort together with the PIPAPO (Pianura Padana Produzione di Ozono) air-quality
3 campaign around Milano (Italy) (more details on the measurements: Trickl, 2010). The mobile ozone DIAL was
4 operated at Barni (Provincia di Como) within the first mountain range of the Alps, about 40 km north of Milano
5 between 1 and 5 June 1998. On the first four days a day-by-day increase of the afternoon peak ozone advected
6 from the Milano metropolitan area to Barni by the daytime up-valley wind was observed. During each night the
7 O₃ mixing ratio dropped to roughly 60 ppb due to the reversal of the orographic wind direction.
8 Figure 20 shows the situation for the day with the highest ozone values, 4 June. The behaviour of the ozone rise
9 was surprisingly similar to that on the previous days, including the bimodal profile at 13:36 CET (Central
10 European Time = UTC + 1 h). In the late afternoon 120 ppb of ozone were reached, exactly verified by side-by-
11 side measurements with ozone sondes launched by a team from the Swiss Paul-Scherrer Institute. This high
12 mixing ratio turned out to be the very limit for retaining an overlap between the near-field and the far-field 266-
13 nm “on” detection channels for the chosen position of the far-field apertures (blades) and PMT settings. The
14 comparison of the DIAL and the sonde measurements also indicates some air-mass lifting towards the main part
15 of the lake since the boundary-layer height (defined here by elevated ozone) grew as the sonde drifted northward
16 during its ascent. It is interesting to note that the 19:10-CET DIAL profile next to the ground would agree with
17 the sonde profiles for some average position of the two sonde maxima.

18 **8. Discussion and Conclusions**

19 Differential-absorption lidar systems for trace-gas measurements have proved to be an invaluable tool for
20 atmospheric studies (Trickl, 2010). Despite this fact the application of DIAL systems is rather limited, in
21 particular combined approaches. Despite promising developments in Europe within TESLAS in the early 1990s
22 no continental-scale ozone-lidar network could be established. Ozone measurements have been mostly limited to
23 Haute Provence (Gaudel et al., 2015; Tarasick et al., 2019), Garmisch-Partenkirchen and Athens (Kalobakas et
24 al., 2012; Mytilinaios et al., 2018). By contrast, the ozone-lidar network TolNET was implemented in North
25 America (Newchurch et al., 2016).

26 At IMK-IFU (Garmisch-Partenkirchen, Germany) three DIAL systems have been developed since 1988, two for
27 ozone and one for water vapour (Vogelmann and Trickl, 2008). The ozone systems have been used for a large
28 number of focussed investigations until 2003 (e.g., Carnuth et al., 2002; Eisele et al., 1999; Stohl and Trickl,
29 1999; Trickl, 2003; Trickl et al., 2003; 2010; 2011). The stationary ozone and water-vapour lidars, have been
30 used for routine measurements since 2007 (e.g., Trickl et al., 2014; 2015; 2016; 2020). The measurements with
31 the stationary ozone DIAL have yielded a total of almost 5000 evaluated ozone profiles since 1991. In the
32 absence of interruptions in the measurement programme, the typical annual number of evaluated measurements
33 has been of the order of 500 measurements. This number will grow with further growing reliability of the
34 automatically produced quick-look ozone and 313-nm aerosol profiles, due to a diminishing requirement for
35 manual optimization. Manual corrections are, still, required in the presence of high ozone levels, due to the
36 residual daytime issues at 313 nm and in the presence of pronounced aerosol and cloud structures.

37 In the course of three decades of ozone-DIAL development at IMK-IFU we have gradually optimized the
38 technology to a state where even small variations in tropospheric ozone can be sensed with a high level of
39 credibility. A full restriction to analogue data acquisition is possible due to the large dynamic range of the 5600
40 and 7400 Hamamatsu PMTs. Automatic operation was introduced in 1996 (for both systems) although it has
41 been limited to clear weather situations. Thus, the largest effort has been spent for the data evaluation. The

1 results of automatic data evaluation have rarely been directly adopted and careful manual corrections have been
2 made. These corrections include the selection of the best partial profiles based on comparisons and optimizing
3 the vertical resolution in relation to the changing signal-to-noise ratio or when zooming into interesting ozone
4 features. As a consequence of the excellent data quality the full use of automatic data evaluation is now coming
5 within reach at least under conditions of low to moderate aerosol.

6 The quality of the retrieved 313-nm aerosol backscatter coefficients almost matches that traditionally obtained in
7 the green spectral region. Baseline corrections are needed during daytime due to signal distortions caused by the
8 high daylight sensitivity of the 7400 PMTs. Spectral filtering must be improved. Perhaps one of the old 5400
9 PMTs must return to the far-field 313-nm channel.

10 Quite a number of lessons have been learnt:

- 11 – Three-wavelength operation is mandatory: It provides a wide vertical range and internal quality assurance;
12 the aerosol retrieval yields an additional quality control of the 313-nm backscatter profiles.
- 13 – Use of at least one short "on" wavelength below 280 nm is an important base for high accuracy and for a
14 low to moderate level of interference by aerosols that can be readily corrected for. Even for 266 nm a range
15 up to about $r = 2.5$ km above the lidar was demonstrated.
- 16 – A short measurement time of 41 s was achieved with the stationary system whereas for the mobile system
17 about 10 min were necessary. This longer signal accumulation is, in part, due to the slower repetition rate of
18 15 Hz per wavelength for the longer wavelengths, in part also by the strong signal decay for 266 nm (30 Hz
19 repetition rate) that necessitates longer averaging to achieve a reasonable signal-to-noise ratio at larger
20 distances. For the stationary system, longer averaging (e.g., 5 min) will yield better results in the upper
21 troposphere in summer. In principle, the free-tropospheric capability (i.e., without significant amounts of
22 aerosol) can be driven close to the uncertainty limit set by the absorption cross sections.
- 23 – Current-day transient digitizers make single-photon counting in an ozone DIAL almost superfluous, except
24 for very long measurements in dark environment.
- 25 – Simultaneous analogue and PC counting out of a single PMT is possible, but has so far led to a deterioration
26 of the analogue signal that cannot easily be corrected mathematically (see Klanner et al., 2020). Single-
27 photon counting will be resumed if the residual signal distortions can be removed. However, an operation
28 for low PMT supply voltages must be ensured to avoid signal attenuation and excessive averaging.
- 29 – The application of the small Hamamatsu PMTs has allowed the use of higher signal voltage levels (100 mV
30 or more) than in the traditionally used photo tubes. A photon flux as high as possible should be applied in
31 the far field channels since the signal noise is strongly influenced by the photon noise^{*)}. This is an issue if
32 both analogue and photon counting out of the same PMT is chosen because photon counting requires
33 elevated supply voltages of the order of 800 V, too high for strong irradiation.
- 34 – A problem with the Hamamatsu 7400 PMTs not yet fully solved is the high sensitivity with respect to
35 daylight: The background signal must not exceed 1 mV in order to avoid undershot, which can be
36 minimized by higher laser pulse energy (improving the peak-signal-to-background ratio), careful spectral
37 filtering, reducing the slit width at the polychromator entrance, adding another black baffle for the incoming
38 radiation just below the entrance flap in the roof and a very clean surface of the primary mirror of the
39 telescope. Also, for 313 nm, a return to a 5600 PMT can be considered in the far-field receiver.
- 40 – The use of two spatially separated telescopes for near-field-far-field separation is superior to cutting off the
41 near-field portions in the far-field channels as done in the mobile system (and the water-vapour DIAL

1 (Vogelmann and Trickl, 2008)), unless a rotating signal attenuator is used for reducing the stronger “off”
2 return.

3 – An operational calculation of uncertainties is planned, an important requirement for archiving the data in
4 international data bases.

5 *) In the case of the mobile lidar this would have required to enhance the 266-nm pulse energy of the Powerlite
6 9030 laser to the full 120 mJ, or to use a larger receiver (see first example in Sect. 7.2).

7

8 **9 Data availability**

9 Data and information on the lidar systems can be obtained on request from the author of this paper
10 (thomas.trickl@kit.edu., thomas@trickl.de after feb 2020). The 313-nm aerosol backscatter coefficients are
11 archived in the EARLINET data base, accessible through the ACTRIS data portal <http://actris.nilu.no/>.

12 **10 Author statement**

13 TT carried out most lidar measurements after spring 1997, following U. Kempfer and H. Eisele, assisted by HG
14 and MP. He led the technical development of both ozone DIAL systems since 1990. FN was responsible for the
15 technical infrastructure of the mobile system. HG, MP and HV were involved in the system upgrading since
16 2007.

17 **11 Competing interests**

18 The author declares that he has no conflict of interest.

19 **Appendix**

20 **Table A1: List of citations of atmospheric transport studies including ozone lidar systems**

21	Browell et al., 1987	Ancellet et al., 1991	Ancellet et al., 1994	Browell et al., 1996
22	Lamarque et al., 1996	Langford et al., 1996	Newell et al., 1997	Ravetta et al., 1999
23	Eisele et al., 1999	Stohl and Trickl, 1999	Grant et al., 2000	Baray et al., 2000
24	Seibert et al., 2000	Kowol-Santen and Ancellet, 2000	Browell et al., 2001	Carnuth et al., 2002
25	Zanis et al., 2003	Roelofs et al., 2003	Trickl et al., 2003	Galani et al., 2003
26	Papayannis et al., 2005	Leclair De Bellevue et al., 2006	Ravetta et al., 2007	Liang et al., 2007
27	Trickl et al., 2010	Trickl et al., 2011	Kuang et al., 2012	Trickl et al., 2014
28	Trickl et al., 2015	Ancellet et al., 2016	Granados-Muñoz and Leblanc, 2016	
29	Sullivan et al., 2016	Kuang et al., 2017	Granados-Muñoz et al., 2017	Langford et al., 2018
30	Trickl et al., 2020			

31

32 **Table A2: List of citations of some air-quality studies including ozone lidar systems**

33	Durieux et al., 1998	Fiorani et al., 1998	Zhao et al., 1998	Banta et al., 1998
34	Valente et al., 1998	Senff et al., 1998	Thomasson et al., 2002	Kourtidis et al., 2002
35	Duclaux et al., 2002	Couach et al., 2003	Dufour et al., 2005	Simeonov et al., 2005
36	Langford et al., 2009	Senff et al., 2010	Trickl, 2010	Langford et al., 2012
37	Dreessen et al., 2016	Langford et al., 2017	Sullivan et al., 2017	Yates et al., 2017

38

1 **Table A3: List of citations of papers describing ozone DIAL systems**

2 Grant et al., 1975	Browell, 1982	Pelon and Mégie, 1982	Browell et al., 1983
3 Uchino et al., 1983	Ancellet, 1989	McDermid, 1991	Zhao et al., 1992
4 Uthe and Livingston, 1992	Sunesson et al. 1994	Kempfer et al., 1994	Bucreev et al., 1994
5 Bucreev et al., 1996	Grabbe et al., 1996	Reichardt et al., 1996	Eisele and Trickl, 1997
6 Brenner et al., 1997	Ancellet and Ravetta, 1997	Wallinder et al., 1997	Proffitt and Langford, 1997
7 Ancellet and Ravetta, 1998	Alvarez et al., 1998	Veselovskii and Barchunov, 1999	
8 Baray et al., 1999	Matthias, 2000	Lazzarotto et al., 2001	McDermid et al., 2002
9 Fix et al., 2002	Nakazato et al., 2007	Machol et al., 2008	Burlakov et al., 2010
10 Alvarez et al., 2011	Kuang et al., 2011	Kuang et al., 2013	Uchino et al., 2014
11 Sullivan et al., 2014	De Young et al., 2017	Strawbridge et al., 2018	Fix et al., 2019

12 **Acknowledgements**

13 The author thanks Wolfgang Seiler and Hans Peter Schmid for their support over that many years. Walter
14 Carnuth designed the first version of the stationary ozone DIAL that was built by Ulrich Kempfer and Raul Lotz.
15 The decisive upgrading, that included a lot of new approaches, was achieved in co-operation with H. Eisele. The
16 author is indebted to Werner Funk, Bernd Mielke, Heinz Josef Romanski and Bernhard Stein for numerous
17 important discussions and technical improvements of the detection electronics. The valuable contributions during
18 certain periods of the system development by Pietro Brenner, Josef-Michael Burger, Bernd Jänker and Karl
19 Maurer are emphasized. Hans-Eckhart Scheel, Ludwig Ries, Hans Claude, and Wolfgang Steinbrecht have
20 provided reference ozone data for the Wank, Zugspitze and Schneefernerhaus mountain stations in the vicinity of
21 IFU and ozone sonde data for the Hohenpeißenberg observatory of the German weather service. Johannes Keller
22 provided the ozone sonde profiles of the team from the Swiss Paul-Scherrer-Institut for the Milano field
23 campaign. The development of the mobile system was based on a highly efficient co-operation with the company
24 OHB System (Bremen). The different steps of the lidar development have been funded by the German Ministry
25 of Research and Technology (BMFT), the German Foundation for the Environment (DBU, two projects), and the
26 Bavarian Ministry of Economics. Since 2007 the aerosol results have contributed to EARLINET (European
27 Aerosol Research Lidar Network) that is currently a part of the European Research Infrastructure ACTRIS.
28 The service charges for this open access publication have been covered by a Research Centre of the Helmholtz
29 Association.

30 **References**

31 ATMOFAST: Atmosphärischer Ferntransport und seine Auswirkungen auf die Spurengaskonzentrationen in der
32 freien Troposphäre über Mitteleuropa (Atmospheric Long-range Transport and its Impact on the Trace-gas
33 Composition of the Free Troposphere over Central Europe), Project Final Report, T. Trickl, co-ordinator, M.
34 Kerschgens, A. Stohl, and T. Trickl, subproject co-ordinators, funded by the German Ministry of Education and
35 Research within the programme “Atmosphärenforschung 2000“, Forschungszentrum Karlsruhe, IMK-IFU
36 (Garmisch-Partenkirchen, Germany), <http://www.trickl.de/ATMOFAST.htm>, 130 pp., 2005 (in German), with
37 revised publication list 2012
38 Amodeo, A., Bösenberg, J., Ansmann, A., Balis, D., Böckmann, C., Chaikovsky, A., Comeron, A., Mitev, V.,
39 Papayannis, A., Pappalardo, G., Perrone, M. R., Rizi, V., Simeonov, V., Sobolewski, P., Spinelli, N., Stoyanov,

1 D. V., Trickl, T., and Wiegner, M.: EARLINET: the European Aerosol Lidar Network, *Optica Pura y Aplicada*,
2 39, 1-10, 2006.

3 Ancellet, G., Papayannis, A., Pelon, J., and Mégie, G.: DIAL Tropospheric Ozone Measurement Using a
4 Nd:YAG Laser and the Raman Shifting Technique, *J. Atmos. Oceanic Technol.*, 6, 832-839, 1989.

5 Ancellet, G., Pelon, J., Beekmann, M., Papayannis, A., and Mégie, G.: Ground-Based Lidar Studies of Ozone
6 Exchanges Between the Stratosphere and the Troposphere, *J. Geophys. Res.*, 96, 22401-22421, 1991.

7 Ancellet, A., Beekmann, M., and Papayannis, A.: Impact of cutoff low development on downward transport of
8 ozone in the troposphere, *J. Geophys. Res.*, 99, 3451-3468, 1994.

9 Ancellet, A., and Ravetta, F.: The Airborne Lidar for Tropospheric Ozone (ALTO), *Advances in Atmospheric*
10 *Remote Sensing with Lidar, Selected Papers of the 18th International Laser Radar Conference*, Berlin (Germany,
11 1996), A. Ansmann, R. Neuber, P. Rairoux, U. Wandinger, Eds., Springer (Berlin, Heidelberg, New York), 399-
12 402, 1997.

13 Ancellet, A., and Ravetta, F.: Compact airborne lidar for tropospheric ozone: description and field
14 measurements, *Appl. Opt.*, 37, 5509-5521, 1998.

15 Ancellet, G., Pelon, J., Totems, J., Chazette, P., Bazureau, A., Sicard, M., Di Iorio, T., Du Lac, F., and Mallet,
16 M.: Long-range transport and mixing of aerosol sources during the 2013 North American biomass burning
17 episode: analysis of multiple lidar observations in the western Mediterranean basin, *Atmos. Chem. Phys.*, 16,
18 4725-4742, 2016.

19 Alvarez II, R. J., Senff, C. J., Hardesty, R. M., Parrish, D. D., Like, W. T., Watson, T. B., Daum, P. H., and
20 Gillani, N.: Comparisons of airborne lidar measurements of ozone with airborne in situ measurements during the
21 1995 Southern Oxidants Study, *J. Geophys. Res.*, 103, 31155-31171, 1998.

22 Alvarez II, R. J., Senff, C. J., Langford, A. O., Weikmann, A. M., Law, D. C., Machol, J. L., Merrit, D. A.,
23 Marchbanks, R. D., Sandberg, S. P., Brewer, W. A., Hardesty, R. M., and Banta, R. M.: Development and
24 application of a compact, tunable, solid-state airborne ozone lidar system for boundary layer profiling, *J. Atmos.*
25 *Ocean. Technol.*, 28, 1258-1271, 2011.

26 Banta, R. M., Senff, C. J., White, A. B., Trainer, M., McNider, R. T., Valente, R. J., Mayor, S. D., Alvarez, R. J.,
27 Hardesty, R. M., Parrish, D., and Fehsenfeld, F. C.: Daytime buildup and nighttime transport of urban ozone in
28 the boundary layer during a stagnation episode, *J. Geophys. Res.*, 103, 22519-22544, 1998.

29 Baray, J.-L., Leveau, J., Porteneuve, J., Ancellet, G., Keckhut, P., Posny, F., and Baldy, S.: Description and
30 evaluation of a tropospheric ozone lidar implemented on an existing lidar in the southern subtropics, *Appl. Opt.*,
31 38, 6808-6817, 1999.

32 Baray, J.-L., Daniel, V., Ancellet, G., and Legras, B.: Planetary-scale tropopause folds in the southern
33 subtropics, *Geophys. Res. Lett.*, 27, 353-356, 2000.

34 Blackman, R. B., and Tukey, J. W.: in: *The Measurement of Power Spectra, From the Point of View of*
35 *Communications Engineering*, Dover, Publications, New York, U.S.A., 95-101, 1959.

36 Brenner, P., Reitebuch, O., Schäfer, K., Trickl, T., and Stichternath, A.: A Novel Mobile Vertical-sounding
37 System for Ozone Studies in the Lower Troposphere”, *Advances in Atmospheric Remote Sensing with Lidar*,

1 Selected Papers of the 18th International Laser Radar Conference, Berlin (Germany, 1996), A. Ansmann, R.
2 Neuber, P. Rairoux, U. Wandinger, Eds., Springer (Berlin, Heidelberg, New York), 383-386, 1997.

3 Browell, E. V.: Lidar measurements of tropospheric gases, *Opt. Eng.*, 21, 128-132, 1982.

4 Bragg, S. L., Brault, J. W., and Smith, W. H.: Line Positions and Strengths in the H₂ Quadrupole Spectrum,
5 *Astrophys. J.*, 263, 999-1004, 1982.

6 Browell, E. V., Carter, A. F., Shipley, S. T., Allen, R. J., Butler, C. F., Mayo, M. N., Siviter, J. H., and Hall, W.
7 M.: NASA multipurpose airborne DIAL system and measurements of ozone and aerosol profiles, *Appl. Opt.*, 22,
8 522-534, 1983.

9 Browell, E. V., Danielsen, E. F., Ismail, S., Gregory, G. L., and Beck, S. M.: Tropopause Fold Structure
10 Determined From Airborne Lidar and in Situ Measurements, *J. Geophys. Res.*, 92, 2112-2120, 1987.

11 Browell, E. V., Fenn, M. A., Butler, C. F., Grant, W. B., Merrill, J. T., Newell, R. E., Bradshaw, J. D.,
12 Sandholm, S. T., Anderson, B. E., Bandy, A. R., Bachmeier, A. S., Blake, D. R., Davis, D. D., Gregory, G. L.,
13 Heikes, B. G., Kondo, Y., Liu, S. C., Rowland, F. S., Sachse, G. W., Singh, H. B., Talbot, R. W., and Thornton,
14 D. C.: Large-scale air mass characteristics observed over the Western Pacific during summertime, *J. Geophys.*
15 *Res.*, 111, 1691-1712, 1996.

16 Browell, E. V., Fenn, M. A., Butler, C. F., Grant, W. B., Ismail, S., Ferrare, R. A., Kooi, S. A., Brackett, V. G.,
17 Clayton, M. B., Avery, M. A., Barrick, J. D. W., Fuelberg, H. E., Maloney, J. C., Newell, R. E., Zhu, Y.,
18 Mahoney, M. J., Anderson, B. E., Blake, D. R., Brune, W. H., Heikes, B. G., Sachse, G. W., Singh, H. B., and
19 Talbot, R. W.: Large-scale air mass characteristics observed over the remote tropical Pacific Ocean during
20 March – April 1999: Results from the PEM-Tropics B field experiment, *J. Geophys. Res.*, 106, 32481-32501,
21 2001.

22 Buceev, V. S., Vartapetov, S. K., Veselovskii, I. A., Galustov, A. S., Kovalev, Y. M., Prokhorov, A. M.,
23 Svetogorov, E. S., and Khmelevtsov, S. S., and Lee, C. H.: Excimer-laser-based lidar system for stratospheric
24 and tropospheric ozone measurements, *Quantum Electronics*, 24, 546-551, 1994; translated from *Kvantova*
25 *Electronica*, 21, 591-596, 1994.

26 Buceev, V. S., Vartapetov, S. K., Veselovskii, I. A., Galustov, A. S., Kovalev, Y. M., Svetogorov, E. S., and
27 Khmelevtsov, S. S.: Combined lidar system for stratospheric and tropospheric ozone measurements, *Appl. Phys.*
28 *B*, 62, 97-101, 1996.

29 Burlakov, V. D., Dolgii, S. I., Makeev, A. P., Nevzorov, A. V., Romanovskii, O. A., and Kharchenko, O. V.: A
30 Differential-Absorption Lidar for Ozone Sensing in the Upper Atmosphere – Lower Stratosphere, *Instruments*
31 *and Experimental Techniques*, 53, 886-889, 2010.

32 W. Carnuth, T. Trickl, Transport studies with the IFU three-wavelength aerosol lidar during the VOTALP
33 Mesolcina experiment, *Atmos. Environ.*, 34, 1425-1434, 2000.

34 Carnuth, W., Kempfer, U., and Trickl, T.: Highlights of the tropospheric lidar studies at IFU within the TOR
35 project, *Tellus B*, 54, 163-185, 2002.

36 Couach, O., Balin, I., Jiménez, R., Ristori, P., Perego, S., Kirchner, F., Simeonov, V., Calpini, B., and van den
37 Berg, H.: An investigation of ozone and planetary boundary layer dynamics over the complex topography of
38 Grenoble combing measurements and modelling, *Atmos. Chem. Phys.*, 3, 549-562, 2003.

- 1 Cristofanelli, P., Bonasoni, P., Collins, W., Feichter, J., Forster, C., James, P., Kentarchos, A., Kubik, P. W.,
2 Land, C., Meloen, J., Roelofs, G. J., Siegmund, P., Sprenger, M., Schnabel, C., Stohl, A., Tobler, L., Tositti, L.,
3 Trickl, T., and Zanis, P.: Stratosphere to troposphere transport: a model and method evaluation, *J. Geophys.*
4 *Res.*, 108, 8525, doi: 10.1029/2002JD002600, STA 10, 23 pp., 2003.
- 5 Daumont, D., Brion, J., Charbonnier, J., and Malicet, J.: Ozone UV Spectroscopy I: Absorption Cross-Sections
6 at Room Temperature, *J. Atmos. Chem.*, 15, 145-155, 1992.
- 7 De Schouepnikoff, L., Mitev, V., Simeonov, V., Calpini, B., and van den Bergh, H.: Experimental investigation
8 of high-power single-pass Raman shifters in the ultraviolet with Nd:YAG and KrF lasers, *Appl. Opt.*, 36, 5026-
9 5043, 1997.
- 10 De Young, R., Carrion, W., Ganoë, R., Pliutau, D., Gronoff, G., Berkoff, T., and Kuang, S.: Langley mobile
11 ozone lidar: ozone and aerosol atmospheric profiling for air quality research, *Appl. Opt.*, 56, 721-730, 2017.
- 12 Dickensen, G. D., Niu, M. L., Salumbides, E. J., Komasa, J., Eikema, K. S. E., Pachuki, K., and Ubachs, W.:
13 Fundamental Vibration of Molecular Hydrogen, *Phys. Rev. Lett.*, 110, 193601, 5 pp., 2013.
- 14 Draxler, R., and Hess, G.: An overview of the HYSPLIT_4 modelling system for trajectories, dispersion, and
15 deposition, *Aust. Meteorol. Mag.*, 47, 295-308, 1998.
- 16 Dreesen, J., Sullivan, J., and Delgado, R.: Observations and impacts of transported Canadian wildfire smoke on
17 ozone and aerosol air quality in the Maryland region on June 9–12, 2015, *J. Air & Waste Managem. Ass.*, 66,
18 842-862, 2016.
- 19 Duclaux, O., Frejafon, E., Thomasson, A., Yu, J., C., Puel, C., Savoie, F., Ritter, P., Boch, J. P., and Wolf, J. P.:
20 3D-air quality model evaluation using the Lidar technique, *Atmos. Environ.*, 36, 5081-5095, 2002.
- 21 Dufour, A., Amodei, M., Ancellet, G., and Peuch, V.-H.: Observed and modelled “chemical weather” during
22 ESCOMPTE, *Atmos. Res.*, 74, 161-189, 2005.
- 23 Durieux, E., Fiorani, L., Calpini, B., Flamm, M., Jaquet, L., and van den Bergh, H.: Tropospheric Ozone
24 Measurements over the Great Athens Area during the MEDCAPHOT-TRACE Campaign, *Atmos. Environ.*, 32,
25 2141-2150, 1998.
- 26 Eisele, H.: Aufbau und Betrieb eines Dreiwellenlängen-Lidars für Ozonmessungen in der gesamten Troposphäre
27 und Entwicklung eines neuen Auswerteverfahrens zur Aerosol-korrektur, Dissertation, Universität Tübingen
28 (Germany, 1997), published as Schriftenreihe des Fraunhofer-Instituts für Atmosphärische Umweltforschung,
29 Vol. 55 (Verlag Dr. W. Maraun, Frankfurt/Main, Germany, 1998), ISBN 3-932666-08-9, 107 pp., 1997 (in
30 German).
- 31 Eisele, H., and Trickl, T.: Second Generation of the IFU Stationary Tropospheric Ozone Lidar, *Advances in*
32 *Atmospheric Remote Sensing with Lidar, Selected Papers of the 18th International Laser Radar Conference*
33 (Berlin, Germany, 1996), A. Ansmann, R. Neuber, P. Rairoux, U. Wandinger, Eds., Springer (Berlin,
34 Heidelberg, New York), 379-382, 1997.
- 35 Eisele, H., Scheel, H. E., Sladkovic, R., and Trickl, T.: High-Resolution Lidar Measurements of Stratosphere-
36 Troposphere Exchange, *J. Atmos. Sci.*, 56, 319-330, 1999.
- 37 Eisele, H., and Trickl, T.: Improvements of the aerosol algorithm in ozone-lidar data processing by use of
38 evolutionary strategies, *Appl. Opt.*, 44, 2638-2651, 2005.

- 1 EUROTRAC: Transport and Chemical Transformation of Pollutants in the Troposphere, Vol. 1, An Overview of
2 the Work of EUROTRAC, P. Borrell and P. M. Borrell, Eds., Springer (Berlin, Heidelberg, New York), ISBN 3-
3 540-66775-X, 474 pp., 1997.
- 4 Fiorani, L., Calpini, B., Jaquet, L., van den Bergh, H., and Durieux, E.: A Combined Determination of Wind
5 Velocities and Ozone Concentration for a First Measurement of Ozone Fluxes with a DIAL Instrument during
6 the MEDCAPHOT-TRACE Campaign, *Atmos. Environ.*, 32, 2151-2159, 1998.
- 7 Fix, A., Wirth, M., Meister, A., Ehret, G., Pesch, M., and Weidauer, D.: Tunable ultraviolet optical parametric
8 oscillator for differential absorption lidar measurements of tropospheric ozone, *Appl. Phys. B*, 75, 153-163,
9 2002.
- 10 Fix, A., Steinebach, F., Wirth, M., Schäfler, A., and Ehret, G.: Development and application of an airborne
11 differential absorption lidar for the simultaneous measurement of ozone and water vapor profiles in the
12 tropopause region, *Appl. Opt.*, 58, 5892-5900, 2019.
- 13 Freudenthaler, V.: The telecover test: A Quality assurance tool for the optical part of a lidar system, in:
14 Reviewed and Revised Papers Presented at the 24th International Laser Radar Conference, Boulder (Colorado,
15 U.S.A.), Vol. II, M. Hardesty, S. Mayor, Eds., ISBN 978-0-615-21489-4, 145-146, 2008.
- 16 Giehl, H., and Trickl, T.: Testing the IFU High-Spectral-Resolution Lidar at the 2009 Leipzig Field Campaign,
17 in: Proceedings of the 25th International Laser Radar Conference, St.-Petersburg (Russia), July 5 to 9, 2010, G.
18 Matvienko, A. Zemlyanov, Eds., V. E. Zuev Institute of Optics (Tomsk, Russia), 920-923, 2010.
- 19 Galani, E., Balis, D., Zanis, P., Zerefos, C., Papayannis, A., Wernli, H., and Gerasopoulos, E.: Observations of
20 stratosphere-to-troposphere transport events over the eastern Mediterranean using a ground-based lidar system, *J.*
21 *Geophys. Res.*, 108, 8527, doi: 10.1029/2002JD002596, STA 12, 10 pp., 2003.
- 22 Gaudel A., Ancellet G., and Godin-Beekmann S.: Analysis of 20 years of tropospheric ozone vertical profiles by
23 lidar and ECC at Observatoire de Haute Provence (OHP) at 44° N, 6.7° E, *Atmos. Environ.*, 113, 78-89, 2015.
- 24 Gorshelev, V., Serdyuchenko, A., Weber, M., Chebade, W., and Burrows, J. P.: High spectral resolution ozone
25 absorption cross sections – Part 1: Measurements, data analysis and comparison with previous measurement
26 around 293 K, *Atmos. Meas. Tech.*, 7, 609-624, 2014.
- 27 Grabbe, G. C., Bösenberg, J., Dier, H., Görsdorf, U., Matthias, V., Peters, G., Schaberl, T., and Senff, C.:
28 Intercomparison of Ozone Measurements between Lidar and ECC Sondes, *Contr. Atmos. Phys.*, 69, 189-203,
29 1996.
- 30 Granados-Muñoz, M. J., and Leblanc, T.: Tropospheric ozone seasonal and long-term variability as seen by lidar
31 and surface measurements at the JPL-Table Mountain Facility, California, *Atmos. Chem. Phys.*, 16, 9299–9319,
32 2016.
- 33 Granados-Muñoz, M. J., Johnson, M. S., and Leblanc, T.: Influence of the North American monsoon on
34 Southern California tropospheric ozone levels during summer in 2013 and 2014, *Geophys. Res. Lett.*,
35 doi:10.1002/2017GL073375, 6431-6439, 2017.
- 36 Grant, W. B., and Hake, R. D.: Calibrated remote measurements of SO₂ and O₃ using atmospheric backscatter, *J.*
37 *Appl. Phys.*, 46, 3019-3023, 1975.

1 Grant, W. B., Browell, E. V., Butler, C. F., Fenn, M. A., Clayton, M. B., Hannan, J. R., Fuelberg, H. E., Blake,
2 D. R., Blake, N. J., Gregory, G. L., Heikes, B. G., Sachse, G. W., Singh, H. B., Snow, J., and Talbot, R. W.: A
3 case study of transport of tropical marine boundary layer and lower tropospheric air masses to the northern
4 midlatitude upper troposphere, *J. Geophys. Res.*, 105, 3757-3769, 2000.

5 Hearn, A. G.: The Absorption of Ozone in the Ultra-violet and Visible Regions of the Spectrum, *Proc. Phys.*
6 *Soc.*, 78, 932-940, 1961.

7 Hoerling, M. P., Schaack, T. K., and Lenzen, A. J.: Global Objective Tropopause Analysis, *Mon. Weather Rev.*,
8 119, 1816-1831, 1991.

9 Iarlori, M., Madonna, F., Rizi, V., Trickl, T., and Amodeo, A.: Effective resolution concepts for lidar
10 observations, *Atmos. Meas. Tech.*, 8, 5157–5176, 2015.

11 Jäger, H., Carnuth, W., and Georgii, B.: Observations of Saharan dust at a North Alpine mountain station, *J.*
12 *Aerosol Sci.* 19, 1235–1238, 1988.

13 Jeunouvrier, A., Mérienne, M.-F., Coquart, B., Carleer, M., Fally, S., Vandaele, A. C., Hermans, C., and Colin,
14 R.: Fourier Transform Spectroscopy of the O₂ Herzberg Bands – I. Rotational Analysis, *J. Mol. Spectrosc.*, 198,
15 136-162, 1999.

16 Jonson, J. E., Simpson, D., Fagerli, H., and Solberg, S.: Can we explain the trends in European ozone levels?
17 *Atmos. Chem. Phys.*, 6, 51-66, 2006.

18 Kalabokas, P., Papayannis, A., Tsaknakis, G., and Ziomas, I.: A study on the atmospheric concentrations of
19 primary and secondary air pollutants in the Athens basin performed by DOAS and DIAL measuring techniques,
20 *Science of the Total Environment*, 414, 556-563, 2012.

21 Kempfer, U.: Entwicklung und Anwendung eines differentiellen Absorptions-LIDAR-Systems zur Messung der
22 troposphärischen Ozonkonzentration, Dissertation, Ludwig-Maximilians-Universität München (Germany), 151
23 pp., 1992.

24 Kempfer, U., Carnuth, W., Lotz, R., and Trickl, T.: A wide range ultraviolet lidar system for tropospheric ozone
25 measurements: development and application, *Rev. Sci. Instrum.*, 65, 3145-3164, 1994.

26 Klanner, L., Höveler, K., Khordakova, D., Perfahl, M., Rolf, C., Trickl, T., and Vogelmann, H.: Lidar
27 measurements of atmospheric water vapour up to 20 km within one hour, submitted to *Atmos. Meas. Tech.*,
28 2020.

29 Kley, D., Crutzen, P. J., Smit, H. G. J., Vömel, H., Oltmans, S. J., Grassl, H., and Ramanathan, V.: Observations
30 of near-zero ozone concentrations over the convective Pacific: effects of air chemistry, *Science*, 274, 230-233,
31 1996.

32 Kley, D., Beck, J., Grennfelt, P. I., Hov, O., and Penkett, S. A.: Tropospheric Ozone Research (TOR) A Sub-
33 Project of EUROTRAC, *J. Atmos. Chem.*, 28, 1–9, 1997.

34 Kourtidis, K., Zerefos, C., Rapsomanikis, S., Simeonov, V., Balis, D., Perros, P. E., Thompson, A. M., Witte, J.,
35 Calpini, B., Sharobiem, W. M., Papayannis, A., Mihalopoulos, N., and Drakou, R.: Regional levels of ozone in
36 the troposphere over eastern Mediterranean, *J. Geophys. Res.*, 107, 8140, doi: 10.1029/2000JD000140, PAU 7,
37 13 pp., 2002.

1 Kowol-Santen, J., and Ancellet, G.: Mesoscale analysis of transport across the subtropical tropopause, *Geophys.*
2 *Res. Lett.*, 27, 3345-3347, 2000.

3 Kreipl, S.: Messung des Aerosoltransports am Alpennordrand mittels Laserradar (Lidar), Dissertation, Friedrich-
4 Alexander-Universität Erlangen-Nürnberg (Germany), 195 pp.; 2006; in German.

5 Krupenie, P. H.: The Spectrum of Molecular Oxygen, *J. Phys. Chem. Ref. Data*, 1,423-534, 1972.

6 Kuang, S., Burris, J. F., Newchurch, M. J., Johnson, S., and Long, S.: Differential Absorption Lidar to measure
7 subhourly variation of tropospheric ozone profiles, *IEEE Trans. Geosci. Remote Sens.*, 49, 557-571, 2011.

8 Kuang, S., Burris, J. F., Newchurch, M. J., Johnson, S., and Long, S.: Differential Absorption Lidar to Measure
9 Subhourly Variation of Tropospheric Ozone Profiles, *IEEE Trans. Geosci. Remote Sens.*, 49, 557-571, 2011.

10 Kuang, S., Newchurch, M. J., Burris, J., Wang, L., Knupp, K., and Huang, G.: Stratosphere-to-troposphere
11 transport revealed by ground-based lidar and ozonesonde at a midlatitude site, *J. Geophys. Res.*, 117, D18305,
12 doi: 10.1029/2012JD017695, 14 pp., 2012.

13 Kuang, S., Newchurch, M. J., Burris, J. F., and Liu, X.: Ground-based lidar for atmospheric boundary layer
14 ozone measurements, *Appl. Opt.*, 52, 3557-3566, 2013.

15 Kuang, S., Newchurch, M. J., Johnson, M. S., Wang, L., Burris, J. F., Pierce, R. B., Eloranta, E. W., Pollack, I.
16 W., Graus, M., de Gouw, J., Warneke, C., Ryerson, T. B., Markovic, M. Z., Holloway, J. S., Pour-Biazar, A.,
17 Huang, G., Liu, X., and Feng, N.: Summertime tropospheric ozone enhancement associated with a cold front
18 passage due to stratosphere-to-troposphere transport and biomass burning: Simultaneous ground-based lidar and
19 airborne measurements, *J. Geophys. Res.*, 122, doi:10.1002/2016JD026078, 1293–1311, 2017.

20 Lamarque, J.-F., Langford, A. O., and Proffitt, M. H.: Cross-tropopause mixing of ozone through gravity wave
21 breaking: Observation and modelling, *J. Geophys. Res.*, 101, 22969-22976, 1996.

22 Langford, A. O.: Identification and correction of analog-to-digital-converter nonlinearities and their implications
23 for differential absorption lidar measurements, *Appl. Opt.*, 34, 8330-8340, 1995.

24 Langford, A. O., Masters, C. D., Proffitt, M. H., Hsie, E.-Y., and Tuck, A. F.: Ozone measurements in a
25 tropopause fold associated with a cut-off low system, *Geophys. Res. Lett.*, 23, 2501-2504, 1996.

26 Langford, A. O., Aikin, K. C., Eubank, C. S., and Williams, E. J.: Stratospheric contribution to high surface
27 ozone in Colorado during springtime, *Geophys. Res. Lett.*, 36, L12801, doi:10.1029/2009GL038367, 5 pp., 2009

28 Langford, A. O., Brioude, J., Cooper, O. R., Senff, C. J., Alvarez II, R. J., Hardesty, R. M., Johnson, B. J., and
29 Oltmans, S. J.: Stratospheric influence on surface ozone in the Los Angeles area during late spring and early
30 summer of 2010, *J. Geophys. Res.*, 117, D00V06, doi: 10.1029/2011JD016766, 17 pp., 2012.

31 Langford, A. O., Alvarez II, R. J., Brioude, J., Fine, R., Gustin, M. S., Lin, M. Y., Marchbanks, R. D., Pierce, R.
32 B., Sandberg, S. P., Senff, C. J., Weickmann, A. M., and Williams, E. J.: Entrainment of stratospheric air and
33 Asian pollution by the convective boundary layer in the southwestern U.S., *J. Geophys. Res.*, 122,
34 doi:10.1002/2016JD025987, 1312–1337, 2017.

35 Langford, A. O., Alvarez II, R. J., Brioude, Evan, S., Iraci, L. T., Kirgas, G., Kuang, S., Leblanc, T., Newchurch,
36 M. J., Pierce, R. B., Senff, C. J., and Yates, E. L.: Coordinated profiling of stratospheric intrusions and
37 transported pollution by the Tropospheric Ozone Lidar Network (TOLNet) and NASA Alpha Jet experiment

1 (AJAX): Observations and comparison to HYSPLIT, RAQMS, and FLEXPART, *Atmos. Environ.*, 174, 1-14,
2 2018.

3 Lazzarotto, B., Frioud, M., Larchevêque, G., Mitev, V., Quaglia, P., Simeonov, V., Thompson, A., van den
4 Bergh, H., and Calpini, B.: Ozone and water-vapor measurements by Raman lidar in the planetary boundary
5 layer: error sources and field measurements, *Appl. Opt.*, 40, 2985-2997, 2001.

6 Leblanc, T., Sica, R., van Gijssel, A., Godin-Beekmann, S., Haefele, A., Trickl, T., Payen, P., and Gabarrot, F.:
7 Proposed standardized definitions for vertical resolution and uncertainty in the NDACC lidar ozone and
8 temperature algorithms. Part 1: Vertical resolution, *Atmos. Meas. Tech.*, 9, 4029-4049, 2016; 18 pp. of
9 supplementary material

10 Leblanc, T., Brewer, M. A., Wang, P. S., Granados-Muñoz, M. J., Strawbridge, K. B., Travis, M., Firanski, B.,
11 Sullivan, J. T., McGee, T. J., Sunnicht, G. K., Twigg, L. W., Berkoff, T. A., Carrion, W., Gronoff, G., Aknan,
12 A., Chen, G., Alvarez, R. J., Langford, A. O., Senff, C. J., Kirgis, G., Johnson, M. S., Kuang, S., and
13 Newchurch, M. J.: Validation of the TOLNet lidars: the Southern California Ozone Observation Project
14 (SCOOP), *Atmos. Meas. Tech.*, 11, 6137–6162, 2018.

15 Leclair De Bellevue, J., Réchou, A., Baray, J. L., Ancellet, G., and Diab, R. D.: Signatures of stratosphere to
16 troposphere transport near deep convective events in the southern subtropics, *J. Geophys. Res.*, 111, D24107, doi:
17 10.1029/2005JD006947, 14 pp., 2006.

18 Liang, Q., Jaeglé, L., Hudman, R. C., Turquety, S., Jacob, D. J., Avery, M. A., Browell, E. V., Sachse, G. W.,
19 Blake, D. R., Brune, W., Ren, X., Cohen, R. C., Dibb, J. E., Fried, A., Fuelberg, H., Porter, M., Heikes, B. G.,
20 Huey, G., Singh, H. B., and Wennberg, P. O.: Summertime influence of Asian pollution in the free troposphere
21 over North America, *J. Geophys. Res.*, 112, D12S11, doi: 10.1029/2006JD007919, 20 pp., 2007.

22 Machol, J. L., Marchbanks, R. D., Senff, C. J., McCarty, B. J., Eberhard, W. L., Brewer, W. A., Richter, R. A.,
23 Alvarez II, R. J., Law, D. C., Weickmann, A. M., and Sandberg, S. P.: Scanning tropospheric ozone and aerosol
24 lidar with double-gated photomultipliers, *Applied Optics*, 48, 512-524, 2008.

25 Malicet, J., Daumont, D., Charbonnier, J., Parisse, C., Chakir, A., and Brion, J.: Ozone UV Spectroscopy I:
26 Absorption Cross-Sections and Temperature Dependence, *J. Atmos. Chem.*, 21, 263-273, 1995.

27 Marengo, A., Thouret, V., Nédélec, P., Smit, H., Helten, M., Kley, D., Karcher, F., Simon, P., Law, K., Pyle, J.,
28 Poschmann, G., von Wrede, R., Hume, C., and Cook, T.: Measurement of ozone and water vapor by Airbus in-
29 service aircraft: The MOZAIC airborne program, An overview, *J. Geophys. Res.*, 103, 25631-25642, 1998.

30 Matthias, M.: Vertikalmessungen der Aerosolextinktion und des Ozons mit einem UV-Raman-Lidar,
31 Dissertation, Universität Hamburg, published as Examensarbeit Nr. 80, Max-Planck-Institut für Meteorologie
32 (Hamburg, Germany), ISSN 0938-5177, 143 pp., 2000 (in German).

33 McDermid, I. S., Haner, D. A., Kleiman, M. M., Walsh, T. D., and White, M. L.: Differential absorption lidar
34 systems for tropospheric and stratospheric ozone measurements, *Opt. Engin.*, 30, 22-30, 1991.

35 McDermid, I. S., Beyerle, G., Haner, D. A., and Leblanc, T.: Redesign and improved performance of the
36 tropospheric ozone lidar at the Jet Propulsion Laboratory Table Mountain Facility, *Appl. Opt.*, 41, 7550-7555,
37 2002.

1 Milton, M. J. T., Ancellet, G., Apituley, A., Bösenberg, J., Carnuth, W., Castagnoli, F., Trickl, T., Edner, H.,
2 Stefanutti, L., Schaberl, T., Sunesson, A., and Weitkamp, C.: Raman-shifted laser sources suitable for
3 differential-absorption lidar measurements of ozone in the troposphere, *Appl. Phys. B*, 66, 105-113, 1998.

4 Mytilinaios, M., Papayannis, A., and Tsaknakis, G.: Lower-free tropospheric ozone DIAL measurements over
5 Athens, Greece". *EPJ Web of Conferences*, 176, 05025, doi.org/10.1051/epjconf/201817605025, 2018.

6 Nakazato, M., Nagai, T., Sakai, T., and Hirose, Y.: Tropospheric ozone differential-absorption lidar using
7 stimulated Raman scattering in carbon dioxide, *Appl. Opt.*, 46, 2269-2279, 2007.

8 Newchurch, M. J., Kuang, S., Leblanc, T., Alvarez II, R. J., Langford, A. O., Senff, C. J., Burris, J. F., McGee,
9 T. J., Sullivan, J. T., DeYoung, R. J., Al-Saadi, J., Johnson, M., and Pszenny, A.: TOLNet – A Tropospheric
10 Ozone Lidar Profiling Network for Satellite Continuity and Process Studies, *Proc. 27th International Laser Radar
11 Conference*, New York (U.S.A., 2015), *EPJ Web of Conferences*, 119, 20001, 4 pp., 2016.

12 Newell, R. E., Browell, E. V., Davis, D. D., and Liu, S. C.: Western Pacific ozone and potential vorticity:
13 Implications for Asian pollution, *Geophys. Res. Lett.*, 24, 2733-2736, 1997.

14 Ordoñez, C., Brunner, D., Staehelin, J., Hadjinicolaou, P., Pyle, J. A., Jonas, M., Wernli, H., and Prévôt, A. S.
15 H.: Strong influence of lowermost stratospheric ozone on lower tropospheric background ozone changes over
16 Europe, *Geophys. Res. Lett.*, 34, L07805, doi: 10.1029/2006GL029113, 5 pp., 2007.

17 Pan, L. L., Randel, W. J., Gary, B. L., Mahoney, M. J., and Hints, E. J.: Definitions and sharpness of the
18 extratropical tropopause: A trace gas perspective, *J. Geophys. Res.*, 109, D23103, doi: 10.1029/2004JD004982,
19 11 pp., 2004.

20 Papayannis, A., Balis, D., Zanis, P., Galani, E., Wernli, H., Zerefos, C., Stohl, A., Eckhardt, S., and Amiridis, V.:
21 Sampling of an STT event over the Eastern Mediterranean region by lidar and electrochemical sonde, *Ann.
22 Geophys.*, 23, 2039-2050, 2005. Papayannis, A., Amiridis, V., Mona, L., Tsaknakis, G., Balis, D., Bösenberg, J.,
23 Chaikovskiy, A., De Tomasi, F., Grigorov, I., Mattis, I., Mitev, V., Müller, D., Nickovic, S., Pérez, C.,
24 Pietruczuk, A., Pisani, G. L., Ravetta, F., Rizi, V., Sicard, M., Trickl, T., Wiegner, M., Gerding, M., Mamouri,
25 R. E., D'Amico, G., and Pappalardo, G.: Systematic lidar observations of Saharan dust over Europe in the frame
26 of EARLINET (2000-2002), *J. Geophys. Res.*, 113, D10204; doi: 10.1029/2007JD009028, 17 pp., 2008.

27 Papayannis, A., Ancellet, G., Pelon, J., and Mégie, G.: Multiwavelength lidar for ozone measurements in the
28 troposphere and the lower stratosphere, *Appl. Opt.* 29, 467-476, 1990.

29 Pelon, J., and Mégie, G.: Ozone Monitoring in the Troposphere and Lower Stratosphere: Evaluation and
30 Operation of a Ground-Based Lidar Station, *J. Geophys. Res.*, 87, 4947-4955, 1982.

31 Perrone, M. R., and Piccinno, V.: On the benefits of astigmatic focusing configurations in stimulated Raman
32 scattering processes, *Opt. Comm.*, 133; 534-540, 1997.

33 Proffitt, M. H., and Langford, A. O.: Ground-based differential-absorption lidar system for day or night
34 measurements of ozone throughout the free troposphere, *Appl. Opt.*, 36, 2568-2585, 1997.

35 Ravetta, F., Ancellet, G., Kowol-Santen, J., Wilson, R., and Nedeljkovic, D.: Ozone, Temperature, and Wind
36 Field Measurements in a Tropopause Fold: Comparison with a Mesoscale Model Simulation, *Mon. Wea. Rev.*,
37 127, 2641-2653, 1999.

1 Ravetta, F., Ancellet, A., Colette, A., and Schlager, H.: Long-range transport and tropospheric ozone variability
2 in the western Mediterranean region during the Intercontinental Transport of Ozone and Precursors (ITOP-2004)
3 campaign, *J. Geophys. Res.*, 112, D10S46, doi: 10.1029/2006JD007724, 12 pp., 2007.

4 Reichardt, J., Wandinger, U., Servazi, M., and Weitkamp, C.: Combined Raman lidar for aerosol, ozone and
5 moisture measurements, *Opt. Eng.*, 35, 1457-1465, 1996.

6 Roelofs, G. J., Kentarchos, A. S., Trickl, T., Stohl, A., Collins, W. J., Crowther, R. A., Hauglustaine, D.,
7 Klonecki, A., Law, K. S., Lawrence, M. G., von Kuhlmann, R., and van Weele, M.: Intercomparison of
8 tropospheric ozone models: Ozone transport in a complex tropopause folding event, *J. Geophys. Res.*, 108, 8529,
9 10.1029/2003JD003462, *STA* 14, 13 pp., 2003.

10 Scheel, H. E.: Ozone Climatology Studies for the Zugspitze and Neighbouring Sites in the German Alps, pp.
11 134-139 in: *Tropospheric Ozone Research 2, EUROTRAC-2 Subproject Final Report*, A. Lindskog, Co-
12 ordinator, EUROTRAC International Scientific Secretariat (München, Germany, 2003);
13 <http://www.trickl.de/scheel.pdf>.

14 Seibert, P., Feldmann, H., Neininger, B., Bäumle, M., and Trickl, T.: South foehn and ozone in the Eastern
15 Alps – case study and climatological aspect, *Atmos. Environ.*, 34, 1379-1394, 2000.

16 Senff, C. J., Hardesty, R. M., Alvarez II, R. J., and Mayor, S. D.: Airborne lidar characterization of power plant
17 plumes during the 1995 Southern Oxidants Study, *J. Geophys. Res.*, 103, 31173-31189, 1998.

18 Senff, C. J., Alvarez II, R. J., Hardesty, R. M., Banta, R. M., and Langford, A. O.: Airborne lidar measurements
19 of ozone flux downwind of Houston and Dallas, *J. Geophys. Res.*, 115, D20307, doi:10.1029/2009JD013689, 13
20 pp., 2010.

21 Serdyuchenko, A., Gorshchev, V., Weber, M., Chebade, W., and Burrows, J. P.: High spectral resolution ozone
22 absorption cross sections – Part 2: Temperature dependence, *Atmos. Meas. Tech.*, 7, 625–636, 2014, 2014.

23 Simeonov, V., Larcheveque, G., Quaglia, P., van den Bergh, H., and Calpini, B.: Influence of the photomultiplier
24 tube spatial uniformity on lidar signals, *Appl. Opt.*, 38, 5186-5190, 1999.

25 Simeonov, V., Ristori, P., Taslakov, M., Dinev, T., Molina, L. T., Molina, M. J., and van den Bergh, H.: Ozone
26 and aerosol distribution above Mexico City measured with a DIAL/elastic lidar system during the Mexico City
27 Metropolitan Area (MCMA) 2003 field campaign, in: *Lidar Technologies, Techniques, and Measurements for*
28 *Atmospheric Remote Sensing*, U. N. Singh, Ed., *Proc. SPIE*, 5968, 59840O, doi: 10.1117/12.629429, 8 pp.,
29 2005.

30 Stohl, A., and Trickl, T.: A textbook example of long-range transport: Simultaneous observation of ozone
31 maxima of stratospheric and North American origin in the free troposphere over Europe, *J. Geophys. Res.*, 104,
32 30445-30462, 1999.

33 Stohl, A., Spichtinger-Rakowsky, N., Bonasoni, P., Feldmann, H., Memmesheimer, M., Scheel, H. E., Trickl, T.,
34 Hübener, S., Ringer, W., and Mandl, M.: The influence of stratospheric intrusions on alpine ozone
35 concentrations, *Atmos. Environ.*, 34, 1323-1354, 2000.

36 Stohl, A., Bonasoni, P., Cristofanelli, P., Collins, W., Feichter, J., Frank, A., Forster, C., Gerasopoulos, E.,
37 Gäggeler, H., James, P., Kentarchos, T., Kromp-Kolb, H., Krüger, B., Land, C., Meloen, J., Papayannis, A.,
38 Priller, A., Seibert, P., Sprenger, M., Roelofs, G. J., Scheel, H. E., Schnabel, C., Siegmund, P., Tobler, L., Trickl,

1 T., Wernli, H., Wirth, V., Zanis, P., and Zerefos, C.: Stratosphere-troposphere exchange - a review, and what we
2 have learned from STACCATO, *J. Geophys. Res.*, 108, 8516, doi:10.1029/2002JD002490, STA 1, 15 pp., 2003.

3 Strawbridge, K. B., Travis, M. S., Firanski, B. J., Brook, J. R., Staebler, R., and Leblanc, T.: A fully autonomous
4 ozone, aerosol and nighttime water vapour lidar: a synergistic approach to profiling the atmosphere in the
5 Canadian oil sands region, *Atmos. Meas. Tech.*, 11, 6735–6759, 2018.

6 Sullivan, J. T., McGee, T. J., Sumnicht, G. K., Twigg, L. W., and Hoff, R. M.: A mobile differential absorption
7 lidar to measure sub-hourly fluctuations of tropospheric ozone in the Baltimore-Washington, D.C. region,
8 *Atmos. Meas. Tech.*, 7, 3529-3548, 2014.

9 Sullivan, J. T., McGee, T. J., Thompson, A. M., Pierce, R. B., Sumnicht, G. K., Twigg, L. W., Eloranta, E. W.,
10 and Hoff, R. M.: Characterizing the lifetime and occurrence of stratospheric-tropospheric exchange events in the
11 rocky mountain region using high-resolution ozone measurements, *J. Geophys. Res.*, 120, 12410-12424, doi:
12 10.1002/2015JD023877, 2016.

13 Sullivan, J. T., Rabenhorst, S. T., Dreessen, J., McGee, T. J., Delgado, R., Twigg, L., and Sumnicht, G.: Lidar
14 observations revealing transport of O₃ in the presence of a nocturnal low-level jet: Regional implications for
15 “next-day” pollution, *Atmos. Environ.*, 158, 160-171, 2017.

16 Sunesson, J. A., Apituley, A., and Swart, D. P. J.: Differential absorption lidar system for routine monitoring of
17 tropospheric ozone, *Appl. Opt.*, 33, 7045-7058, 1994.

18 Tarasick, D., Galbally, I. E., Cooper, O. R., Schultz, G M., Ancellet, G., Leblanc, T., Wallington, T. J., Ziemke,
19 J., Liu, X., Steinbacher, M., Staehelin, J., Vigouroux, C., Hannigan, J., García, O., Foret, G., Zanis, P.,
20 Weatherhead, E., Petropavlovskikh, I., Worden, H., Osman, M., Liu, J., Chang, K.-L., Gaudel, A., Lin, M.,
21 Granados-Muñoz, M., Thompson, A. M., Oltmans, S. J., Cuesta, J., Dufour, G., Thouret, V., Hassler, B., Trickl,
22 T., and Neu, J. L.: Tropospheric Ozone Assessment Report: Tropospheric ozone from 1877 to 2016, observed
23 levels, trends and uncertainties, *Elem. Sci. Anth.*, 7, Article 39, DOI: <https://doi.org/10.1525/elementa.376>, 72
24 pp. (plus 56 pp. of supplemental material), 2019.

25 TESLAS: Tropospheric Environmental Studies by Laser Sounding (TESLAS), in: Transport and Chemical
26 Transformation of Pollutants in the Troposphere, Vol. 8, Instrument Development for Atmospheric Research and
27 Monitoring, J. Bösenberg, D. Brassington, and P. C. Simon, Eds., Springer (Berlin, Heidelberg, New York),
28 ISBN 3-540-62516-X, 1-203, 1997.

29 Thomasson, A., Geffroy, S., Frejafon, E., Weidauer, D., Fabian, R., Godet, Y., Nominé, M., Ménard, T.,
30 Rairoux, P., Moeller, D., and Wolf, J. P.: LIDAR mapping of ozone-episode dynamics and intercomparison with
31 spot analyzers, *Appl. Phys. B*, 74, 453-459, 2002.

32 Trickl, T.: Lidar Studies of Tropospheric Transport, in: Tropospheric Ozone Research 2, EUROTRAC-2
33 Subproject Final Report, A. Lindskog, Subproject Co-ordinator, EUROTRAC-2 International Scientific
34 Secretariat (München, Germany, 2003), 146-159, 2003; [http:// www.trickl.de/TOR.pdf](http://www.trickl.de/TOR.pdf)

35 Trickl, T.: Upgraded 1.56- μ m lidar at IMK-IFU with 0.28 J/pulse, *Appl. Opt.*, 49, 3732-3740, 2010.

36 Trickl, T.: Tropospheric trace-gas measurements with the differential-absorption lidar technique, in: Recent
37 Advances in Atmospheric Lidars, L. Fiorani, V. Mitev, Eds., INOE Publishing House, Bucharest (Romania),
38 Series on Optoelectronic Materials and Devices, Vol. 7, ISSN 1584-5508, ISSN 978-973-88109-6-9; 87-147,
39 2010; revised version: <http://www.trickl.de/DIAL.pdf>.

- 1 Trickl, T., Vrakking, M. J. J., Cromwell, E. F., Lee, Y. T., and Kung, A. H.: Ultrahigh-resolution (1 + 1)
2 photoionization spectroscopy of Kr I: Hyperfine structures, isotope shifts and lifetimes for the n = 5, 6, 7 4p 5ns
3 Rydberg levels, *Phys. Rev. A*, 39, 2948-2955, 1989.
- 4 Trickl, T., Cooper, O. R., Eisele, H., James, P., Mücke, R., and Stohl, A.: Intercontinental transport and its
5 influence on the ozone concentrations over central Europe: Three case studies, *J. Geophys. Res.*, 108, D12, 8530,
6 10.1029/2002JD002735, *STA* 15, 23 pp., 2003.
- 7 Trickl, T., A. H. Kung, A. H., and Y. T. Lee, Y. T.: Krypton atom and testing the limits of extreme-ultraviolet
8 tunable-laser spectroscopy, *Phys. Rev. A* 75, 022501, 13 pp, 2007.
- 9 Trickl, T., Feldmann, H., Kanter, H.-J., Scheel, H. E., Sprenger, M., Stohl, A., and Wernli, H.: Deep
10 stratospheric intrusions over Central Europe: case studies and climatological aspects, *Atmos. Chem. Phys.*, 10,
11 499-524, 2010.
- 12 Trickl, T., Eisele, H., Bärtsch-Ritter, N., Furger, M., Mücke, R., Sprenger, M., and Stohl, A.: High-ozone layers
13 in the middle and upper troposphere above Central Europe: potential import from the stratosphere along the
14 subtropical jet stream, *Atmos. Chem. Phys.*, 11, 9343-9366; 5-p. Supplement, 2011.
- 15 Trickl, T., Vogelmann, H., Giehl, H., Scheel, H. E., Sprenger, M., and Stohl, A.: How stratospheric are deep
16 stratospheric intrusions? *Atmos. Chem. Phys.*, 14, 9941-9961, 2014.
- 17 Trickl, T., Vogelmann, H., Flentje, H., and Ries, L.: Stratospheric ozone in boreal fire plumes – the 2013 smoke
18 season over Central Europe, *Atmos. Chem. Phys.*, 15, 9631-9649, 2015.
- 19 Trickl, T., Vogelmann, H., Fix, A., Schäfler, A., Wirth, M., Calpini, B., Levrat, G., Romanens, G., Apituley, A.,
20 Wilson, K. M., Begbie, R., Reichardt, J., Vömel, H. and Sprenger, M.: How stratospheric are deep stratospheric
21 intrusions into the troposphere? LUAMI 2008, *Atmos. Chem. Phys.*, 16, 8791-8815, 2016.
- 22 Trickl, T., Vogelmann, H., Ries, L., and Sprenger, M.: Very high stratospheric influence observed in the free
23 troposphere over the Northern Alps – just a local phenomenon? *Atmos. Chem. Phys.*, 20, 243-266, 2020.
- 24 Uchino, O., Tokunaga, M., Maeda, M., and Miyazoe, Y.: Differential-absorption-lidar measurements of
25 tropospheric ozone with excimer-Raman hybrid laser, *Opt. Lett.*, 8, 347-349, 1983.
- 26 Uchino, O., Sakai, T., Nagai, T., Morino, I., Maki, T., Deushi, M., Shibata, K., Kajino, M., Kawasaki, T., Akaho,
27 T., Takubo, S., Okumura, H., Arai, K., Nakazato, M., Matsunaga, T., Yokota, T., Kawakami, S., Kita, K., and
28 Sasano, Y.: DIAL measurement of lower tropospheric ozone over Saga (33.24° N, 130.29° E), Japan, and
29 comparison with a chemistry-climate model, *Atmos. Meas. Tech.*, 7, 1385-1394, 2014.
- 30 U.S. Standard Atmosphere 1976, National Oceanic and Atmospheric Organization (NOAA), National
31 Aeronautics and Space Administration, United States Air Force, NOAA-S/T 76-1562, U.S. Printing Office
32 (Washington, D.C.), 227 pp., 1976.
- 33 Uthe, E. E., and Livingston, J. M.: Airborne Lidar Mapping of Ozone Concentrations During the Lake Michigan
34 Ozone Study, *J. Air Waste Manage. Assoc.*, 42, 1313-1318, 1992.
- 35 Valente, R. J., Imhoff, R. E., Tanner, R. L., Meagher, J. F., Daum, P. H., Hardesty, R. M., Banta, R. M., Alvarez,
36 R. J., McNider, R. T., and Gillani, N. V.: Ozone production during an urban air stagnation episode over
37 Nashville, Tennessee, *J. Geophys Res.*, 103, 22555-22568, 1998.

1 Vautard, R., Szopa, S., Beekmann, M., Menut, L., Hauglustaine, D. A., Rouil, L., and Roemer, M.: Are decadal
2 anthropogenic emission reductions in Europe consistent with surface ozone observations? *Geophys. Res. Lett.*,
3 33, L13810, doi:10.1029/2006GL026080, 4 pp., 2006.

4 VDI guide line 4210, Remote Sensing, Atmospheric Measurements with LIDAR, Measuring gaseous air
5 pollution with the DAS LIDAR (Verein Deutscher Ingenieure, Düsseldorf, Germany), 47 pp., 1999.

6 Veselovskii, I., and Barchunov, B.: Excimer-laser-based lidar for tropospheric ozone monitoring, *Appl. Phys. B*,
7 68, 1131-1137, 1999.

8 Viallon, J., Lee, S., Moussay, P., Tworek, K., Peterson, M., and Wielgosz, R. I.: Accurate measurements of
9 ozone absorption cross-sections in the Hartley band, *Atmos. Meas. Tech.*, 8, 1245-1257, 2015.

10 Völger, P., Bösenberg, J., and Schult, I.: Scattering Properties of Selected Model Aerosols Calculated at UV-
11 Wavelengths: Implications for DIAL Measurements of Tropospheric Ozone, *Beitr. Phys. Atmosph.*, 69, 177-
12 187, 1996.

13 Vogelmann, H. and Trickl, T.: Wide-Range Sounding of Free-Tropospheric Water Vapor with a Differential-
14 Absorption Lidar (DIAL) at a High-Altitude Station, *Appl. Opt.*, 47, 2116-2132, 2008.

15 VOTALP II: Vertical Ozone Transport in the Alps II, Final Report for the European Union, Contract Nr.: ENV4
16 CT970413, Reporting Period 1/3/1998-29/2/2000, H. Kromp-Kolb, Co-ordinator, Universität für Bodenkultur
17 Wien (Austria), Institut für Meteorologie und Physik, 96 pp., 2000.

18 Wallinder, E., Edner, H., Ragnarson, P., and Svanberg, S.: Vertically Sounding Ozone Lidar System based on a
19 KrF Excimer Laser, *Physica Scripta*, 55, 714-718, 1997.

20 Wang, L., Newchurch, M. J., Alvarez II, R. J., Berkoff, T. A., Brown, S. S., Carrion, W., De Young, R. J.,
21 Johnson, B. J., Ganoë, R., Gronoff, G., Kirgis, G., Kuang, S., Langford, A. O., Leblanc, T., McDuffie, E. E.,
22 McGee, T. J., Pliutau, D., Senff, C. J., Sullivan, J. T., Sumnicht, G., Twigg, L. W., and Weinheimer, A. J.:
23 Quantifying TOLNet ozone lidar accuracy during the 2014 DISCOVER-AQ and FRAPPÉ campaigns, *Atmos.*
24 *Meas. Tech.*, 10, 3865–3876, 2017.

25 Weitkamp, C., Baumbach, G., Becker, K.-H., Braun-Schoen, S., Burger, H., Dinev, S., Fabian, R., Frey, S.,
26 Fritzsche, F., Glaser, K., Glauer, J., Herb, F., Immler, F., Junkermann, W., Kanter, H. J., Lindemann, C.,
27 Loescher, A., Mohnen, V. A., Möller, D., Neidhart, B., Olariu, R., Reimer, E., Schmidt, V., Schubert, G.,
28 Spittler, M., Vogt, U., Weidauer, D., Windholz, L., and Wöste, L.: Wie richtig sind Lidarmessungen der
29 Ozonverteilung?, *Gefahrstoffe – Reinhaltung der Luft*, 60, 279-284, 2000; in German

30 Wotava, G., and Kromp-Kolb, H.: The research project VOTALP – general objectives and main results, *Atmos.*
31 *Environ.*, 34, 1319-1322, 2000.

32 Yates, E. L., Johnson, M. S., Iraci, L. T., Ryoo, J.-M., Pierce, R. B., Cullis, P. D., Gore, W., Ives, M. A.,
33 Johnson, B. J., Leblanc, T., Marrero, J. E., Sterling, C. W., and Tanaka, T.: An Assessment of Ground Level and
34 Free Tropospheric Ozone Over California and Nevada, *J. Geophys. Res.*, 122, 10089-10102,
35 <https://doi.org/10.1002/2016JD026266>, 2017.

36 Zanis, P., Trickl, T., Stohl, A., Wernli, H., Cooper, O., Zerefos, C., Gaeggeler, H., Priller, A., Schnabel, C.,
37 Scheel, H. E., Kanter, H. J., Tobler, L., Kubik, P. W., Cristofanelli, P., Forster, C., James, P., Gerasopoulos, E.,
38 Delcloo, A., Papayannis, A., and Claude, H.: Forecast, observation and modelling of a deep stratospheric
39 intrusion event over Europe, *Atmos. Chem. Phys.*, 3, 763-777, 2003.

1 Zhao, Y., Howell, J. N., and Hardesty, R. M.: Transportable Lidar for the Measurement of Ozone Concentration
2 and Flux Profiles in the Lower Troposphere, in: Proceedings of the 16th International Laser Radar Conference,
3 Cambridge (Massachusetts, U.S.A, 1992), 185-187, 1992.

4 Zhao, Y., Marchbanks, R. D., Senff, C. J., and Johnson, H. D.: Lidar Profiling of Ozone and Aerosol in the
5 SCOS97-NARSTO Experiment, in: Proceedings of the Ninetenth International Laser Radar Conference,
6 Annapolis (Maryland, U.S.A., 1998), U. N. Singh, S. Ismail, and G. K. Schwemmer, Eds., NASA Langley
7 Research Center, NASA/CP-1998-207671/PT1, 375-378, 1998.

8

1 **Table 1. Transmitter Details**

2 The numbers are given for normal operating conditions

3		Stationary system	Mobile system
4	Laser source	KrF laser	frequency-quadrupled Nd:YAG Laser
5	Wavelength	245.50 nm	266.13 nm
6	Pulse energy	400 mJ	70 mJ
7	Pulse repetition rate	99 Hz	30 Hz
8	Operating wavelengths [nm]	277.124 ^a , 291.838 ^b , 313.188 ^a	266.12, 289.10 ^b , 299.21 ^a
9	Emission	simultaneous	289 nm and 299 nm sequential,
10			266 nm for each pulse
11	Beam expansion	5:1	6:1
12	Beam divergence	< 0.75 mrad	< 0.5 mrad

13

14 (a) Q₁ line of first Stokes shift in H₂ (Bragg et al., 1982; Dickensen et al., 2013): 4155.2521 cm⁻¹

15 (b) Q₂ second Stokes shift in D₂ (Jennings et al., 1986): 2987.289 cm⁻¹

16

1 **Table 2. Receiver Details**

2 Latest version only

3	Stationary system	Mobile system
4 Primary mirrors	0.13 m diameter, $f = 0.72$ m	0.36 m diameter, $f = 1.56$ m
5	0.50 m diameter, $f = 2.0$ m	
6 Wavelength separation	two 1.1-m grating	sequential detection of 289 nm,
7	Spectrographs	299 nm, 266 nm optically separated
8 PMTs	Hamamatsu 7400,	Hamamatsu 5600
9	modified by RSV	
10 Pre-amplifiers	gain 1–10, bandwidth 4 MHz	
11	(1996–2011)	
12 Transient digitizers	6 units, 12 bit, 20 MHz	4 units, 12 bit, 20 MHz
13	ground-free input stages	
14 Photon counting	10 GHz time bins	
15 Measurement time	41 s	10 min
16		

1 **Table 3. Measurement periods of the stationary DIAL**

2 **Projects:** TOR (EUROTRAC subproject Tropospheric Ozone Research ^a), VOTALP (Vertical Ozone Transport
 3 in the Alps^b), STACCATO (Influence of Stratosphere-Troposphere Exchange in a Changing Climate on
 4 Atmospheric Transport and Oxidation Capacity^c), ATMOFAST (German abbreviation of “Atmospheric Long-
 5 range Transport and its Impact on the Trace-gas Concentrations in the Free Troposphere over Central Europe” ^d);
 6 for references see text.

7 Period	Measurements	Comments
8 Jan.-Dec. 1991	580 measurements (just about 60	within TOR
9	re-evaluated)	
10 1993	a few measurements	within TOR
11 Jan. 1996-Feb. 1998	1122 evaluated measurements	within VOTALP 1+2
12 May 1999	86 evaluated measurements	within VOTALP 2
13 Aug. 2000-Aug. 2001	520 evaluated measurements	within STACCATO
14 July 2003	37 evaluated measurements	within ATMOFAST
15 2007-2018	2959 evaluated measurements	routine measurements; gaps due to repairs
16		
17 (a) Kley et al., 1997		
18 (b) Wotava and Kromp-Kolb, 2000; VOTALP II, 2000		
19 (c) Stohl et al., 2003		
20 (d) ATMOFAST, 2005		
21		

1 **Table 4. Uncertainties of the stationary ozone lidar**

2 Altitudes: above sea level (a.s.l.); E ... EMI PMTs, H ... Hamamatsu PMTs

3	Period	1-2.3 km	2.3-5 km.	5-8 km	8 km-tropopause	Electronics
4	1991-1993	5 ppb	3-5 ppb	5-20 ppb	not reached	8 bit DSP, E
5	1996-4/1996	5 ppb	2-4 ppb	4-8 ppb	up to 10 ppb (winter)	12 bit DSP, E
6					up to 20 ppb (summer)	
7	5/1996-4/1997	5 ppb	2-4 ppb	4-8 ppb	unknown ^{*)}	12 bit DSP, H
8	5/1997-2003	5 ppb	2-4 ppb	4-8 ppb	best: 7 ppb; up to 10 ppb (winter)	12 bit DSP, H,
9					best: 7-10 ppb; up to 20 ppb (summer)	1 GHz Optec
10	2007-2011	5 ppb	2.5-4 ppb	3-7 ppb	best: 7 ppb; up to 10 ppb (winter)	12 bit Licel, H
11					best: 7-10 ppb; up to 20 ppb (summer)	
12	2012-2019	2-4 ppb	1.5-4 ppb	3-7 ppb	best: 5 ppb; up to 8 ppb (winter)	12 bit Licel, H
13					best: 5-8 ppb; up to 15 ppb (summer)	(ground-free)

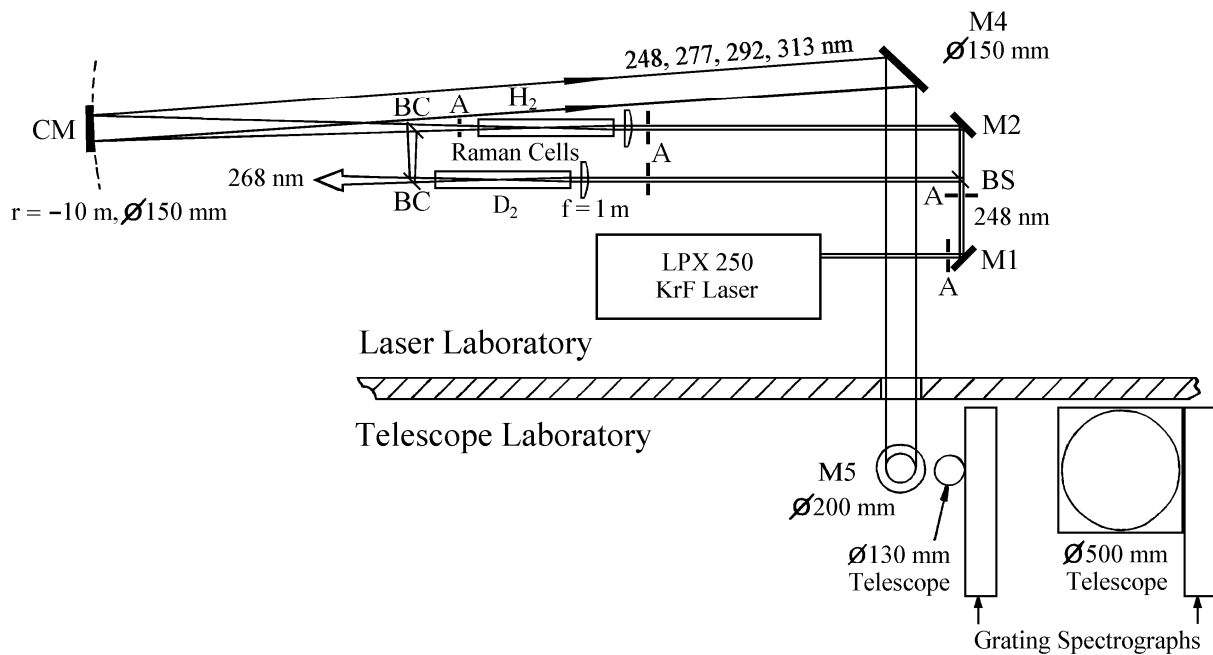
14 ^{*)} Sometimes artefacts in upper troposphere due to preamplifier ringing, corrected for important examples

15

1 **Figures:**

2

3



4 **Fig. 1.** Overview of the IFU stationary ozone DIAL system; the system covers two separate laboratories for the
 5 laser and the telescopes, respectively. Abbreviations:

6 M1, M2 ... dielectric high-reflecting mirrors for 248 nm

7 SM ... spherical mirror ("M3"), high reflecting for 248 to 313 nm, $f = 5$ m

8 M4, M5 ... dielectric mirrors, high reflecting for 248 to 313 nm

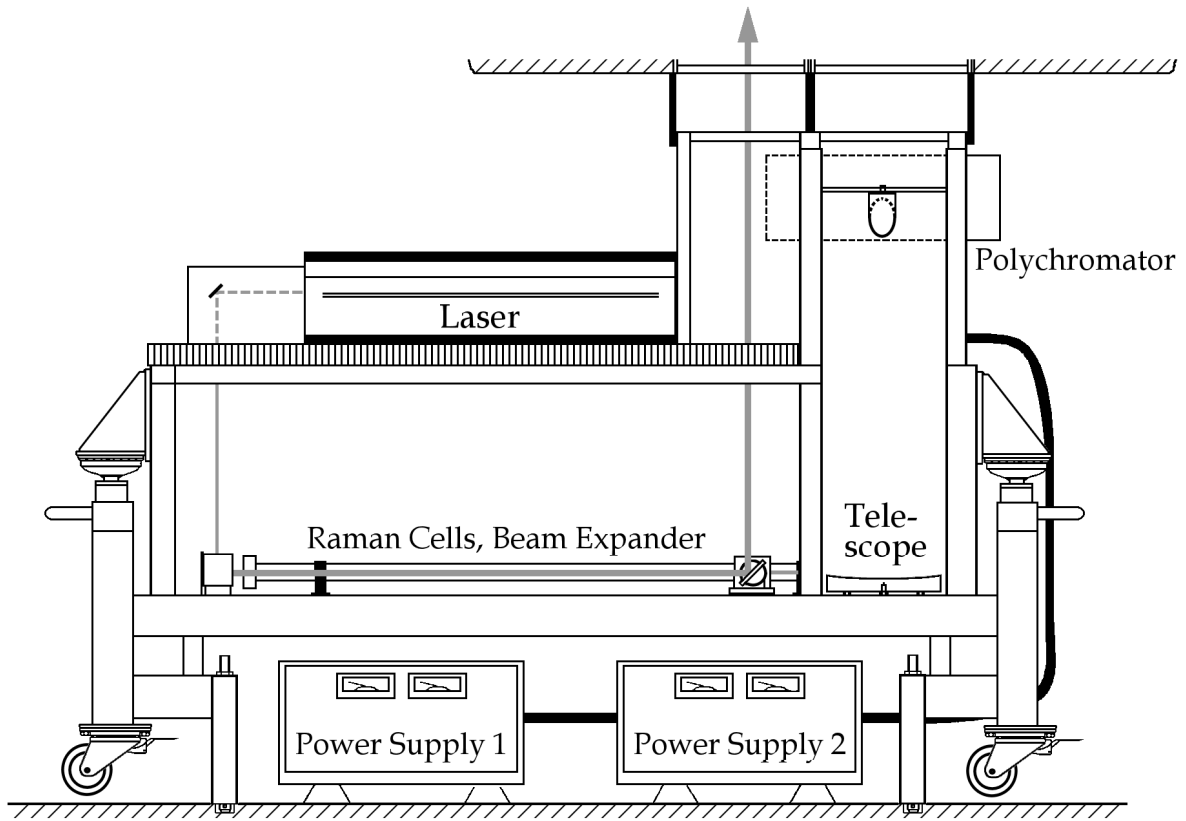
9 BS ... 50-% beam splitter

10 BC ... wavelength-selective beam combiner, reflecting 99 % at 292 nm for an incidence angle of 45° and
 11 transmitting all the other lidar wavelengths with losses of not exceeding 12 %.

12 A ... rectangular sand-blasted aluminium apertures for blocking divergent parts of the amplifier emission that
 13 would otherwise hit and evaporate the black surfaces of the optics holders, leading to more rapid ageing of the
 14 optics.

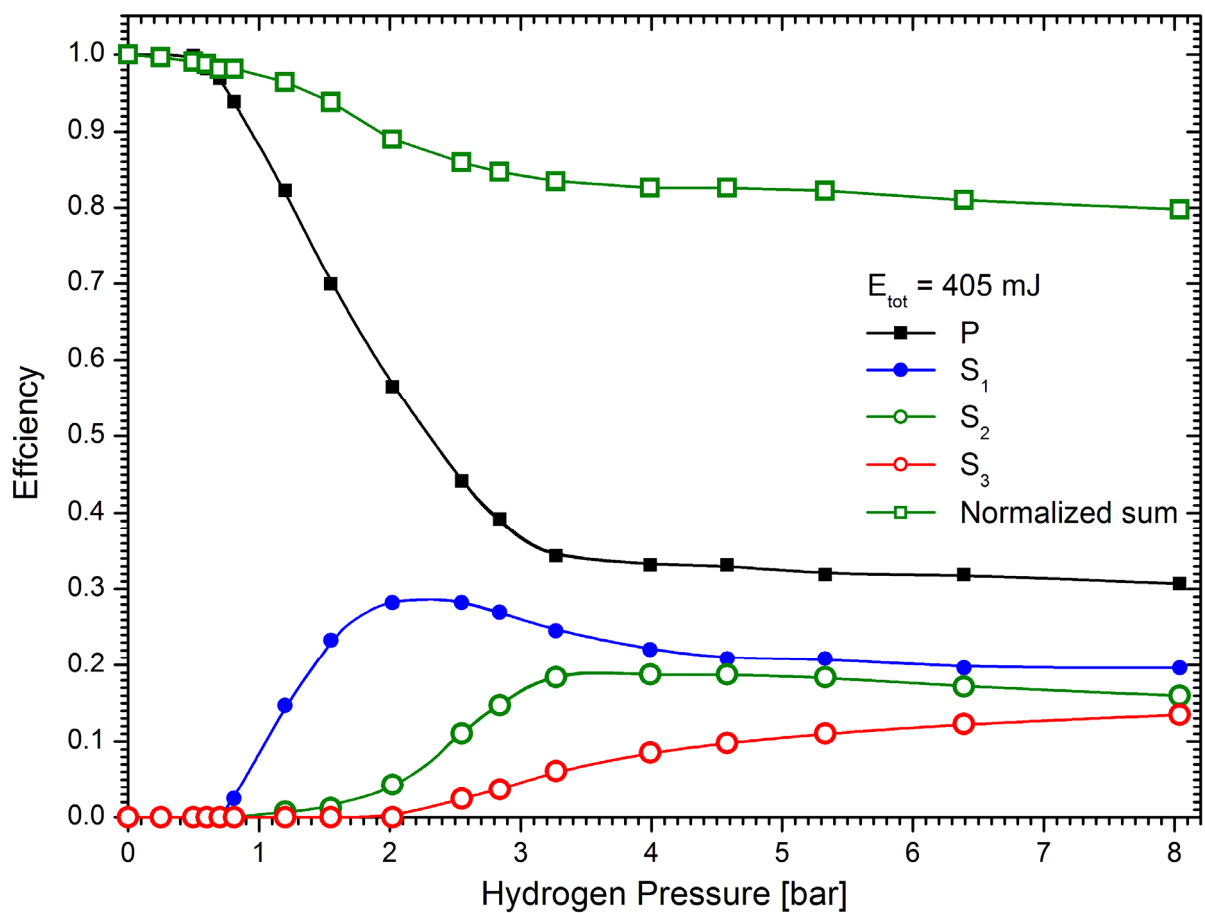
15

1



2 **Fig. 2.** Overview of the mobile ozone DIAL: the laser and the Raman-shifting components were mounted on
3 optical tables at two different levels of a shock-isolated frame. The Newtonian telescope was located in a
4 separate tower, the secondary mirror directing the beam into a polychromator perpendicularly to the plane
5 formed by the telescope and the outgoing laser beam. The covers of the Raman compartment (jalousies on both
6 sides) and the telescope (door) were removed in this simple view. The laser power supply was delivered in two
7 units custom-made to fit under the lower laser table. The entire frame was rolled into the the lorry through the
8 rear doors.
9

1

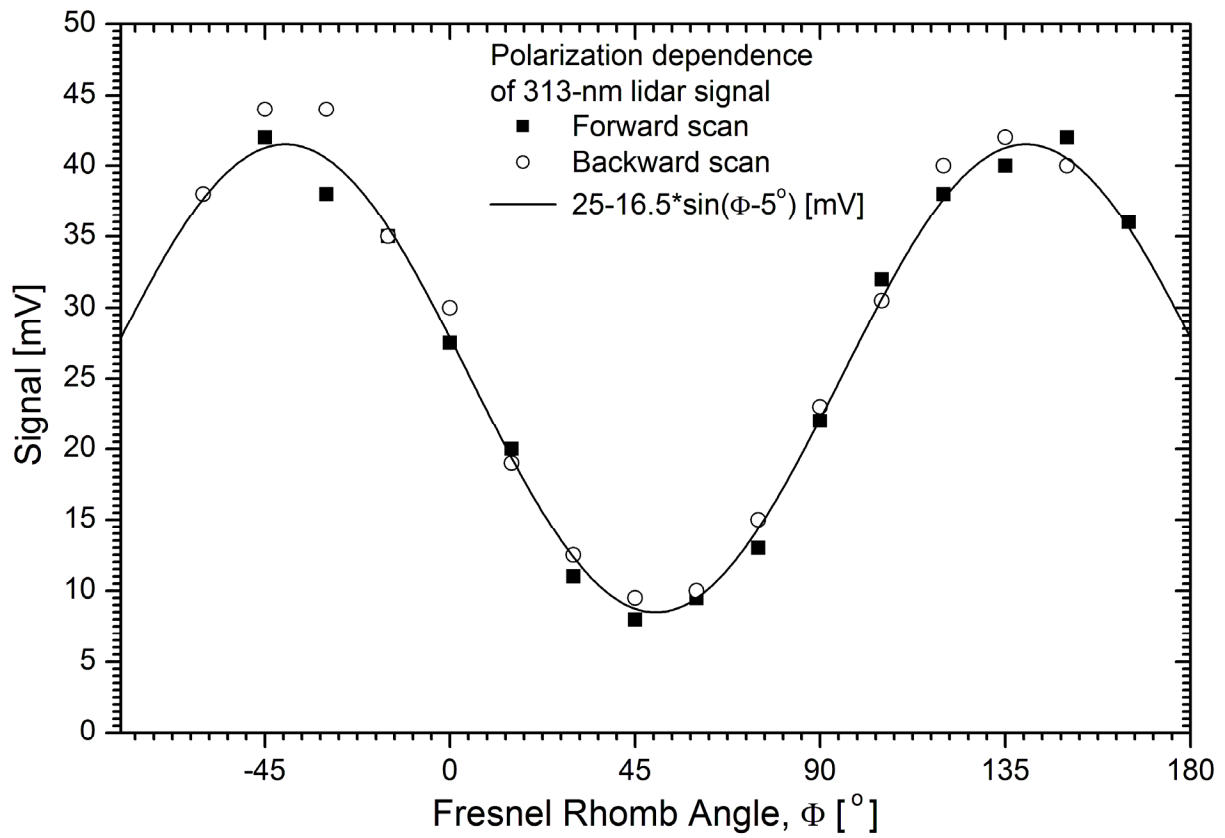


2 **Fig. 3.** Raman conversion efficiency ($f = 1.0$ m) as a function of pressure for shifting the 248.5-nm radiation in
 3 hydrogen; the top curve (dark green) represents the sum of the residual pump energy and the first three Stokes
 4 emissions, normalized to the pump energy at zero pressure. The less important higher-Stokes emissions were not
 5 measured here, but may contribute above 4 bar which would shift the sum to higher values.

6

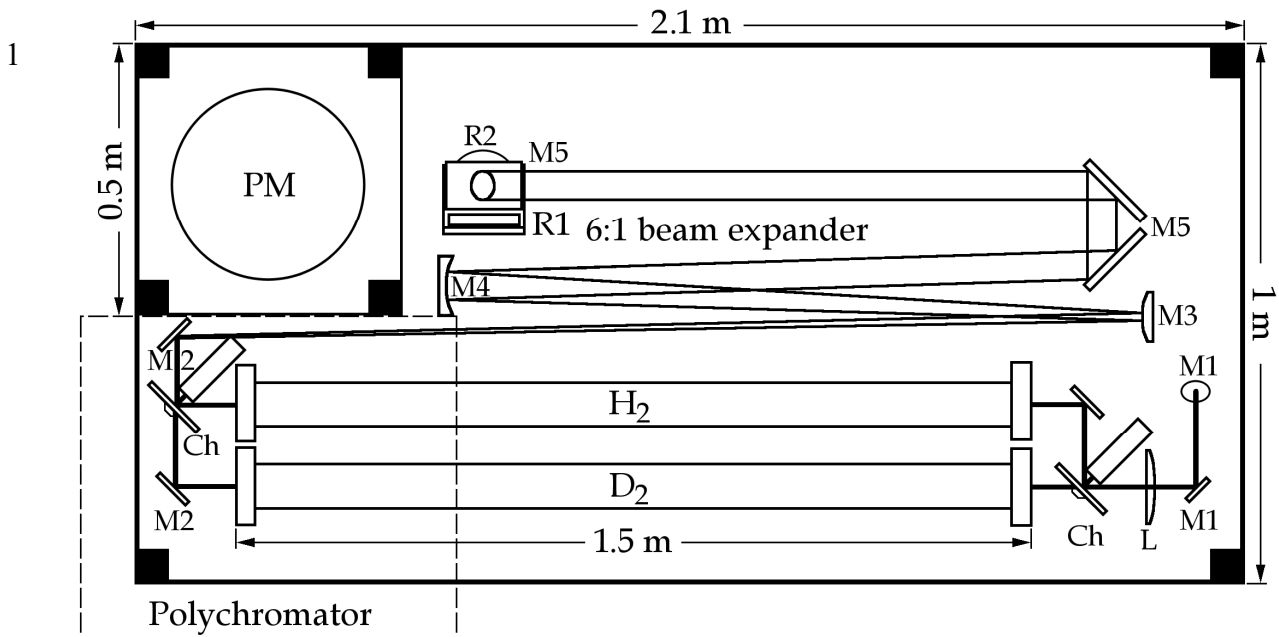
7

1



2 **Fig. 4.** 313-nm backscatter signal as a function of the angle of the Fresnel Rhomb (i.e., half the polarization
3 angle): The strongest signal is achieved with the polarization of the radiation emitted into the atmosphere
4 perpendicular to the grooves of the grating.

5



2 **Fig. 5.** Lower compartment of the transmitter section of the mobile DIAL; the 266-nm beam enters vertically
 3 from the top compartment and hits the first of the two M1 mirrors. The polychromator is located above the two
 4 compartments as indicated by the broken line.

5 Abbreviations:

6 M1 ... high-reflecting mirror for 266 nm

7 M2 ... high-reflecting mirror for at least 266 – 300 nm

8 Ch rotating beam splitter (“chopper”)

9 L $f = 1.00$ m, AR coated

10 M3 ... curved mirror, $f = -0.20$ m, HR coated for at least 266 – 300 nm

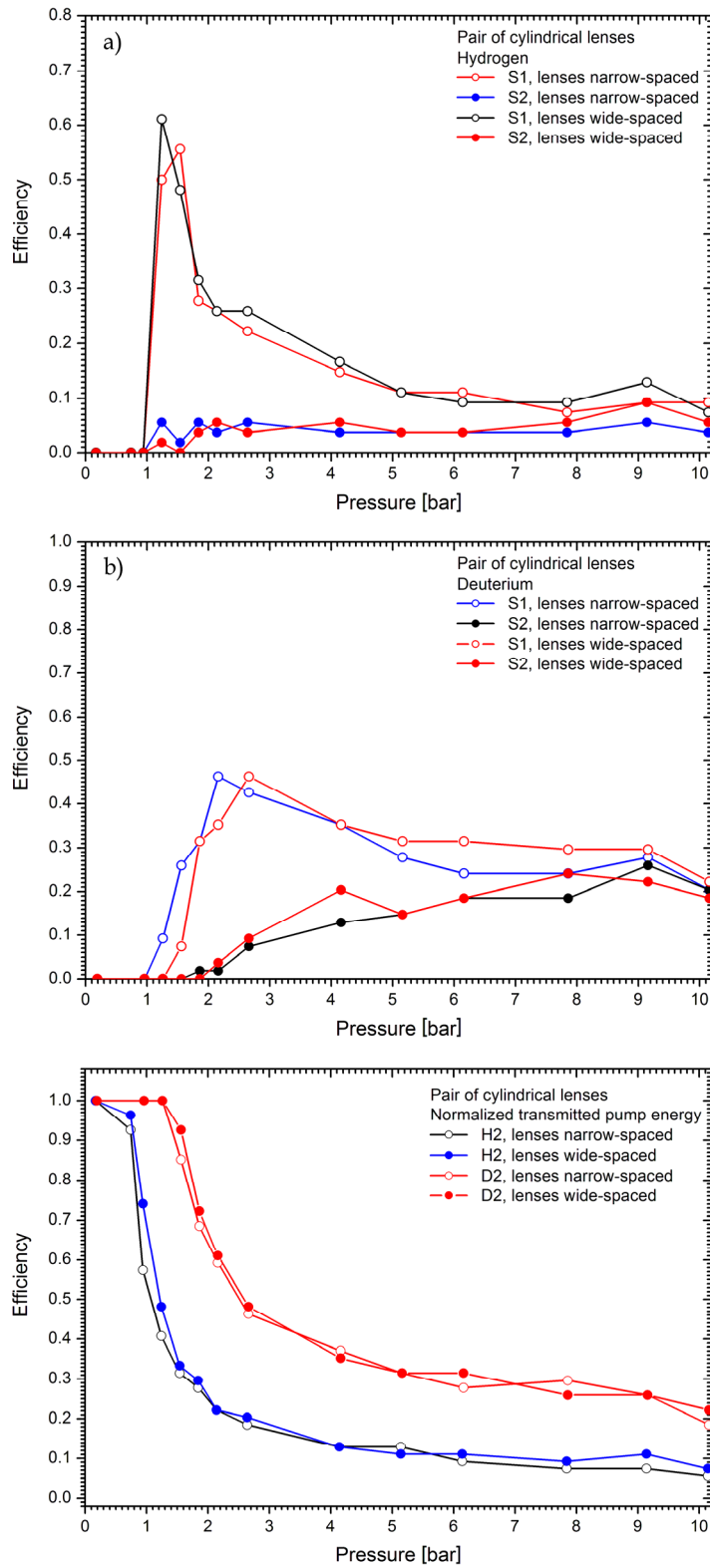
11 M4 ... curved mirror, $f = -0.20$ m, coated for at least 266 – 300 nm

12 M5 ... rectangular mirrors, high-reflecting mirror for at least 266 – 300 nm

13 R1, R2 ... motorized rotation stages, mounted vertically and horizontally, respectively)

14

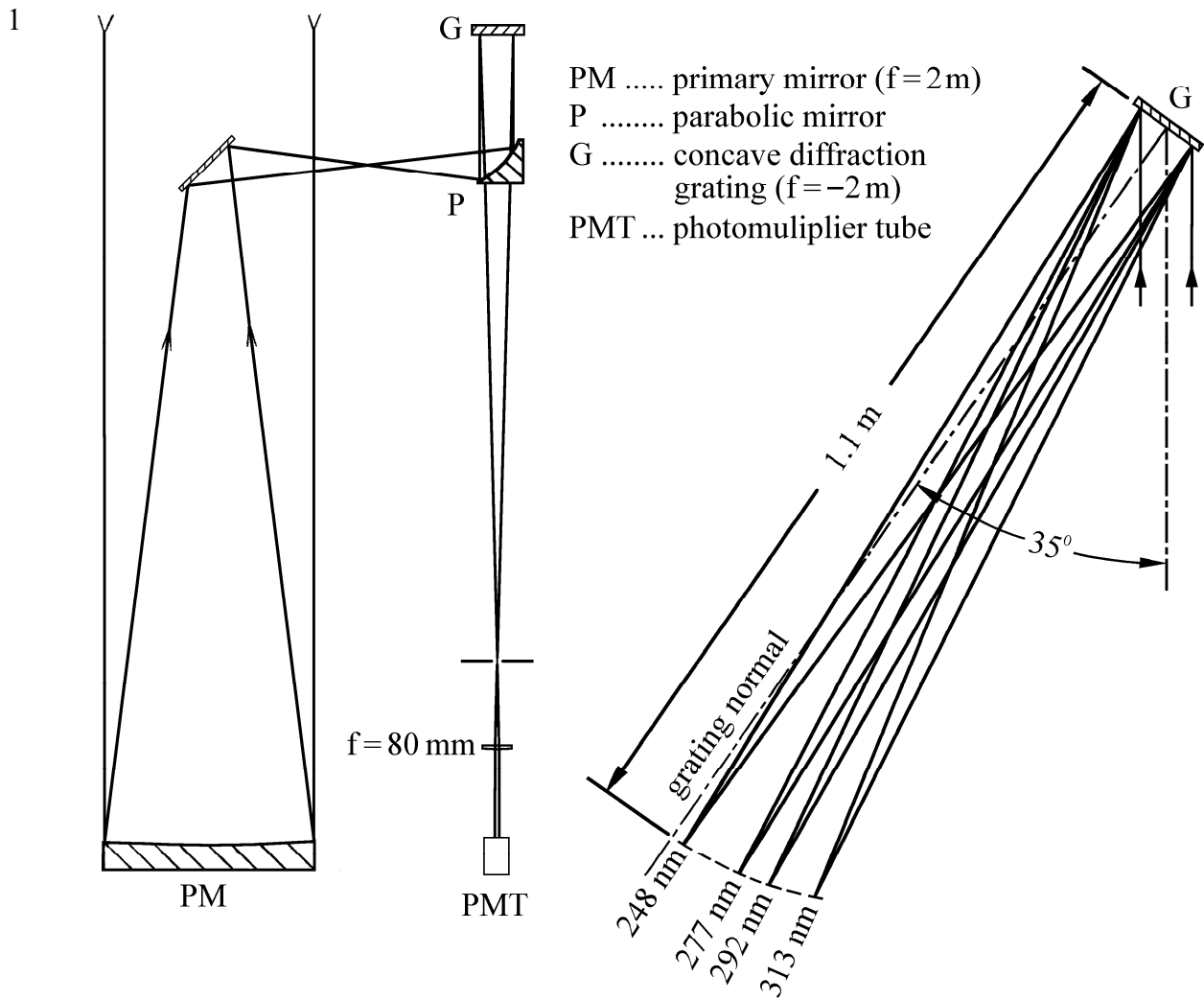
1



2 **Fig. 6.** Raman conversion efficiencies and pump-beam depletion for a pair of crossed $f = **$ m cylindrical lenses:
 3 (a) S1 and S2 in hydrogen (b) S1 and S2 in deuterium (c) normalized transmitted pump energy in both H₂ and
 4 D₂.

5

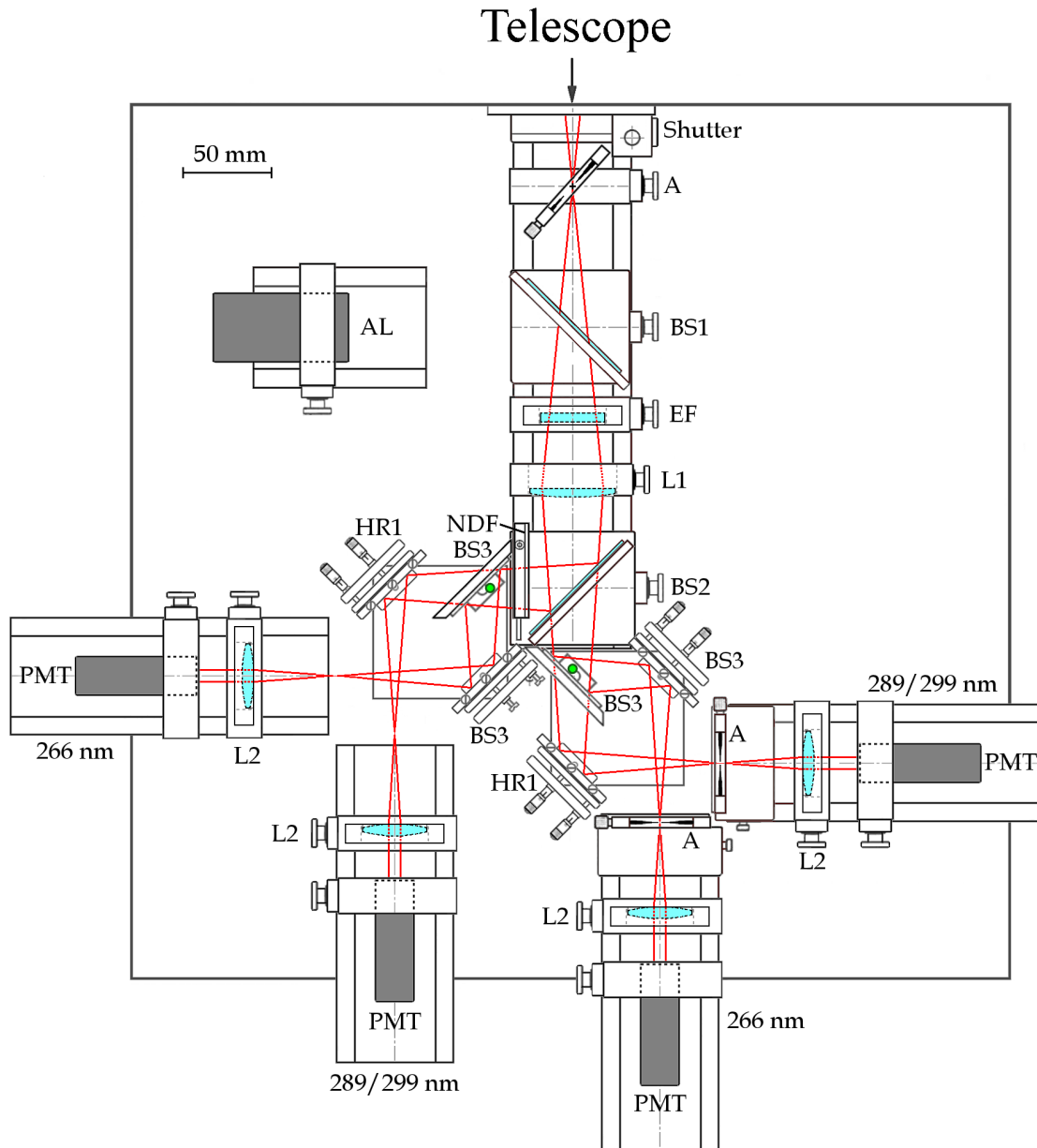
6



2 **Fig. 7.** Layout of the two grating spectrographs; $\alpha = 35^\circ$ is the Wadsworth angle chosen, corresponding to a
3 wavelength of 240.0 nm. The choice of angle was limited by the space available in the housing of the
4 spectrograph, also considering the big PMTs initially used.

5

1



2 **Fig. 8.** Polychromator of the mobile ozone DIAL: The opto-mechanical components were mounted on a rail
 3 system attached to a black optical table with a 25 mm × 25 mm hole pattern (M6 threads, not shown). The two
 4 green dots mark the intermediate image planes of the primary mirror of the telescope. (the secondary image
 5 planes coincide with the PMT cathodes). Abbreviations:

6 A ... rectangular aperture with four adjustable black blades

7 BS1 ... beam splitter for reflecting 532 nm or 1064 nm out of the received radiation for aerosol measurements
 8 (not implemented)

9 BS2 ... 1:100 beam splitter for near-field – far-field separation

10 BS3 ... dichroic beam splitter with $T < 4\%$ for 289 and 299 nm

11 HR1 ... high-reflecting mirror (45°)

12 EF ... Dielectric edge filter, blocking the radiation above 299 nm

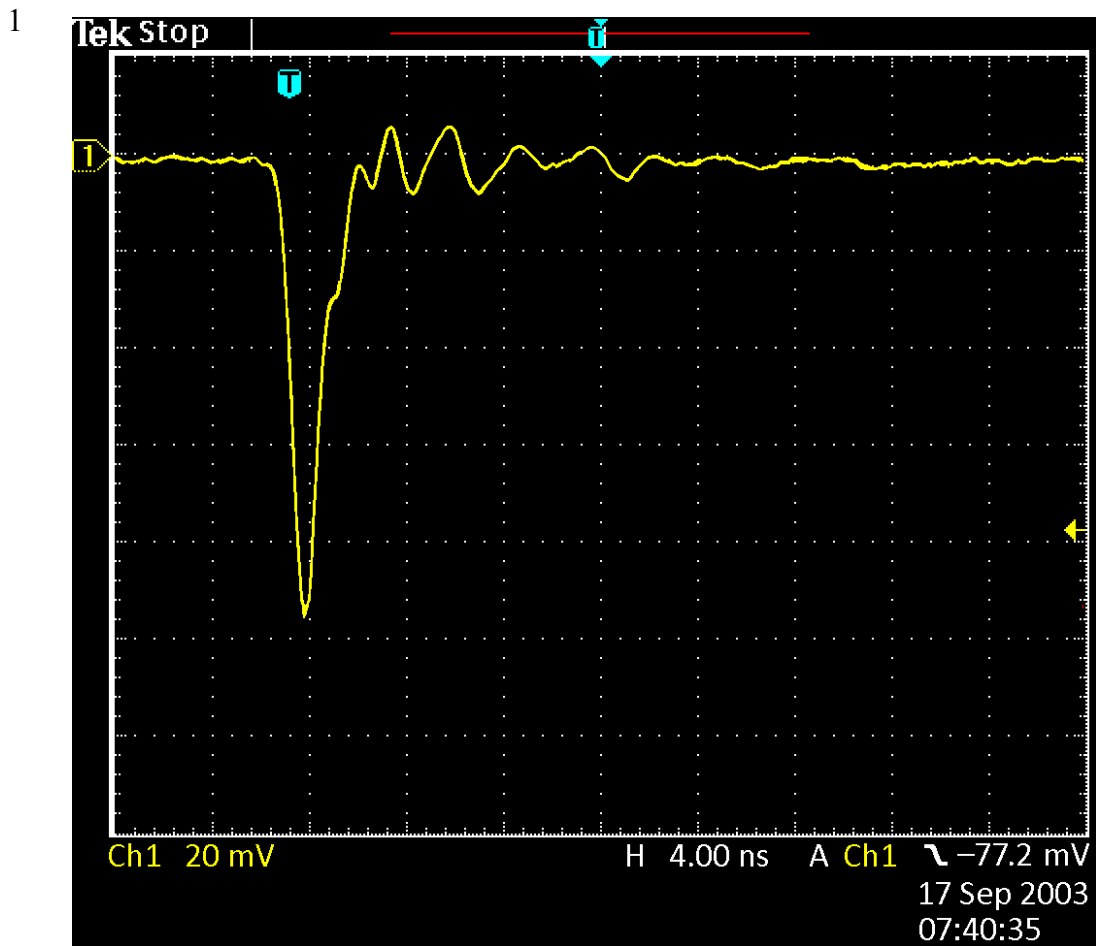
13 NDF ... $T = 10\%$ neutral density filter

14 L1 ... $f = 100$ mm lenses

15 L2 ... $f = 50$ mm lenses

16 AL ... alignment laser

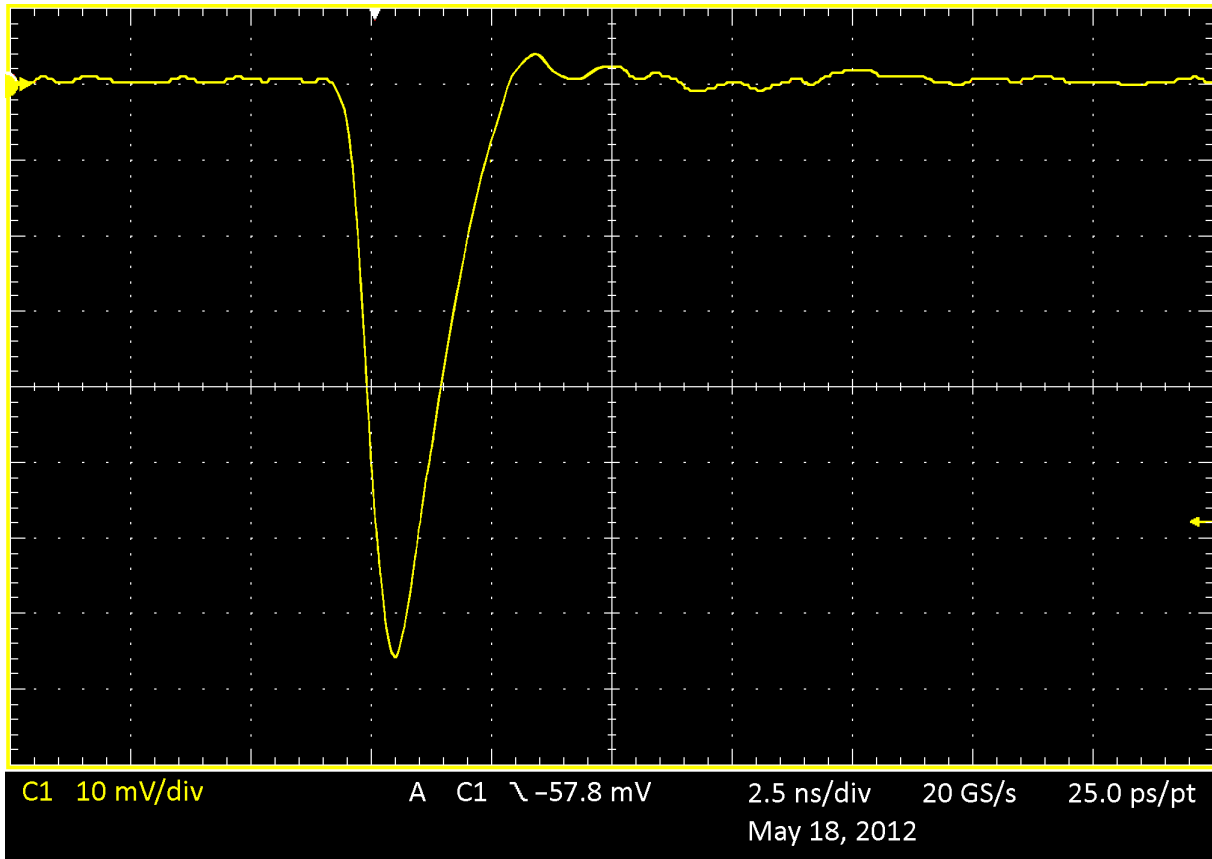
17



2 **Fig. 9.** Top panel: Single-photon pulse from a Hamamatsu 5600 or 7400 PMT, measured with a 500-MHz digital
3 oscilloscope (Tektronix, TDS 3045 C)

4

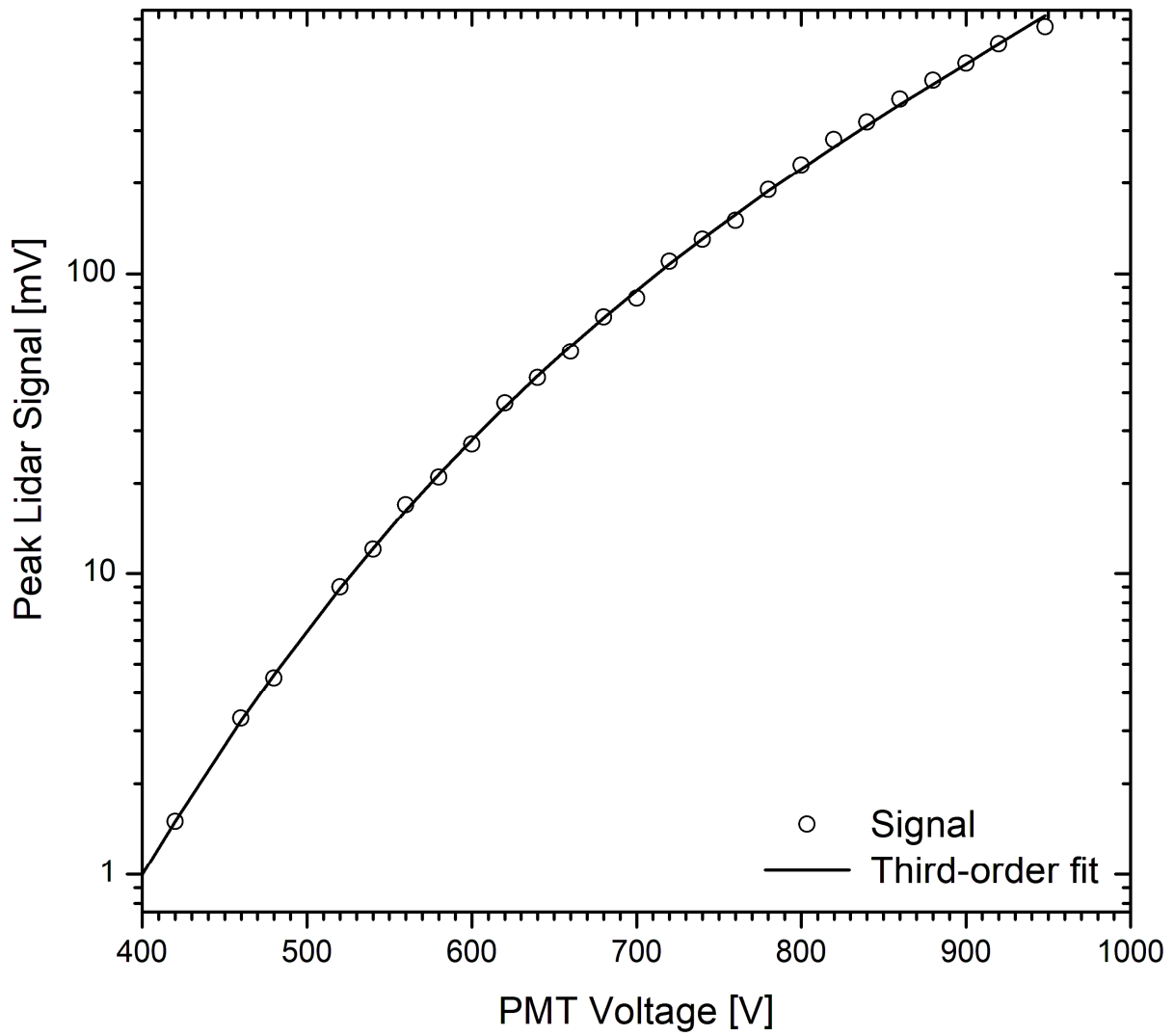
1



2 **Fig. 9.** Bottom panel: Single-photon pulse from a Hamamatsu R7400P-03 PMT with the most recent version of
3 the Romanski (RSV) socket, measured with a 1-GHz digital oscilloscope (Tektronix, DPO 7104)

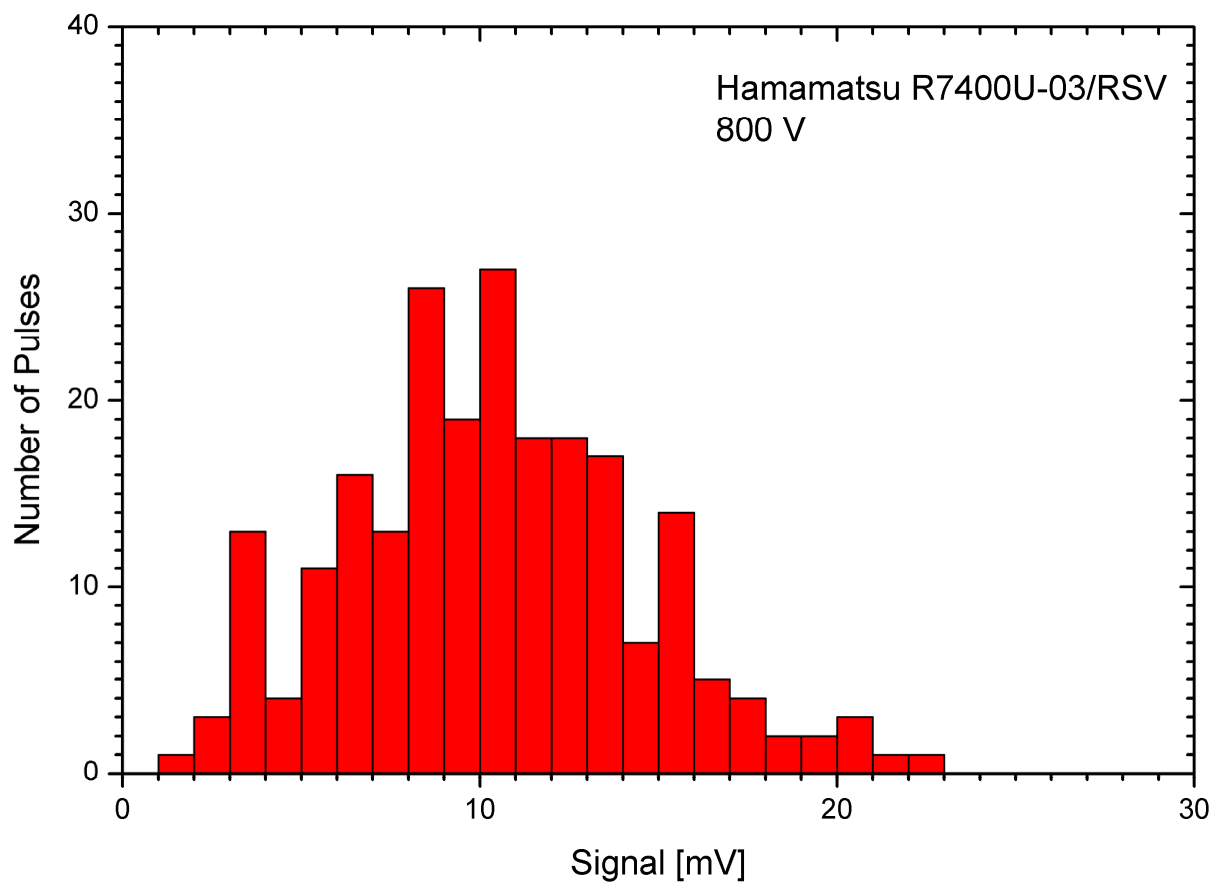
4

1



2 **Fig. 10.** Peak lidar signal measured with a R7400P-03 PMT as a function of the supply high voltage. The
3 measurement was made for different attenuations of the incoming radiation, calibrating the data to the results for
4 the standard settings. Signal-induced nonlinearities were only observed for very high photon fluxes, for which
5 the supply voltage had to be reduced to 450 V to ensure signals below 100 mV (Kreipl, 2006).
6

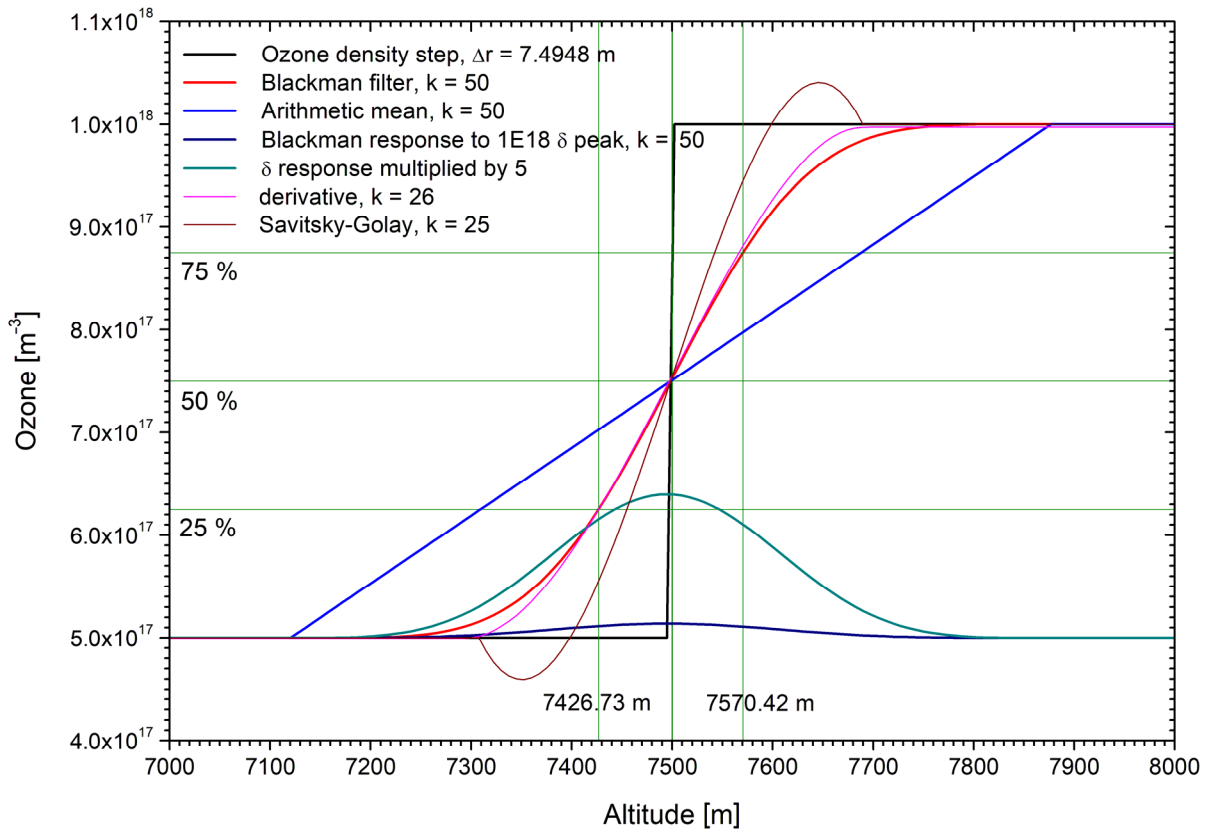
1



2 **Fig. 11.** Pulse height distribution of a Hamamatsu R7400-03 PMT (RSV module) for 800 V of operating voltage
3 determined from a long time scan with a 1-GHz digital oscilloscope (sign of the pulse amplitudes inverted)

4

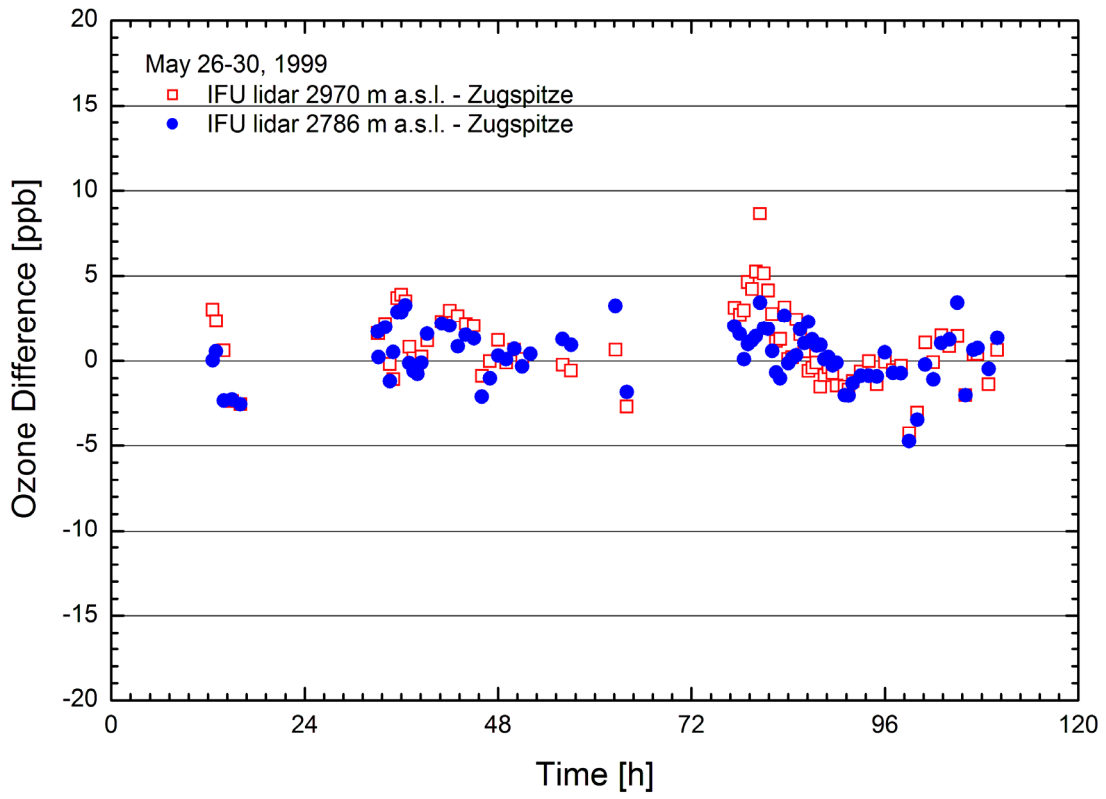
1



2 **Fig. 12.** Response of the digital filter used in the data-evaluation procedure for the IFU DIAL systems to a
 3 Heaviside ozone step and for a sliding arithmetic mean, both filters shown for smoothing over 101 points; a
 4 digitizer bin size of 7.4948 m is assumed. The VDI vertical resolution is the altitude difference for a rise from 25
 5 % to 75 % of the input step. For comparison, the very small response of the Blackman filter to a delta (single-
 6 bin) signal peak of 1×10^{18} residing on a 5×10^{17} background is shown, the enhancement also multiplied by 5. The
 7 slope for a $k = 27$ derivative filter (see text) is identical with that of the Blackman filter at half rise. Finally, the
 8 result of $k = 25$ Savitsky-Golay smoothing is shown, 25 being the maximum possible k value in the ORIGIN
 9 graphics package. This kind of smoothing is absolutely inadequate.

10

1



2 **Fig. 13.** Comparison of the stationary DIAL with the Zugspitze in-situ data during four days in May 1999
3 (VOTALP “Munich” field campaign); the deviations have diminished to about one half of the noise shown here
4 ever since.

5

6

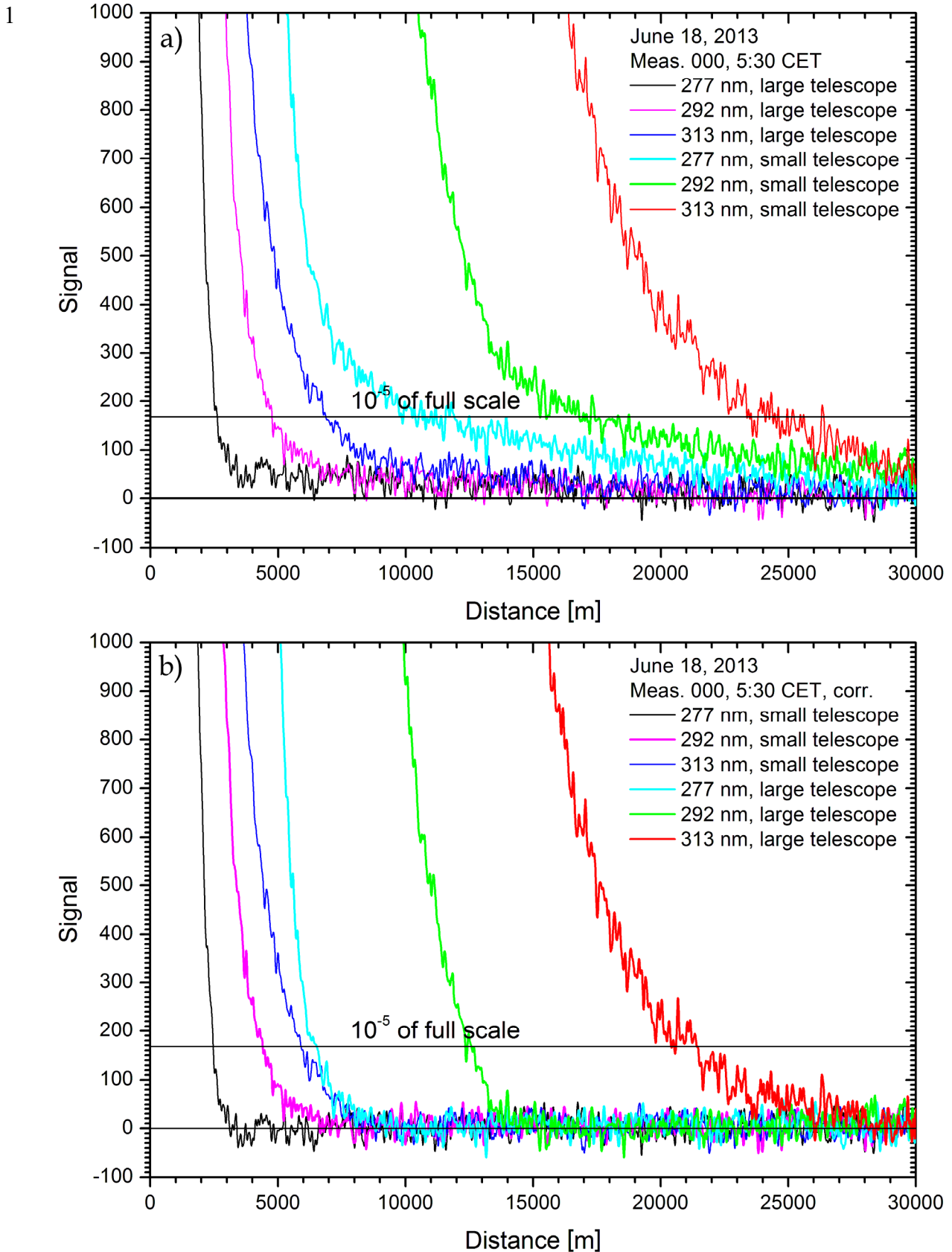
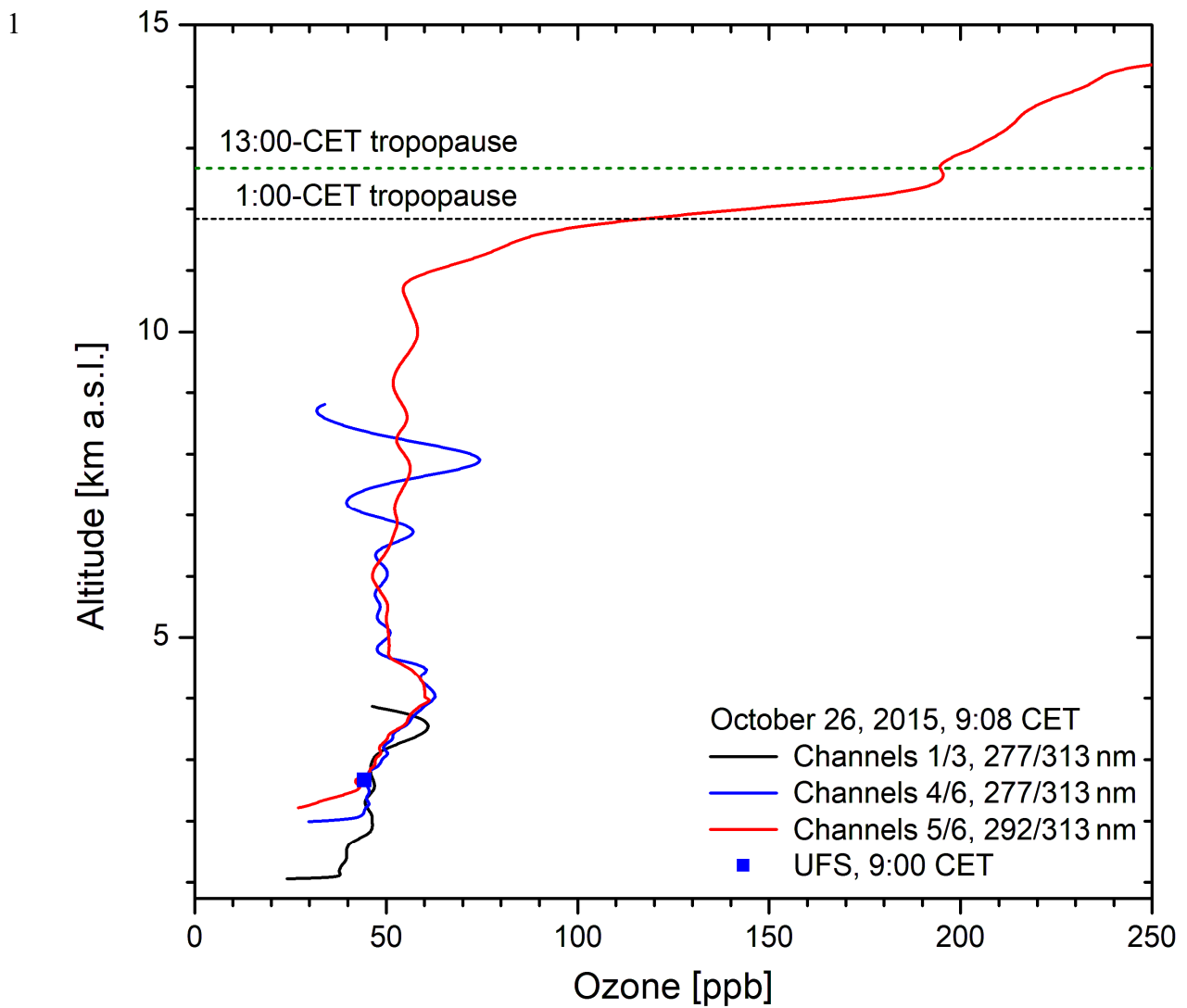
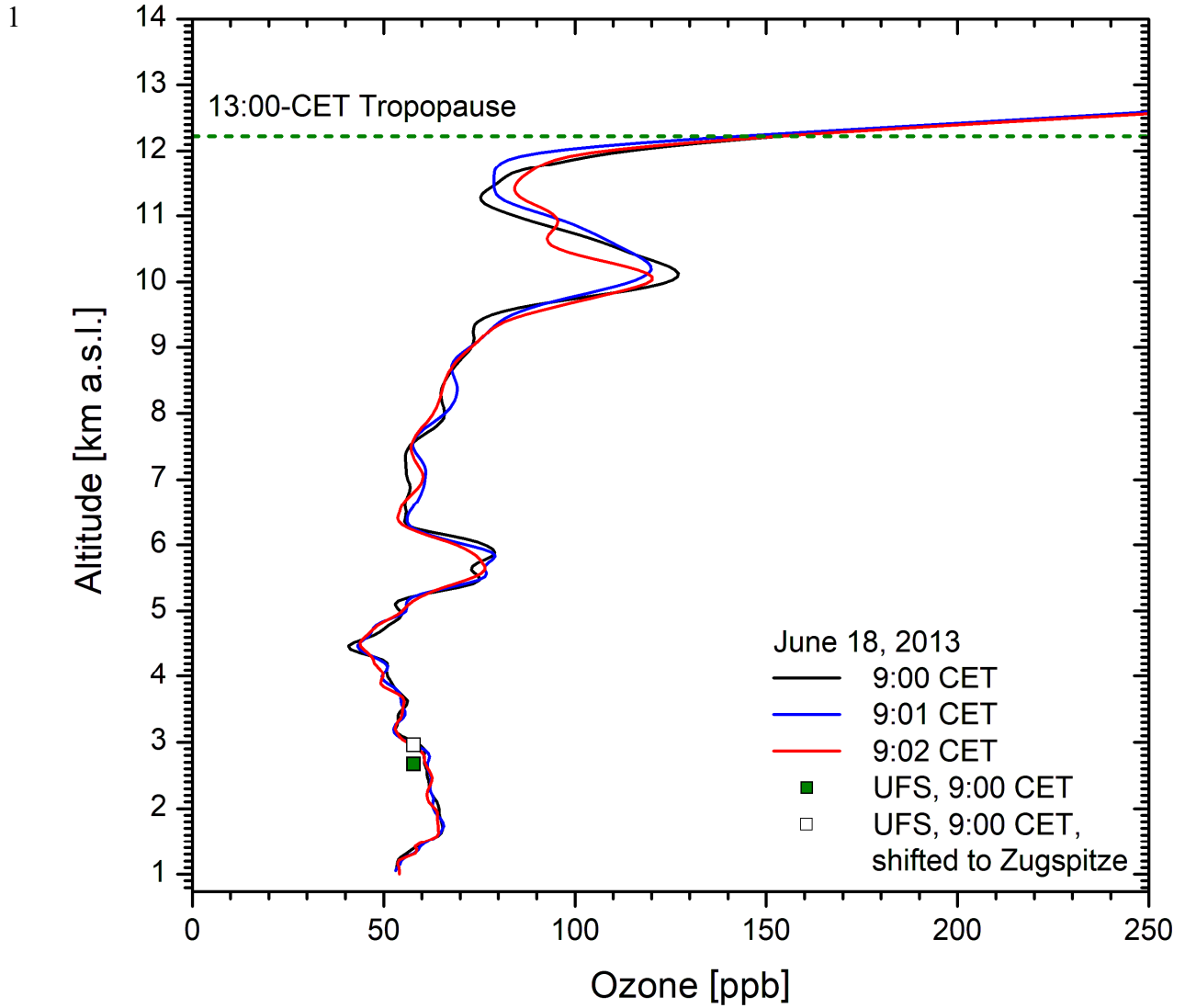


Fig. 14. Strongly expanded backscatter profiles without (a) and with (b) exponential correction, recorded after the introduction of the ground-free input stage to the transient digitizers in late 2012; the 313-nm signals are noisier due to the early-morning daylight background. The data are smoothed over ± 14 points (VDI vertical resolution 40 m) in order to reduce the digital ripple.



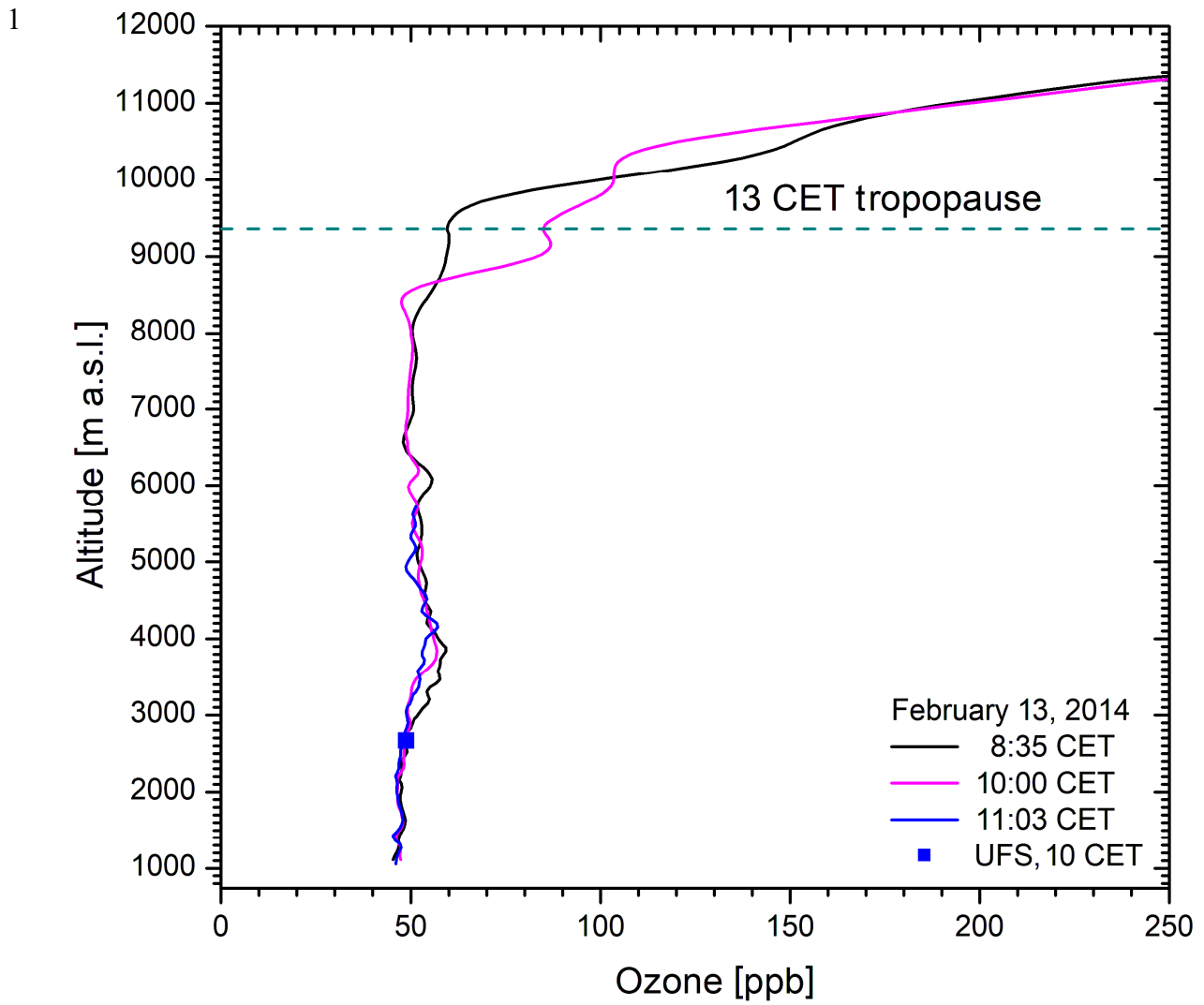
2 **Fig. 15.** Selection of partial ozone profiles from both receivers of the stationary: The near-field result can be
 3 used here to more than 2 km above the lidar due to low ozone density. The ozone hump between about 3.0 and
 4 4.8 km is caused by a remote stratospheric air intrusion. The lidar measurement agrees with that at the nearby
 5 Schneefernerhaus station (UFS, 2670 m; 0.7 ppb below blue curve). The altitude of the tropopause is taken from
 6 the Munich radiosonde.

7



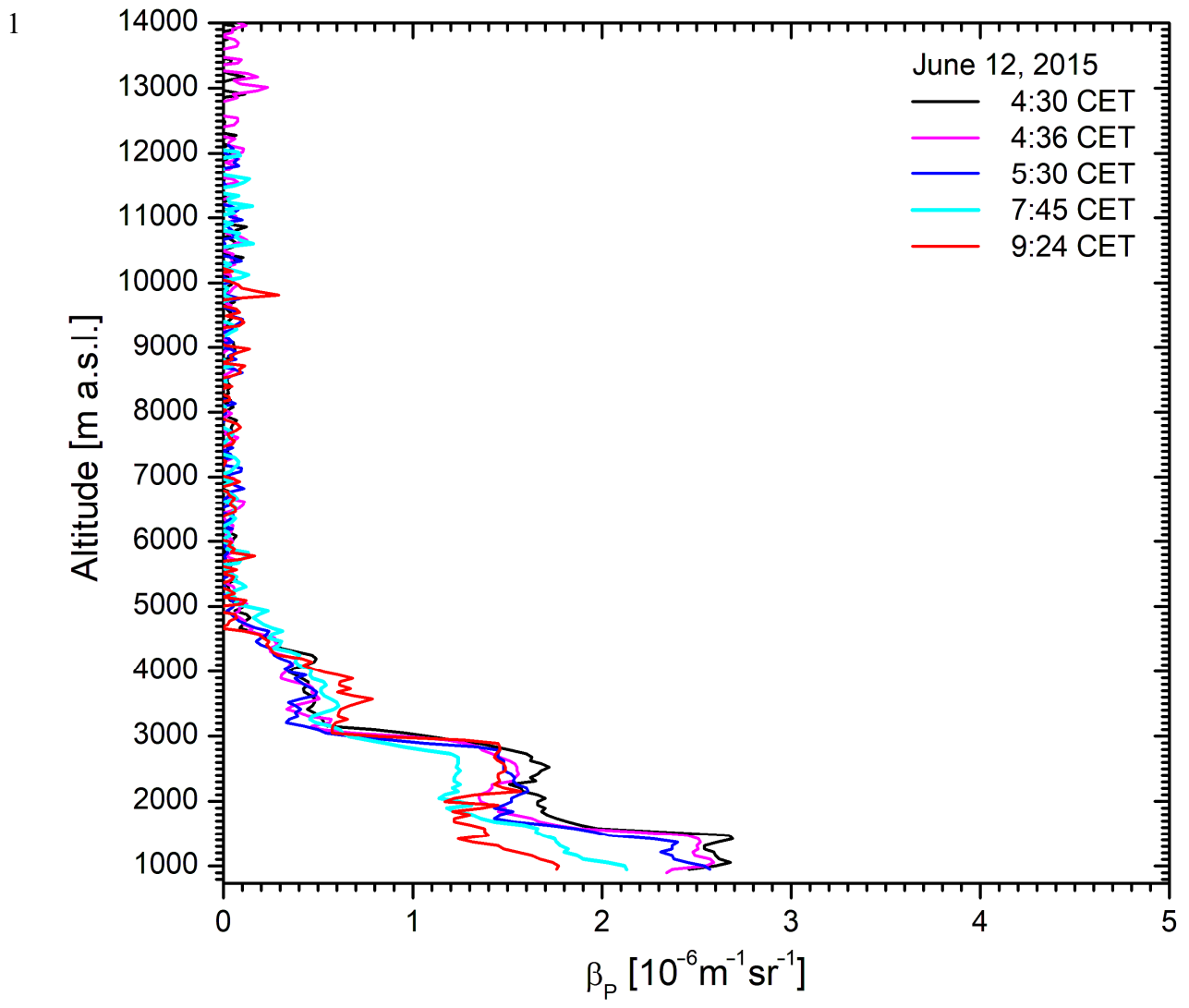
2 **Fig. 16.** Example for reproducibility testing during a period of elevated ozone: The “on” wavelengths used are
 3 277 nm (channel 1, near-field telescope, up to 2.23 km), 277 nm (channel 6, up to about 6 km) and 292 nm
 4 (channel 5, up to the top). The lidar measurement perfectly agrees with that at UFS if the altitude is shifted to
 5 that of the Zugspitze summit (2962 m), justified by the southerly advection. Above 5 km the signal in channel 6
 6 becomes low due to the high ozone values in the lower troposphere and a weighted average of the 277/292 nm
 7 ozone profile with that for 292/313 nm was applied for the final few hundred metres below 6 km. Above 9 km
 8 the 292-nm signal starts to become noisy resulting in reduced reproducibility. The altitude of the tropopause is
 9 taken from the Munich radiosonde.

10



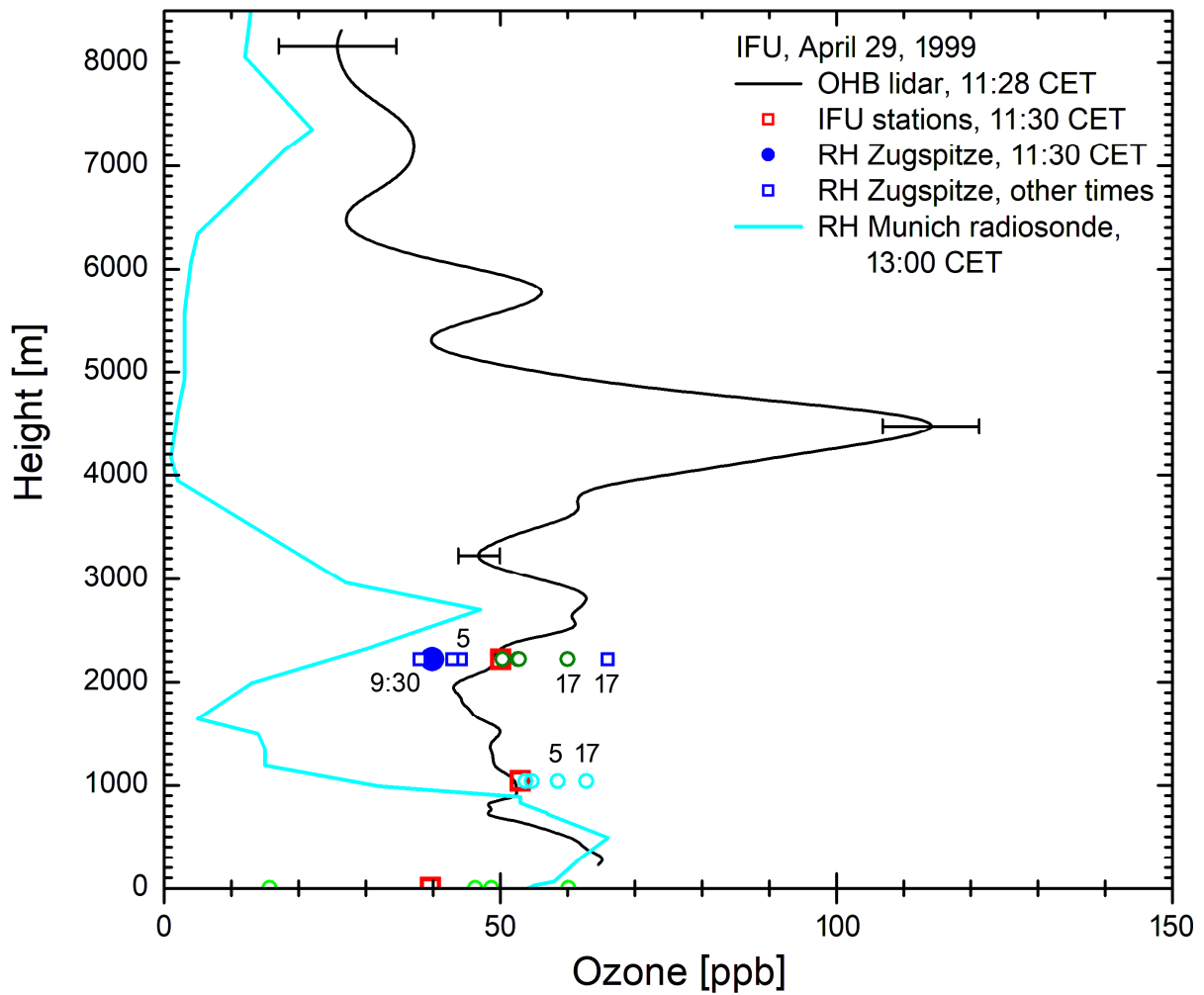
2 **Fig. 17:** Ozone measurement with the stationary DIAL on 13 February 2014; the variability is low apart from the
 3 two dry layers at below 4 km and at 6.1 km that are also visible in the 1-CET Munich radiosonde data and that
 4 seem to erode after 8:35 CET. The agreement with the in-situ measurements at UFS is perfect.

5



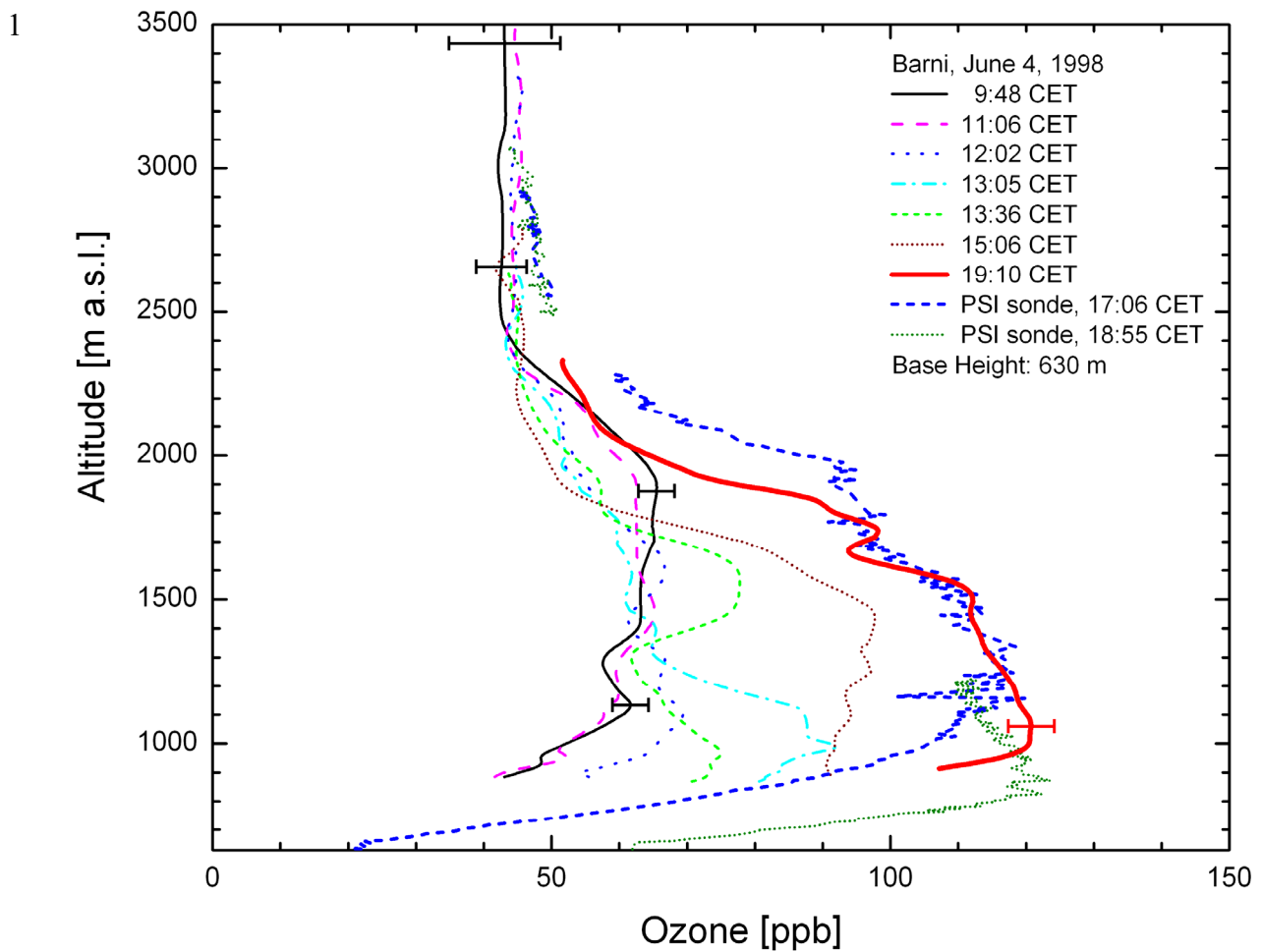
2 **Fig. 18.** 313-nm aerosol backscatter coefficients for 12 June 2015

1



2 **Fig. 19.** Ozone measurement with the mobile DIAL during the brightest part of the day, after all modifications
 3 had been made (about 10^4 laser shots): The vertical axis is the height above the lidar site (IFU, 730 m a.s.l.): Up
 4 to 2.7 km above the ground 266-299-nm wavelength pairs were taken (near-field: up to 1.5 km). Up to 3.7 km
 5 the combination 289-299 nm was used. Above this, ozone was obtained from a single-trace evaluation for 299
 6 nm, slightly recalibrated at the lower end of that range. For comparison, in-situ ozone values from the three local
 7 monitoring stations IFU (745 m a.s.l.), Wank (1780 m a.s.l.) and Zugspitze (2962 m a.s.l.) are shown for 11:30
 8 CET, (red squares). Additional values from these stations are marked with open circles for 5:00 CET, 9:30 CET,
 9 14:00 CET and 17:00 CET (labelled in some cases). For the interpretation of the complicated meteorological
 10 situation, the corresponding relative-humidity of the Zugspitze summit and the noon operational ascent of the
 11 Munich radiosonde are also included. Outside the most reliable part of the operating range a few representative
 12 error bars are drawn.

13



2 **Fig. 20.** Ozone measurements at Barni (Provincia di Como, Italy) on 4 June 1998, during the VOTALP Milano
 3 field campaign; the profiles show the day-time gradual advection of the Milano ozone plume. The ozone sonde
 4 data from the two launches at the lidar site have been kindly supplied by J. Keller (Paul-Scherrer-Institut,
 5 Switzerland; the times are launch times). Only 266 nm could be used as the “on” wavelength. As a consequence
 6 the range was strongly reduced during the period with the highest ozone mixing ratio.

7